DISS ETH NO. 25500

Resolution sensitivity and convergence behavior at convection-resolving scales in simulations of summertime moist convection over land

A thesis submitted to attain the degree of

DOCTOR OF SCIENCES of ETH ZURICH

(Dr. sc. ETH Zurich)

presented by

Davide Panosetti

MSc ETH in Atmospheric and Climate Science, ETH Zurich

born on 23.05.1990

citizen of

Italy

accepted on the recommendation of

Prof. Dr. Christoph Schär, examiner
Dr. Linda Schlemmer, co-examiner
Prof. Dr. Evelyne Richard, co-examiner

2018

Acknowledgments

Foremost, I would like to express my sincere gratitude to Christoph and Linda. My PhD project was excellently supervised. Christoph's expertise, guidance and motivation were fundamental throughout these three years. Linda's continuous engagement, enthusiasm and feedback helped me a lot through good and bad times. Their contribution to this PhD thesis was essential.

Several other people contributed to the outcome of this PhD thesis. Steef and Jürg guided me toward the publication of my first paper. Tapio gave me my first chance to be part of a research group before joining IAC and was an important contact person during my first years at ETH Zurich. Kathy and Dani helped me finding a way through the complexities of the COSMO model. Jacopo and Paolo contributed to the writing and revision of the thesis abstract in Italian.

I want to thank my fellow group members for these three years spent together, and Tapio's former group members, in particular Kyle and Colleen, for their support and guidance during my master studies at ETH Zurich.

A big thank you to my parents who supported me with my studies and guided me throughout my life. Thank you to all my friends for the wonderful time spent together in Zurich, particularly to my basketball fellas for the hits and bruises which were an essential getaway from the tough PhD life.

Last but not least, thanks to my wife who more than anyone else experienced the struggles of this journey and provided me with moral and emotional support in all kinds of situations.

Abstract

Convection-resolving models (CRMs) are a useful tool to study moist convection because they can successfully reproduce important physical processes related to moist convection without a convection parameterization. They also benefit from a better representation of complex topographic structures and surface fields, and are thus particularly suitable for simulations over land. However, the truncation of the continuous energy cascade at scales of $\mathcal{O}(1\,\mathrm{km})$ poses a serious challenge, as in kilometer-scale simulations the size and properties of the simulated convective cells are often determined by the horizontal grid spacing (Δx). Furthermore, the majority of the subgrid-scale turbulence parameterization schemes currently in use were devised for scales much larger or much smaller than the kilometer scale, and are thus in a strict sense not applicable to CRMs. Several previous studies have reported large sensitivities to Δx with regard to the size and properties of the simulated convective clouds, and observed a poor representation of boundary-layer turbulence in kilometer-scale simulations. On the other hand, other studies have shown that large-scale flow properties are much less sensitive to changes in Δx and often converge at the kilometer scale. This thesis aims at understanding more about the resolution sensitivity in CRMs and investigate further on the convergence behavior of both idealized and real-case simulations of summertime moist convection over land, with particular reference to the aforementioned issues.

In the first part a framework for a systematic assessment of physical convergence at the kilometer scale is presented. Physical convergence (or simply convergence) is defined as the insensitivity of flow statistics to Δx and associated changes in the flow physics, and is achieved when the resolution sensitivity systematically decreases at finer resolutions. The convergence of domain-averaged and integrated tendencies related to a large ensemble of convective cells (in this thesis referred to as *bulk convergence*, since the focus is on the bulk flow properties) is compared with the convergence of the size and properties of individual clouds and updrafts (in this thesis referred to as *structural convergence*, since the focus is on the structural details of the convective clouds). Results show that bulk convergence is generally achieved for a wide range of variables and different experiments. On the other hand, structural convergence is not yet fully achieved at the kilometer scale. In particular, smaller and more numerous clouds are simulated, and the convective

cells are weaker at coarser resolutions.

The second part extends the findings presented in the first part by assessing bulk and structural convergence in convection-resolving real-case simulations. Two episodes of thermally-driven convection over the Alps and of airmass convection over Central Germany are considered to compare the results over flat and mountainous terrain. Bulk convergence is discussed not only for the mean diurnal cycle of several quantities related to moist convection, but also for the spatial distribution of their integrated values. It is found that bulk convergence is systematically achieved in both episodes for the spatial distribution of the analyzed quantities. For their mean diurnal cycle, bulk convergence was generally achieved over the Alps but not over Central Germany, owing to the mesoscale forcing stemming from the orography in the former case. Structural convergence is confirmed to be not yet achieved at the kilometer scale.

A third part is devoted to exploring the sensitivities of both the mean flow properties and characteristics of the individual convective cells to the subgrid-scale turbulence treatment at convection-resolving scales. A 1D TKE-based turbulence parameterization devised for mesoscale modeling with grid-independent but tunable diffusivity and a 3D Smagorinsky turbulence closure devised for LES are compared at different Δx in real-case simulations over flat and mountainous terrain. Results show that the mean flow properties are more sensitive to the subgrid-scale turbulence treatment than to Δx, whereas the opposite applies to the characteristics of the individual convective cells. A less diffusive 1D model produces stronger convective cells, thicker clouds but reduced cloud cover, lower cloud base and more precipitation. These sensitivities are generally more pronounced at coarse resolutions and over flat terrain. The diffusivity of the 1D model had little impact on the characteristics of the single convective cells, which are mostly determined by Δx. The 3D Smagorinsky closure yields similar results to a largely diffusive 1D model at the kilometer and larger scales, suggesting that this scheme is not applicable at such scales. However, the two became comparable at sub-kilometer scales, indicating that 3D schemes yield reasonable performances also at scales larger than those for which they were designed, and should preferably be used at Δx smaller than a few hundred meters.

In summary, the results presented in this thesis demonstrate that kilometer-scale resolutions are often sufficient provided that the focus is on the bulk flow properties and the feedbacks between the convective clouds and the large-scale environment. This encourages the application of CRMs for regional-scale or global climate projections. Nevertheless, the findings confirm that CRMs currently operate at too coarse resolutions to fully resolve the structural details of the cloud field and the complex boundary-layer dynamics, and also highlight the high demand for scale-aware turbulence parameterizations.

Riepilogo

I modelli a passo di griglia di $\mathcal{O}(1\,\text{km})$ (convection-resolving models, CRMs) sono uno strumento molto utile per lo studio della convezione perché possono rappresentare in maniera esplicita importanti processi fisici ad essa collegati senza la necessità di parametrizzare la convezione. Questi modelli beneficiano inoltre di una rappresentazione più dettagliata di complesse strutture topografiche e delle caratteristiche del suolo, e sono dunque particolarmente adatti per simulazioni su topografia. Tuttavia, l'impossibilità di rappresentare con continuità lo spettro energetico ad una scala inferiore a $\mathcal{O}(1\,\text{km})$ rappresenta un problema complesso dal punto di vista modellistico, in quanto le dimensioni e le proprietà delle celle convettive risultano determinate principalmente dal passo di griglia (Δx). Inoltre, la maggioranza delle parametrizzazioni dei processi turbolenti oggi in uso sono state concepite per scale ben maggiori o minori del tipico Δx di un CRM, ed un loro utilizzo in tali modelli non è quindi giustificato. Numerosi studi hanno dimostrato che le dimensioni e le proprietà delle celle convettive simulate dai CRM variano notevolmente a seconda della risoluzione impiegata, e che la turbolenza nello strato limite planetario non è adeguamente rappresentata. Tuttavia, altri studi hanno osservato che le caratteristiche a larga scala dipendono molto meno dalla risoluzione del modello, e dimostrato la loro convergenza a scale di $\mathcal{O}(1\,\text{km})$. Questa tesi ambisce ad approfondire le sensibilità al Δx delle variabili atmosferiche nei CRM ed a studiare la loro convergenza in simulazioni idealizzate e realistiche di convezione umida su terreno, con particolare attenzione alle problematiche sopra citate.

Nella prima parte della tesi viene introdotto un concetto ben definito per lo studio della convergenza delle variabili atmosferiche. Per convergenza fisica (o semplicemente convergenza) si intende l'insensibilità delle variabili atmosferiche sia al Δx, sia a cambiamenti nella rappresentazione della fisica dello stesso modello associati al Δx, e si ottiene quando la sensibilità alla risoluzione del modello diminuisce sistematicamente a Δx inferiori. La convergenza delle variabili medie atmosferiche in domini abbastanza grandi da contenere un numero elevato di celle convettive (in questa tesi definita *convergenza a larga scala*) viene confrontata con la convergenza delle dimensioni e proprietà delle singole celle convettive (in questa tesi definita *convergenza strutturale*) in simulazioni idealizzate. I risultati dimostrano convergenza a larga scala di diverse variabili atmosferiche ed in diversi esperimenti. D'altro canto, la

convergenza strutturale non è ottenuta a risoluzioni tipiche di un CRM. In particolare, le nubi simulate ad alta risoluzione sono più numerose e di dimensioni minori, e le celle convettive presentano una minore intensità.

La seconda parte consiste in un'estensione della prima in cui convergenza a larga scala e strutturale vengono messe a confronto in simulazioni realistiche. Due episodi di convezione orografica estiva sulle Alpi e di convezione libera sulla Germania Centrale vengono studiati per confrontare i risultati in presenza o meno di una forzante orografica alla mesoscala. La convergenza a larga scala viene discussa non solo per il ciclo medio diurno di diverse variabili atmosferiche, ma anche per la distribuzione spaziale dei loro valori integrati. Viene dimostrato che la convergenza a larga scala è sistematicamente ottenuta in entrambi gli episodi per la distribuzione spaziale delle variabili atmosferiche considerate. Per quanto riguarda il loro ciclo medio diurno, la convergenza a larga scala è in genere osservata nelle simulazioni sulle Alpi, ma non in quelle sulla Germania Centrale, sottolineando il ruolo della forzante orografica alla mesoscala nel ridurre la sensibilità delle variabili medie atmosferiche al Δx. Per quanto riguarda la convergenza strutturale, viene confermato che questa non può essere ottenuta a passi di griglia di $\mathcal{O}(1\,\text{km})$. La velocità verticale media all'interno delle nubi convettive e la dimensione di queste ultime infatti risultano essere particolarmente sensibili al Δx.

La terza parte tratta delle sensibilità sia delle proprietà medie dell'atmosfera, sia delle caratteristiche delle singole nubi convettive alla parametrizzazione della turbolenza. Una parametrizzazione unidimensionale (1D) formulata sull'equazione dell'energia cinetica turbolenta e concepita per modelli alla mesoscala con un grado di diffusione indipendente dal passo di griglia ma regolabile viene confrontata con una parametrizzazione tridimensionale (3D) concepita per large-eddy simulation a Δx di $\mathcal{O}(100\,\text{m})$ in simulazioni realistiche su terreno sia pianeggiante che montuoso. I risultati dimostrano che le variabili medie atmosferiche sono più sensibili alla parametrizzazione della turbolenza impiegata che al Δx, mentre l'opposto vale per le caratteristiche delle singole nubi convettive. Un modello 1D meno diffusivo produce celle convettive più vigorose, nubi più spesse ma coperture nuvolose ridotte, una base delle nubi inferiore e maggiori precipitazioni. Questi effetti sono più rilevanti in simulazioni su pianura e a risoluzioni inferiori. La diffusività del modello ha un impatto contenuto sulla dimensione delle singole celle convettive e sulle variabili atmosferiche relative alle singole nubi come la frazione delle nubi di dimensioni uguali al Δx e la distanza media tra le nubi, le quali sono determinate principalmente dal Δx. Il modello 3D risulta essere molto più diffusivo del modello 1D a scale di $\mathcal{O}(1\,\text{km})$ o maggiori, sottolineando che parametrizzazioni di questo tipo non dovrebbero in principio essere utilizzate a scale simili. Tuttavia, i due modelli producono risultati simili a scale sotto il chilometro, indicando che il modello 3D rende performance accettabili anche a Δx più grandi di quelli per cui è stato concepito, ed inoltre che potrebbe essere più adatto per Δx più piccoli di alcune centinaia di metri.

In sintesi, gli studi presentati in questa tesi dimostrano che simulazioni a passo di griglia di $\mathcal{O}(1\,\text{km})$ sono nella maggior parte dei casi sufficienti per rappresentare le proprietá medie dell'atmosfera e i feedback tra le nubi convettive ed i fenomeni a larga scala. Questi risultati supportano l'utilizzo di questi modelli per simulazioni climatiche a scala regionale e globale. Tuttavia, questa tesi ha dimostrato che questi modelli operano a Δx troppo grandi per risolvere in maniera esplicita i dettagli strutturali e le proprietà delle singole nubi convettive e la dinamica dello strato limite planetario, e sottolineato l'importanza dello sviluppo di nuove parametrizzazioni della turbolenza che possano essere applicate a simili scale spaziali.

Contents

We excuse our sloth
under the pretext
of difficulty.

1

Introduction

Moist convection is a fundamental process in the atmosphere and a major component of the water and energy cycles. Its key role is to transfer sensible and latent heat from the surface to the upper troposphere to counteract the destabilization caused by radiative effects, surface fluxes or synoptic and large-scale circulations. Clouds are manifestations of moist convection. Upward transport and detrainment of condensate and atmospheric constituents into the upper troposphere by deep convective clouds is critical to the climate system because of the resulting vertical mixing of the troposphere. Clouds can also generate precipitation. Particularly during summer, convective rainfall is a relevant process in the mid-latitude atmosphere. Besides its positive ecological effects (such as water supply), deep convective storms produce a variety of hazardous weather events such as flash floods, large hail, damaging wind gusts, tornadoes and lightnings. For these reasons, numerical weather prediction and climate models are required to describe accurately the physical processes behind the initiation and development of moist convection with the ultimate goal of improving the prediction of the probability of occurrence of hazardous events and our understanding of the feedbacks between convective clouds and the climate system.

This chapter provides a brief introduction into atmospheric moist convection, with particular focus on its triggering and evolution over mountainous terrain. Capabilities, potential and limitations of numerical models in representing convection at convection-resolving scales are presented. The goals of this thesis are outlined at the end of this chapter.

1.1 An introduction into atmospheric moist convection

For a first definition of convection one may go back to the Archimede's principle stating that a body completely or partially immersed in a fluid at rest is acted upon by an upward, or buoyant, force of magnitude equal to the weight of the fluid displaced. Of particular interest for the atmosphere is moist convection, i.e. upward and downward motions (or thermals) associated with moist air and phase changes of water (cloud formation). Dry convection, such as boundary-layer (BL) thermals, is also important because it is a precursor for moist convection.

Moist convection is involved in many day-to-day changes in weather, and can express itself with a rich phenomenology spanning a wide range of scales. Examples of moist convection are stratiform cloud decks that efficiently reflect incoming sunlight, fair-weather shallow cumuli as well as deep convective clouds such as cumulonimbus clouds. These latter are of particular interest to the society because, despite their short lifespan of a few hours, they can generate heavy and highly localized rainfall, strong wind gusts and damaging lightning strikes. Moist convection is a key feature of the water cycle [e.g. Schneider et al., 2010; Stevens and Bony, 2013a] and an important element of the climate system [e.g. Emanuel, 1994; Schneider, 2006]. Heating/cooling and drying/moistening of the surrounding environment occur through latent heat release from developing clouds, compensating subsidence, detrainment of updraft air at the cloud top, and evaporation and melting of falling condensate. During daytime, low clouds cool the surface by reflecting sunlight, but they also have a surface warming effect because they absorb and re-emit infrared radiation coming from the surface.

The concept of "parcel theory" [e.g. Emanuel, 1994] is useful for a qualitative understanding of the formation and development of moist convection. The concept can be illustrated by a fluid parcel in initial equilibrium with its environment that is displaced (lifted) such that its thermodynamic state (i.e. temperature and water loading) deviates from the equilibrium state in its new environment. If in its new environment the fluid parcel is of lower density than the surrounding air (i.e. it is positively buoyant) it will rise. This process is fundamentally altered by the presence of moisture. When condensation of water vapor into cloud droplets occurs above the lifting condensation level (LCL), latent heat is released and the fluid parcel becomes less dense. This additional heating partly offsets the adiabatic cooling that the fluid parcel experiences as it rises, and allows it to ascend into regions that it will not be able to reach without condensational heating. Beyond the level of free convection (LFC) the fluid parcel continues to rise until its level of neutral buoyancy (LNB), i.e. until it reaches a new state of equilibrium with its environment. On the other hand, mixing with the dry environment (entrainment) causes some of the cloud water to re-evaporate, and the associated evaporative cooling acts toward damping convection. The potential energy necessary to lift the parcel to its LFC is referred to as convective

inhibition (CIN), and the energy available between the LFC and the LNB is called convective available potential energy (CAPE).

A rather arbitrary distinction between two different regimes of cumulus convection is generally made. Shallow convection has a limited vertical extent, and arises from dry BL thermals that may reach the LCL to form shallow cumulus clouds. Precipitation is generally very low or absent, and clouds are weakly organized. Low rainfall rates also imply that these clouds lead to moistening and cooling of the free troposphere and accumulation of latent heating in the BL [e.g. Stevens, 2005]. Deep convective clouds develop if parcels are lifted to their LFC to continue a free ascent with positive buoyancy. These clouds often reach, and sometimes overshoot the tropopause, warming the upper troposphere and drying the atmospheric column due to the abundant precipitation generated. The formation of cloud systems (cloud organization) plays an important role. Deep convection is often observed in the form of mesoscale convective systems, particularly in the tropics, or frontal systems and squall lines in the mid-latitudes [Houze, 1993]. Cooling by evaporation of precipitation below convective clouds results in cold pools, which are characterized by a near-surface horizontal flow of relatively cold and dry air and may favor cloud organization [e.g. Grabowski et al., 2006; Böing et al., 2012; Schlemmer and Hohenegger, 2014].

1.2 The role of mountains

A large fraction of the global land surface is covered by mountains. Precipitation climatologies indicate a preferential location for rainfall over mountainous regions. For example, a climatology of Central Europe from high-resolution rain-gauge observations by Frei and Schär [1998] indicates that the most intense precipitation with values above $3\,\mathrm{mm\,day^{-1}}$ or $1000\,\mathrm{mm\,year^{-1}}$ occurs in the vicinity of high mountain peaks. A similar pattern was observed by Fiddes et al. [2015] over Eastern Australia.

The strong local control exerted by mountains on the formation of clouds and the rainfall distribution has been the subject of several studies. These include aircraft [Braham Jr and Draginis, 1960; Raymond and Wilkening, 1980; Banta, 1984; Banta and Barker Schaaf, 1987] and satellite [e.g. Xie et al., 2006] measurements, in-situ and doppler observations [Demko et al., 2009; Demko and Geerts, 2010a,b] as well as model studies [e.g. Meissner et al., 2007; Bennett et al., 2011]. A number of large field experiments were also organized to collect high-resolution data necessary for model validation, such as the Mesoscale Alpine Program (MAP; Bougeault et al., 2001) in 1999 covering the Alps, and the Convective and Orographically-induced Precipitation Study (COPS; Wulfmeyer et al., 2008) in 2007 covering the Vosges mountains, the Rhine valley and the Black Forest mountains. The importance of the orography in triggering convection was highlighted by Barthlott and Hoose [2015] also in the context of the more recent and broader Hydro-

logical cycle in the Mediterranean Experiment (HyMeX; see e.g. Drobinski et al., 2014).

The mechanisms leading to the orographic triggering or enhancement of convection and precipitation have been extensively reviewed in the literature [e.g. Banta, 1984, 1990; Houze, 1993; Schär, 2002; Kirshbaum et al., 2018]. A relevant mechanism is the enforced adiabatic ascent of the impinging air (particularly in wintertime). Orographic ascent enhances precipitation by lifting air to saturation, increasing the hydrometeor content of impinging clouds, and initiating moist instabilities [Kirshbaum et al., 2018]. Aircraft measurements have also shown that mountains favor cloud organization [Kirshbaum and Grant, 2012]. The importance of boundary-layer convergence for convection initiation was highlighted by Barthlott et al. [2011] and Richard et al. [2011]. Another orographic precipitation-enhancement mechanism is the seeder-feeder effect [Bergeron, 1965; Purdy et al., 2005], in which precipitation from an upper-level precipitating cloud (seeder) falls through a lower-level orographic cloud (feeder) capping a hill or a small mountain, thus producing greater precipitation on the hill or mountain under the lower feeder cloud by collecting cloud water as it passes through it by collision and coalescence or accretion.

Of particular interest for the scope of this thesis, are thermally-driven wind systems. These wind systems determine the airmass exchange between mountainous regions and the adjacent plains and are observed on a wide range of scales, from the whole mountain range [e.g. Reiter and Tang, 1984; Lugauer and Winkler, 2005], to the scale of single valleys and slopes [e.g. Wagner, 1932]. Thermally-driven wind systems form due to horizontal density gradients generated by differential surface heating between the mountain peaks and the surrounding plains and valleys [e.g. Egger, 1990; Whiteman, 1990]. On fair-weather days, they are important for the transport and mixing of heat, moisture, and other constituents over mountainous terrain [Schmidli, 2013]. In the presence of a supportive environment, convergence of thermally-driven winds is an important convection initiation mechanism.

Figure 1.1 illustrates the early-afternoon transition from shallow to deep, precipitating convection in a large-eddy simulation (LES) of moist convection over an idealized double mountain ridge. The simulations were performed in the abscence of large-scale forcing, with a strongly inhibited (but conditionally unstable) atmosphere (see Panosetti et al., 2016), which are commonly observed features in Central Europe in summertime. This is a perfect visualization of how mass convergence and a weaker inhibition over the mountain peaks combine with moisture advection by thermally-driven upslope winds to initiate deep convection.
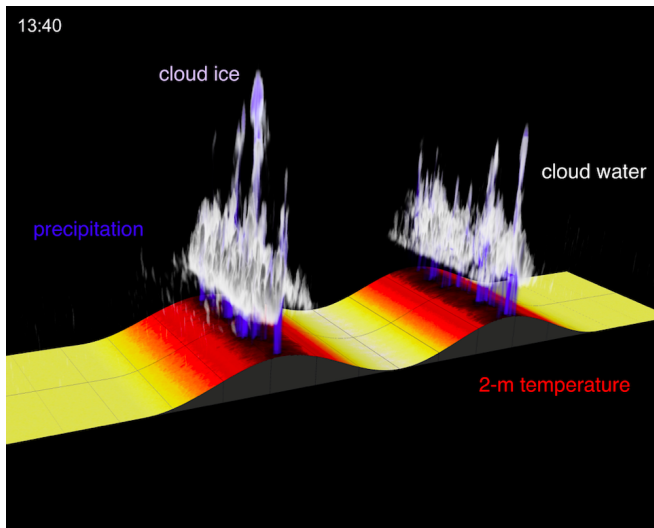
Figure 1.1: Transition from shallow to deep, precipitating convection in a large-eddy simulation of moist convection over an idealized double mountain ridge (see Panosetti et al., 2016). The color shading of the surface indicates the 2-m temperature (dark colors for cold temperature), the precipitation is illustrated in blue, cloud water in a greyscale, and the light blue colors at the top illustrate cloud ice. The figure is an extract of an animation published on the Climate Visuals Vimeo channel of ETH Zurich: https://vimeo.com/152534469. Courtesy of Linda Schlemmer.

1.3 Convection-resolving modeling

1.3.1 Parameterization of convection

A large number of state-of-the-art global (GCMs) and regional-scale (RCMs) climate models still operate at horizontal grid spacings (Δx) of $\mathcal{O}(100\,\mathrm{km})$ and of $\mathcal{O}(10\,\mathrm{km})$ respectively. Important processes that are not resolved at neither of these scales must be parameterized, i.e. described in terms of the resolved variables. These processes strongly affect global and regional climate and their parameterization is considered a major source of errors and uncertainty in future climate projections [e.g. Pedersen and Winther, 2005; Déqué et al., 2007]. In particular, parameterizing convection requires a sophisticated modeling approach because the triggering and development of convective clouds emerge from an interplay of processes acting at the scale of cloud droplet formation ($\simeq 10^{-6}\,\mathrm{m}$) to the synoptic scale ($\simeq 10^{6}\,\mathrm{m}$).

Some of the open issues in parameterizing convective clouds in climate models are discussed in Randall et al. [2003] and Arakawa [2004]. These mostly regard the triggering (is convection active in a gridbox?), the closure (how

intense is convection?) and the vertical transport of heat, water vapor and mass (how does convection change the surrounding environment?). Besides these issues, the assumptions made for the entrainment and detrainment of convective plumes (see de Rooy et al., 2013 for a review) and for their precipitation efficiency [e.g. Renno et al., 1994] remain rather crude. Large uncertainties in both GCMs and RCMs are related to the representation of clouds and convection [e.g. Sanderson et al., 2008; Sherwood et al., 2014]. Furthermore, convection parameterizations interact with many other subgrid-scale schemes, such as microphysics, radiation, and turbulence, such that error propagation can occur due to non-linearities [e.g. Stevens and Bony, 2013b]. The use of convection parameterization schemes leads to well-known issues such as a too early onset of convection in comparison to observations [e.g. Dai and Trenberth, 2004; Bechtold et al., 2004; Brockhaus et al., 2008], the underestimation of dry days and overestimation of low precipitation event frequency [e.g. Berg et al., 2013], the underestimation of hourly precipitation intensity [e.g. Ban et al., 2014; Fosser et al., 2015] and the misrepresentation of orogenic propagating precipitation systems [Pritchard et al., 2011], the soil moisture-precipitation feedback [e.g. Hohenegger et al., 2009; Taylor et al., 2013] and several tropical biases associated with the Madden-Julian oscillation [Zhang and Mu, 2005] and with the Intertropical Convergence Zone [Song and Zhang, 2009; Zhang and Song, 2010].

1.3.2   The added value of convection-resolving modeling

Although recently developed parameterization schemes have led to improvements of several of these issues [e.g. Donner et al., 2011; Bengtsson et al., 2013; Bechtold et al., 2014], the increasing computational resources have allowed simulations of moist convection at the so-called "convection-resolving" scales of $\mathcal{O}(1\,\mathrm{km})$. At these resolutions the fundamental non-hydrostatic processes behind deep convective clouds are explicitly resolved [Klemp and Wilhelmson, 1978; Weisman et al., 1997] and deep convection parameterization can be switched off. Today such convection-resolving models (CRMs: often referred to as convection-permitting or cloud-resolving models in the literature, see e.g. Prein et al., 2015) are largely employed by research institutions to study moist convection and by national weather services for limited-area NWP [e.g. Saito et al., 2007; Weusthoff et al., 2010; Tang et al., 2013; Brousseau et al., 2016]. The general experience is that CRMs outperform convection-parameterizing models (CPMs) in both NWP [e.g. Done et al., 2004; Richard et al., 2007; Lean et al., 2008; Weisman et al., 2008] and regional-scale climate modeling [e.g. Kendon et al., 2012; Ban et al., 2014]. Moreover, recent studies have established CRMs as a solid framework for decade-long continental-scale climate simulations [e.g. Liu et al., 2016; Leutwyler et al., 2016, 2017; Prein et al., 2017] and global NWP and climate simulations [e.g. Skamarock et al., 2014; Heinzeller et al., 2016; Kajikawa et al., 2016].
The increased resolution in CRMs also yields a better representation of the

underlying orography, coast lines and land surface heterogeneity [e.g. Leroyer et al., 2014], which may cause initial cloud formation [Pielke Sr, 2001]. Features such as cloud self-organization, gust fronts from earlier clouds and precipitation-driven cold pools may also be explicitly resolved and contribute to a better representation of the diurnal cycle of convection [e.g. Lean et al., 2008; Hohenegger et al., 2015].

1.3.3 Modeling within the grey zone of convection

Atmospheric dynamics is highly turbulent, nonlinear and chaotic. As a consequence, interactions result in energy cascades across a wide range of different scales. The scales of atmospheric phenomena span several orders of magnitude, from the planetary scales of Rossby wave propagation ($\simeq 10^6$ m), to the Kolmogorov microscale ($\simeq 10^{-3}$ m) where energy is dissipated into heat [Wyngaard, 2010] (Fig. 1.2). Beyond that, cloud microphysical processes extend down to the scale of cloud droplet formation ($\simeq 10^{-6}$ m). Numerical models are able to represent explicitly only a truncated portion of all these scales. Physical parameterization of subgrid-scale turbulence and convection, as well as explicit and implicit numerical diffusion contribute to defining the quantity of energy at the grid scale. However, such scale separation between grid-scale and subgrid-scale processes does not exist in nature. It is therefore questionable whether the total energy cascade is replicated correctly or not in numerical models [Honnert et al., 2011; Schemann et al., 2013]. As a result of this, the size and properties of the simulated smallest convective features are often determined by Δx.

Convective clouds have approximately the same size or are even smaller than the horizontal grid spacing generally employed in today's NWP models and RCMs. At these scales neither a traditional parameterization nor explicit dynamics are well suited, and the use of either may lead to systematic errors. These include, for example, an erroneous spatial distribution and temporal evolution of precipitation [e.g. Xu et al., 2002; Bryan et al., 2003]. This "no-men's land" in which the partition between grid-scale and subgrid-scale processes is unclear is called the "grey zone" [e.g. Craig and Dörnbrack, 2008] of convection.

Modeling within the grey zone is challenging mostly due to the model's inability to represent processes such as shallow convection, entrainment and detrainment, and of the uncertainties related to the treatment of subgrid-scale turbulence.

The grey zone of turbulence is defined in Wyngaard [2004] as the scales on the order of the energy-containing turbulence scale and displayed in Fig. 1.3. The fundamental difference with regard to turbulence treatment in mesoscale models is symbolized by the parameter $\alpha = l/\Delta$, where l is the energy-containing turbulence scale (1 km is a good order of magnitude for convective conditions), and Δ is the grid size. In mesoscale models ($\mathcal{O}(10$ km$)$ mesh size), $\alpha \ll 1$ and therefore none of the turbulence can be resolved. In
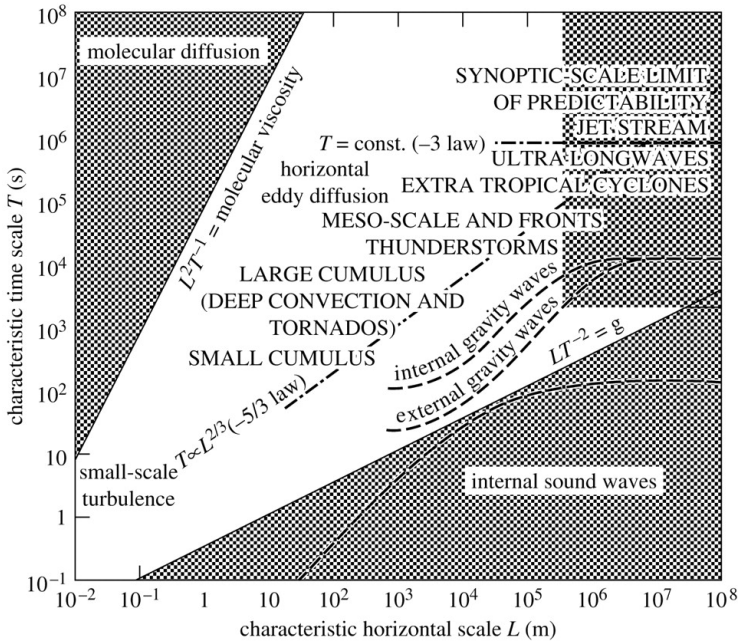
Figure 1.2: Typical space and timescales of atmospheric phenomena (following Smagorinsky [1974].

large eddy simulation models (LES; $\mathcal{O}(100\,\mathrm{m})$ horizontal grid spacing), on the other hand, the finer grid allows for explicit resolution of the largest BL eddies, and $\alpha >> 1$. Turbulence in mesoscale models is often treated by simple one-dimensional (1D) turbulence schemes, which assume that the net effect of turbulence consists in a mostly vertical down-gradient flux. In LES, three-dimensional (3D) subgrid-scale models are employed to account for the horizontal down-gradient fluxes as well. However, in CRMs, the model resolution is roughly equal to the characteristic turbulence scales of convective structures ($\alpha \sim 1$; Craig and Dörnbrack, 2008), and thus neither LES nor 1D turbulence schemes are strictly applicable.

Numerical simulations in the grey zone for BL turbulence do not only have issues with turbulence treatment, but it is also questionable whether a shallow convection parameterization scheme should be employed. Most of the convection parameterization schemes employed in CRMs have in fact been devised for GCMs [e.g. Tiedtke, 1989; Kain and Fritsch, 1990], and are thus based on assumptions that are often violated at such scales. Furthermore, in CRMs the model grid size is roughly equal to or even larger than the typical horizontal size of shallow clouds. Therefore a shallow convection parameteri-

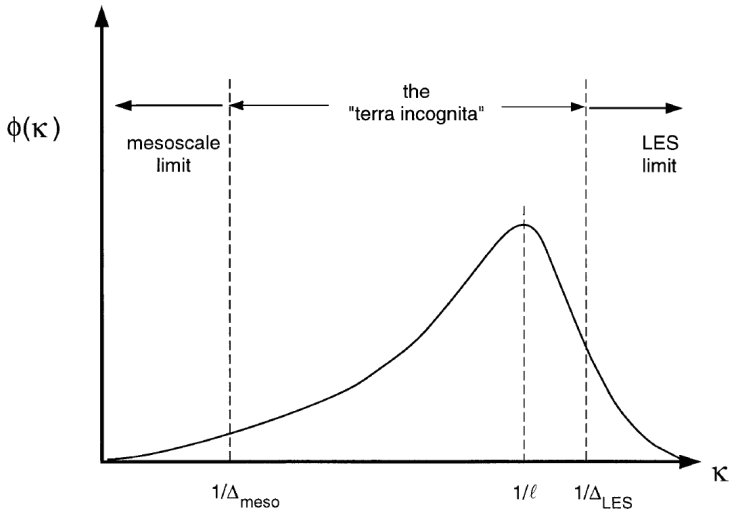**Figure 1.3:** A schematic of a turbulence spectrum (i.e. a function that illustrates the quantity of energy contained in turbulent eddies of a given size) $\phi(k)$ in the horizontal plane as a function of the horizontal wavenumber k. Its peak is at $k \sim 1/l$, where l is the length scale of the energetic eddies. Δ is the model grid size. In the mesoscale limit (left), $\Delta_{meso} >> l$ and none of the turbulence is resolved. In the LES limit (right), $\Delta_{LES} << 1$ and the energy-containing turbulence is resolved. From Wyngaard [2004].

zation might still be necessary to capture sufficient moisture transport from the boundary layer into the mid-troposphere.

1.3.4 Atmospheric predictability at convection-resolving scales

The chaotic nature of the atmosphere also implies intrinsic predictability limitations [e.g. Lorenz, 1963]. The predictability of a system is the degree of accuracy with which it is possible to predict its state in the near and distant future. Small-scale uncertainties which are inevitably present in numerical models amplify with time, leading to a divergence of initially nearby phase-space trajectories [Hohenegger and Schär, 2007].

Considerable effort has been made to comprehensibly quantify atmospheric predictability. Most of our current knowledge is based on studies in simplified settings, for example, using idealized numerical experiments [e.g. Lorenz, 1969; Métais and Lesieur, 1986; Rotunno and Snyder, 2008]. More recent studies employed either global or regional numerical models [e.g. Lorenz, 1982; Zhang et al., 2002; Tribbia and Baumhefner, 2004; Selz and Craig, 2015].

One common and widely used strategy to better understand predictability in the atmosphere is to run perturbation experiments (ensembles) to assess the evolution of differences within the simulations. In general, the ensemble mean exhibits better skills than a single (deterministic) integration, and the ensemble spread can serve as an indicator of the predictability of the system. This has led to the widespread use of ensemble prediction systems (EPSs; see e.g. Kalnay, 2003) in NWP. These differences are often limited to initial conditions, but also other aspects need to be considered. For example, regional models also require lateral boundary conditions, which constrain error growth at synoptic scales and lead to artificially enhanced predictability estimates [e.g. Errico and Baumhefner, 1987; Vukicevic and Errico, 1990]. Additional issues include uncertainties related to the model physics parameterizations [Ancell et al., 2018], the accuracy of numerical schemes, and the use of numerical diffusion [Knievel et al., 2007] and model-top damping [Klemp et al., 2008]. These uncertainties affect atmospheric predictability in full forecasting systems.

A recent study by Hohenegger and Schär [2007] addressing the issue of atmopsheric predictability in CRMs have shown that error growth rates are about 10 times larger at convection-resolving scales compared to synoptic scales. Moist convection is the principal process associated with this fast error growth [Zhang et al., 2003]. Although a rapid and unrealistic propagation of numerical noise ("chaos seeding"; see Ancell et al., 2018) may have led to excessively large error growth rate estimates, their result clearly shows that the limited atmospheric predictability at convection-resolving scales is a major limiting factor for CRMs.

1.3.5 The issue of convergence at the kilometer scale

The effective resolution in convection-resolving simulations was demonstrated to be limited by the horizontal rather than by the vertical grid spacing, provided that the vertical structure of the PBL is sufficiently well resolved [Bryan et al., 2003; Skamarock, 2004]. The limiting behavior of discretization schemes to reach the solution of a fixed set of governing equations at infinitely small Δx (and timestep) was addressed in the framework of the so-called *numerical convergence*. According to the Lax-Richtmyer theorem, a scheme is numerically convergent if it is stable and consistent [Lax and Richtmyer, 1956]. However, numerical models employ several different schemes each with a different order of convergence. Furthermore, several parameterizations include grid-dependent variables. Therefore, what in the literature (and in this thesis) is simply referred to as convergence is in fact *physical convergence* [Langhans et al., 2012c], that is, the insensitivity of flow statistics with respect to both the grid spacing and the flow physics.

Several studies have reported deficits in convection-resolving simulations due to the coarse horizontal grid [e.g. Petch et al., 2002; Bryan et al., 2003; Craig and Dörnbrack, 2008; Hanley et al., 2015; Dauhut et al., 2015]. In particular,

they have remarked that the analyzed statistics related to moist convection do not converge at the kilometer-scale. This has led several authors to question the physical validity of the convection-resolving approach. However, the focus of these studies was primarily on the structure and evolution of single cloud clusters or convective cells, which in this thesis is referred to as *structural convergence*. It is therefore questionable whether this is an appropriate convergence test for CRMs, since in climate projections the net effect of large ensembles of convective cells is considered. As for NWP, the issue of atmospheric predictability at convection-resolving scales discussed in Section 1.3.4 makes it clear that it is in general not possible that the spatial location and initiation time of each individual convective cell can be realistically and consistently simulated by a CRM.

In contrast, a study by Langhans et al. [2012c] paved the road for a new and more appropriate convergence test for kilometer-scale simulations. In the view of supporting the convection-resolving approach for regional-scale climate simulations, the authors focused on the convergence of large-scale tendencies related to an ensemble of convective cells in real-case simulations of thermally-driven convection over the Alps. They found that *bulk convergence* of domain-averaged and integrated properties can in general be achieved at the kilometer scale, despite some sensitivities related to the employed turbulence parameterization. If bulk convergence can be demonstrated, it means that the large-scale flow properties are not driven by eddy-resolving scales and are relatively unaffected by further refinement of the mesh grid. Similar results were obtained in idealized simulations of deep convection [Verrelle et al., 2015] and real-case simulations of a cold front [Harvey et al., 2017]. These findings lend support to the use of CRMs for climate projections.

1.4   Goals and outline of the thesis

A precise framework for a systematic comparison between bulk and structural convergence has not yet been established. The majority of the previous studies have focused solely on one of the two types of convergence. Moreover, all these previous studies left several important questions open. First, it is not clear whether bulk convergence is an intrinsic property of CRMs, since so far it has been demonstrated only in real-case simulations over mountainous terrain, i.e. in the presence of a pronounced mesoscale forcing from the orography and under the influence of the model external parameters, such as soil type, land use, etc.. Second, bulk convergence was obtained for the mean diurnal cycle of certain quantities, but nothing has been said regarding their spatial distribution. Furthermore, the previous analyses are based on single (deterministic) simulations, and thus it cannot be understood how the resolution sensitivity compares with, for instance, the model ensemble spread at convection-resolving scales. Third, there is still a lack of understanding regarding which approach is best to adopt to parameterize subgrid-scale tur-

bulence in CRMs, and how much this is important to determine the model resolution sensitivity, particularly with regard to the smallest simulated convective features.

This thesis aims to extend and complement the current knowledge on the resolution sensitivity and convergence behavior of convection-resolving simulations of summertime deep convection over land by setting the following overarching goals:

- To define a clear framework for a systematic comparison between structural and bulk convergence at convection-resolving scales;

- To establish whether or not bulk convergence is systematically achieved in convection-resolving simulations;

- To better understand the role of mesoscale forcing, and in particular thermally-driven wind systems, in determining the model resolution sensitivity and convergence behavior;

- To further investigate on the sensitivities related to subgrid-scale turbulence parameterization at the kilometer scale.

To these ends, idealized and real-case simulations with a state-of-the-art numerical model are run to address the following research questions:

1. How do structural and bulk convergence compare at convection-resolving scales?

2. Is bulk convergence robustly achieved in both idealized and real-case simulations? Can it be assessed also for the spatial distribution of the analyzed quantities, other than for their mean diurnal cycle?

3. Which physical processes or parameterizations foster convergence or yield a lower model resolution sensitivity?

4. How does the parameterization of subgrid-scale turbulence at the kilometer scale affect the mean flow properties and the characteristics of the individual convective cells?

These research questions are addressed in the following chapters:

Chapter 3: Convergence behavior of idealized convection-resolving simulations of summertime deep convection over land. [Panosetti et al., 2018, CD] Several previous studies have more or less explicitly questioned the physical validity of the convection-resolving approach by observing that the statistics related to single convective cells or cloud systems do not structurally converge until scales of $\mathcal{O}(100\,\mathrm{m})$ or even smaller. On the other hand, bulk convergence of domain-averaged and integrated quantities related to an ensemble of convective cells at the kilometer scale has been demonstrated

in real-case simulations over mountainous terrain. In this chapter a first-of-its-kind systematic comparison between bulk and structural convergence at convection-resolving scales is provided. Idealized simulations of deep convection over land are performed and a number of different experiments are conducted. Results show that bulk convergence is generally achieved at the kilometer scale for the domain-averaged surface rain rate, the integrated atmospheric heat and water vapor budgets, and for a few terms of the surface radiation budgets. This was observed in the presence and in the abscence of orography and environmental vertical wind shear, and also in simulations in which the land-surface and radiation schemes were switched off. On the other hand, despite the evidence of a lower resolution sensitivity for some statistics related to updraft velocity and convective mass fluxes, structural convergence is not achieved at the kilometer scale.

Chapter 4: Bulk and structural convergence at convection-resolving scales in real-case simulations of summertime moist convection over land. [Panosetti et al., 2019, QJRMS] This chapter extends the findings of Chapter 3 and previous studies by assessing bulk and structural convergence in real-case simulations. Bulk convergence is addressed not only for the mean diurnal cycle of precipitation, clouds and convective transport of mass, heat and water vapor, but also for the spatial distribution of their integrated values. A revised metric is employed which compares the resolution sensitivity with the model ensemble spread, as a measure to quantify atmospheric predictability, thus allowing for a more thorough assessment of bulk convergence. Two 9-day episodes of quasiperiodic thermally-driven orographic convection over the Alps and airmass convection over Central Germany are investigated to compare the results over mountainous and flat terrain. Results reveal that bulk convergence is systematically achieved for the spatial distribution of the analyzed quantities in both episodes. For their mean diurnal cycles, bulk convergence is generally observed in simulations over the Alps, but not over Central Germany, highlighting that a mesoscale orographic forcing reduces the resolution sensitivity of the bulk flow properties. On the other hand, structural convergence is confirmed to be not yet achieved at the kilometer scale.

Chapter 5: On the subgrid-scale turbulence parameterization at convection-resolving scales and sensitivities of the mean flow properties and characteristics of the individual convective cells. [Panosetti et al., 2019, MWR, in prep.] The partitioning between grid-scale and subgrid-scale variables is a major source of errors in convection-resolving simulations, which are able to explicitly simulate only a truncated portion of the continuous energy cascade. There is still disagreement on which approach it is best to adopt with regard to turbulence treatment at the kilometer scale. In this chapter we explore the sensitivities of the mean flow properties and

the characteristics of the individual convective cells to the employment of a 1D TKE-based turbulence parameterization devised for mesoscale modeling with grid-independent but tunable diffusivity and a 3D turbulence closure devised for LES at convection-resolving scales. Real-case simulations over the Alps and Central Germany are run to compare the results over flat and mountainous terrain. Results show that a less diffusive 1D model produces stronger convective cells, thicker clouds but reduced cloud cover, lower cloud base and more precipitation. These sensitivities are more pronounced at coarser resolutions and over flat terrain. A 3D closure yields excessive diffusion at grid spacings lof $\mathcal{O}(1\,\mathrm{km})$ and larger, suggesting that it should not be applied at such scales. However, the 1D and 3D models yield similar results at subkilometer scales, indicating that 3D closures perform reasonably well at scales larger for which they were designed for, and that they should in principle be employed at grid spacings of a few hundred meters or smaller.

Appendix A: Idealized large-eddy and convection-resolving simulations of moist convection over mountainous terrain. [Panosetti et al., 2016, JAS] On summertime fair-weather days, thermally-driven wind systems play an important role in determining the initiation and subsequent development of moist convection over mountainous terrain. This study compares the mechanisms of convection initiation and precipitation development within thermally-driven flows in idealized large-eddy (LES) and convection-resolving (CRM) simulations. Mass convergence and a weaker inhibition over the mountain tops combine with water vapor advection by upslope winds to initiate deep convection. In the CRM simulations, the spatial distribution of clouds and precipitation is generally well captured. However, if the mountains are high enough to force the thermally-driven flow into an elevated mixed layer, the transition to deep convection occurs faster, precipitation is generated earlier and in higher amounts compared to the LES. This is caused by stronger upslope winds due to weaker vertical turbulent mixing compared to the LES. The strength of the upslope winds and consequently the total accumulated precipitation in the CRM simulations is also found to be very sensitive to the choice of the turbulence scheme and to the employment of a shallow convection parameterization.

Appendix B: The influence of the resolution of topography and surface fields on the simulation of orographic moist convection. [Heim et al., 2019, MWR, in prep.] The degree of detail in the representation of topography and surface parameters at convection-resolving scales influences the simulation of moist convection, particularly over complex terrain such as the Alps. This study compares two sets of simulations with varying degree of detail in topography and surface fields and aims to analyze how this affects the initiation and development of convective cells within a thermally-driven flow. Results show major differences in the diurnal cycle of precipitation, in

the strength of thermally-driven flows and in the structure of the convective clouds. With a higher degree of details in the topography and surface fields convection is triggered later, its maximum intensity is reduced and it lasts for a longer time. Additional precipitation is generated by secondary convective cells during the night over the Po Valley. The single convective cells are weaker and smaller, but their number increases.

2

Convergence behavior of idealized convection-resolving simulations of summertime deep convection over land

Davide Panosetti[1], Linda Schlemmer[1], and Christoph Schär[1]

Abstract Convection-resolving models (CRMs) can explicitly simulate deep convection and resolve interactions between convective updrafts. They are thus increasingly used in numerous weather and climate applications. However, the truncation of the continuous energy cascade at scales of $\mathcal{O}(1\,\mathrm{km})$ poses a serious challenge, as in kilometer-scale simulations the size and properties of the simulated convective cells are often determined by the horizontal grid spacing (Δx).
In this study, idealized simulations of deep moist convection over land are

---

[1]Institute for Atmospheric and Climate Science, ETH Zurich, Universitätstrasse 16, 8092 Zurich, Switzerland

performed to assess the convergence behavior of a CRM at $\Delta x = 8$, 4, 2, 1 km and 500 m. Two types of convergence estimates are investigated: bulk convergence addressing domain-averaged and integrated tendencies related to the water and energy budgets, and structural convergence addressing the statistics and scales of individual clouds and updrafts. Results show that bulk convergence generally begins at $\Delta x = 4$ km, while structural convergence is not yet fully achieved at the kilometer scale, despite some evidence that the resolution sensitivity of updraft velocities and convective mass fluxes decreases at finer resolution. In particular, at finer grid spacings the maximum updraft velocity generally increases, and smaller and more numerous clouds are simulated. A number of different experiments are conducted, and it is found that the presence of orography and environmental vertical wind shear yields more energetic structures at scales much larger than Δx, sometimes reducing the resolution sensitivity.

Overall the results lend support to the use of kilometer-scale resolutions in CRMs, despite the inability of these models to fully resolve the associated cloud field.

2.1 Introduction

Deep convection is an important process in the atmosphere and a major component of the water and energy cycles. Due to the underlying complexity, state-of-the-art global climate models (GCMs) tend to do a poor job predicting the diurnal variability of deep convection [e.g. Dai and Trenberth, 2004]. Also in regional climate models the simulation of the triggering and evolution of deep convective cells makes up for a large part of their inaccuracy in simulating clouds and precipitation, particularly due to the employment of a convection parameterization scheme [e.g. Brockhaus et al., 2008; Barthlott et al., 2011].

In summertime and over land, deep convection often occurs in response to a pronounced diurnal cycle of solar radiation. The development of convective clouds is also tightly linked to the interplay between convection and mesoscale circulations, either generated by convection itself or by external factors such as surface heterogeneities [e.g. Hohenegger et al., 2015]. Secondary precipitation events can be triggered by cold pools driven by evaporative cooling of rain under deep convective clouds [e.g. Grabowski et al., 2006; Khairoutdinov and Randall, 2006; Böing et al., 2012; Schlemmer and Hohenegger, 2014]. Furthermore, the formation of clouds and the rainfall distribution over land are considerably influenced by the presence of mountains [e.g. Banta, 1984, 1990; Houze, 1993]. Previous studies observed that the Alpine region, due to its complex topography, enhances the precipitation over Central Europe [e.g. Frei and Schär, 1998]. Among others, convergence of upslope winds, which are driven by horizontal density gradients generated by differential surface heating between the mountain peaks and the surrounding flat terrain, is an

important convection initiation mechanism [e.g. Kirshbaum, 2011; Panosetti et al., 2016]. Cloud organization is another important contributing factor. The role of mountains [e.g. Kirshbaum and Grant, 2012] and environmental wind shear [e.g. Ludlam, 1980; Weisman and Klemp, 1982] in the organization process has long been known.

The increased computational resources available in recent years have allowed to establish convection-resolving models (CRMs: often referred to as convection-permitting or cloud-resolving models in the literature, see e.g. Prein et al., 2015) as a solid framework for idealized and real-case studies of deep moist convection. CRMs are models with horizontal grid spacings of $\mathcal{O}(1\,\mathrm{km})$. Several studies have shown that even at grid spacings as large as $4\,\mathrm{km}$ deep convection can be successfully modelled without a convection parameterization scheme [e.g. Weisman et al., 1997; Hohenegger et al., 2008; Baldauf et al., 2011]. Also due to their ability to resolve complex topographic structures, CRMs represent a particularly useful tool to simulate convective precipitation over land for both weather and climate applications. The use of CRMs is motivated by previous encouraging results in both numerical weather prediction [e.g. Done et al., 2004; Lean et al., 2008; Weisman et al., 2008; Schwartz et al., 2009] and regional-scale climate simulations [e.g. Hohenegger et al., 2008; Kendon et al., 2012; Ban et al., 2014]. Moreover, recent studies showed that decade-long CRM simulations are becoming feasible on continental scales [e.g. Prein et al., 2017; Leutwyler et al., 2016, 2017]. Limited-area numerical weather prediction models are nowadays run operationally by forecast centers with kilometer-scale resolution, e.g. over the UK with the UKV model at $1.5\,\mathrm{km}$ horizontal resolution since 2011 [Tang et al., 2013], over France with the AROME model at $1.3\,\mathrm{km}$ horizontal resolution since 2015 [Brousseau et al., 2016] and over Switzerland with the COSMO-Model at $1.1\,\mathrm{km}$ horizontal grid spacing since 2016 [Lapillonne et al., 2016]. CRMs have also been used within GCMs in the context of the so-called multiscale modeling framework or "superparameterization" [Grabowski, 2001; Randall et al., 2003] to simulate the interactions of an ensemble of convective elements with the large-scale flow.

However, the truncation of the continuous energy cascade at scales of $\mathcal{O}(1\,\mathrm{km})$ poses a serious challenge, as in kilometer-scale simulations the size and properties of the simulated convective cells are often determined by the horizontal grid spacing (Δx) [e.g. Langhans et al., 2012c]. The energy-containing turbulence scale ($1\,\mathrm{km}$ is a good order of magnitude for convective conditions) is of comparable size or even smaller than the typical horizontal grid spacing employed in CRMs [Zhou et al., 2014], and thus far away from resolved. Indeed, previous studies showed that a good representation of the energy cascade is key for obtaining convergence of flow structures for simulations using resolutions around or finer than the kilometer scale [e.g. Bryan et al., 2003; Ricard et al., 2013]. Furthermore, as explained in Wyngaard [2004], neither traditional LES turbulence closures nor one-dimensional vertical tur-

bulence schemes devised for mesoscale modeling are in principle applicable to CRMs, but nevertheless commonly employed. This is why modeling at the kilometer-scale is often referred to as modeling within the "grey zone" of deep moist convection [e.g. Craig and Dörnbrack, 2008].

Several studies have more or less explicitly questioned the physical validity of the convection-resolving approach. For example, Bryan et al. [2003] revealed that a simulation with $\Delta x = 1\,\text{km}$ did not produce equivalent squall-line structure and evolution as compared to $\Delta x = 125\,\text{m}$. Craig and Dörnbrack [2008] found that substantially higher resolution than the one used in CRMs is required to accurately simulate the transport, entrainment, and detrainment processes in evolving cumulus clouds. Hanley et al. [2015] showed that CRMs operating at horizontal grid spacings of $\mathcal{O}(1\,\text{km})$ have major shortcomings with regard to storm morphology. However, these studies focused primarily on the *structural convergence* of statistics related to single thermals or single cloud systems.

In contrast to these previous studies Langhans et al. [2012c] assessed the *bulk convergence* of regional-scale properties in real-case convection-resolving simulations of summertime deep convection over the Alps. In their study they considered domain-averaged and integrated quantities over a large $(970 \times 515\,\text{km}^2)$ analysis domain for a 9-day period of reoccurring thermally-driven convection with very weak large-scale forcing. Their findings showed that bulk convergence can begin at grid spacings as large as $4.4\,\text{km}$ for a number of variables related to deep convection. When bulk convergence is achieved, the feedbacks between convection and the larger scale are only marginally affected by further refinements of the mesh grid.

Although the results of Langhans et al. [2012c] clearly support the feasability of kilometer-scale simulations, a number of open questions were left behind. First, it is not clear whether their results are specific to mountainous regions, or can be generalized to flat terrain. Second, it is not evident that bulk convergence can be obtained for smaller domain sizes or shorter time periods than the one considered in their study. Third, the complexity of a real-case setup does not allow to identify those physical processes or parameterizations which determined the model resolution sensitivity or eventually contributed to achieving bulk convergence.

In this paper we compare bulk convergence of domain-averaged and integrated properties of a large ensemble of convective cells against structural convergence of pooled grid-point statistics related to individual clouds and updrafts. The the Consortium for Small-Scale Modeling (COSMO) model is run in idealized setups to study the diurnal cycle of convection and precipitation over land. A number of different experiments are conducted to identify those physical processes or parameterizations which foster convergence or yield a lower resolution sensitivity.

The numerical model and the experimental design are presented in Section 2.2. In Section 2.3, the methodology used to compute the heat and water va-

por budgets and the relevant statistics used to address bulk convergence are described. In Section 2.4.1, the flow structure and evolution in the different experiments is discussed. In Section 2.4.2 bulk convergence is investigated looking at the domain-averaged surface rain rate, surface radiation balance and integrated atmospheric heat and water vapor tendencies. In Section 2.4.3 structural convergence is addressed considering the statistical distributions of updraft velocity, convective mass flux and cloud horizontal area. The summary and discussion are given in Section 2.5.

2.2   Model description

2.2.1   Model

For this study we use version 5.0 of the Consortium for Small-Scale Modeling Model (COSMO-Model; Baldauf et al., 2011). The COSMO-Model is a non-hydrostatic, fully compressible limited-area atmospheric prediction model, designed for both operational high-resolution numerical weather prediction (NWP) and research applications on a broad range of spatial scales. The model is used in different configurations for operational numerical weather prediction purposes at several European weather services, and has been further developed into a regional climate modeling system [Rockel et al., 2008]. The time integration is performed with a third-order Runge-Kutta scheme [Klemp and Wilhelmson, 1978; Wicker and Skamarock, 2002]. A fifth-order advection scheme is used for temperature, pressure, and horizontal and vertical winds, and a second-order scheme [Bott, 1989] is employed for horizontal advection of moist quantities. The parameterizations include a radiative transfer scheme based on the δ-two-stream approach [Ritter and Geleyn, 1992], in which radiation interacts with both subgrid- and grid-scale clouds, and a single-moment bulk microphysics scheme with three ice categories (ice, snow, graupel) after Reinhardt and Seifert [2006].

A 1.5-order scheme based on a prognostic equation for the turbulent kinetic energy (TKE) [Raschendorfer, 2001] with a level 2.5 closure [Mellor and Yamada, 1974, 1982] is used to compute the vertical eddy viscosities for heat K_h^V and momentum K_m^V. $K_{h,m}^V$ are determined using the Prandtl-Kolomogorov specification as:

$$K_{h,m}^V = \phi_{h,m} l_v \sqrt{2\bar{e}} \tag{2.1}$$

The characteristic length scale l_v for vertical mixing is calculated according to [Blackadar, 1962]:

$$l_v = \frac{kz}{1 + (kz)/l_\infty} \tag{2.2}$$

where k is the von-Karman constant, z the altitude, and l_∞ is an asymptotic length scale which is set to 60 m. $\phi_{h,m}$ are stability-dependent coefficients, and $\bar{e} = (\overline{u_i' u_i'})/2$, with $i = 1, 2, 3$, is the subgrid TKE per unit mass. The overbar denotes a time mean. The prime indicates a subgrid-scale variable.

Following Pope [2000] the eddy viscosities for second-order horizontal diffu-
sion $K_{h,m}^H$ are related to the three-dimensional grid-scale rate of strain as:

$$K_{h,m}^H = l_h^2 \sqrt{[2(D_{11} + D_{22} + D_{33})^2 + 4(D_{12}^2 + D_{13}^2 + D_{23}^2)]} \qquad (2.3)$$

$$D_{ij} = \frac{1}{2} \left(\frac{\partial u_i}{\partial x_j} + \frac{\partial u_j}{\partial x_i} \right) \qquad (2.4)$$

where D_{ij} is the grid-scale rate of strain [Langhans et al., 2012a]. The tur-
bulent length scale for horizontal mixing $l_h = c_s \sqrt{\Delta x \Delta y}$ is related to the
horizontal grid spacing, where $c_s = 0.25$ is the Smagorinski constant.
The atmospheric part of the system is coupled to the second-generation, 10-
layer land surface model TERRA_ML [Heise et al., 2003] which provides
values of surface temperature and specific humidity. A Louis surface trans-
fer scheme [Louis, 1979] is used to calculate the transfer coefficients which
yield the surface sensible and latent heat fluxes based on Monin-Obukhov
Similarity Theory.

2.2.2 Setup

The horizontal domain covers $200 \times 200 \, \text{km}^2$. The model uses a generalized
smooth level vertical (SLEVE) coordinate [Schär et al., 2002; Leuenberger
et al., 2010] with 79 vertical levels. The vertical grid spacing varies from
20 m near the surface to 800 m above 18 km. The model top is located at
21 km. 10 soil layers are used with varying thickness from 1 cm for the upper-
most layer to 5.76 m for the lowermost, and the soil total depth is 15.34 m.
Soil parameters and vegetation characteristics are prescribed using values
from simulations of diurnal convection in a mid-European climate [Schlem-
mer et al., 2011]. We conduct simulations at $\Delta x = 8, 4, 2, 1 \, \text{km}$ and 500 m.
The time steps used are 60, 30, 20, 10 and 5 s respectively. 2D and 3D fields
are written to file every 6 minutes before postprocessing, to ensure high res-
olution output data in time. The model is run for 6 days, but the analysis
is based only on the last 5 days of simulation to allow the model to develop
sufficient spatial heterogeneity. The lateral boundary conditions are periodic
in both horizontal directions. At the upper domain boundary a rigid lid is
employed, and a Rayleigh damping layer extends from 11.5 km to the top of
the domain to minimize spurious reflections of gravity waves. The Coriolis
force is set to zero. To break the symmetry of the initial fields, the temper-
ature is disturbed at the lowest model level with random perturbations of
$\pm 0.02 \, \text{K}$. Incoming solar radiation is uniformly distributed on the entire do-
main and is determined for 48.25°N, 0°E (which is comparable to the Black
Forest region in Central Europe) on 12 July 2006 following Schlemmer et al.
[2011].
The case is based upon the setup introduced by Schlemmer et al. [2011]. The
topographic altitude is set to 500 m. The idealized initial temperature and
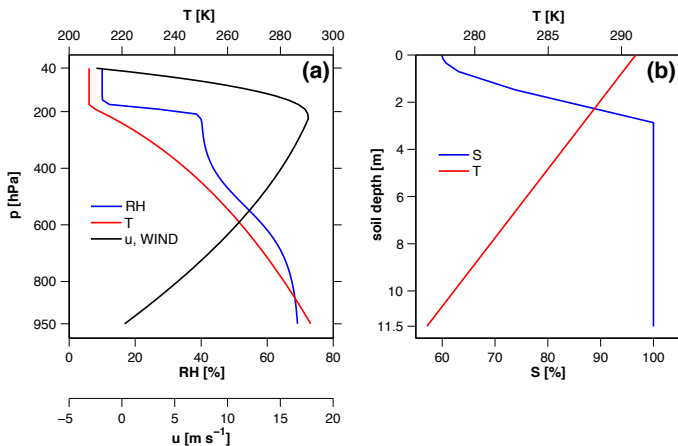
Figure 2.1: Initial profiles of (a) atmospheric temperature (T [K], red line), relative humidity (RH [%], blue line) and horizontal wind speed (u [m s^{-1}], black line) in WIND and (b) soil saturation (S [%], blue line) and soil temperature (T [K], red line).

Experiment	Setup
CTRL	standard setup
MOUNTAIN	CTRL + 3D gauss mountain
WIND	CTRL + env. wind shear
PRESCR	CTRL w. prescr. sfc. fluxes
PRESCR_NORAD	PRESCR w.o. rad. scheme

Table 2.1: List of experiments and different configurations.

moisture profiles (Fig. 2.1a, red and blue lines) are representative of summertime European climatological conditions. To obtain a conditionally unstable stratification, a lapse rate of -7 K km^{-1} is considered for tropospheric temperature, with a surface temperature of 291 K. The relative humidity is 70% close to the surface and decreases up to 40% in the upper troposphere. The reference soil moisture saturation (Fig. 2.1b, blue line) is 60% at the surface and increases to 100% at the depth of 2.50 m. The soil temperature (Fig. 2.1b, red line) is set to 291 K and linearly decreases to 277 K at the depth of 11.50 m.

The experiments and the different configurations are listed in Table 2.1. In the control experiment (CTRL) the model is run as described above over flat terrain and with zero horizontal wind. To compare the convergence behavior over flat and mountainous terrain, in MOUNTAIN a three-dimensional moun-

tain is placed in the center of the model domain and defined by a circular Gaussian function:

$$h(x, y) = He^{-\frac{x^2 + y^2}{A^2}} \tag{2.5}$$

where $H = 500\,\text{m}$ is the mountain height and $A = 20\,\text{km}$ is the mountain half-width. Since the employed land-surface model neglects lateral water transport, in MOUNTAIN the saturation of the soil layer is kept constant throughout the entire simulation to prevent unrealistically high values of soil moisture over the mountain due to the high precipitation amounts. To test the sensitivity to the presence of environmental vertical wind shear, in WIND the zonal wind is set to $0\,\text{m s}^{-1}$ at the surface, increases to $17.5\,\text{m s}^{-1}$ at the tropopause, and decreases again to $-3\,\text{m s}^{-1}$ in the stratosphere (Fig. 2.1a, black line). In PRESCR the model is run with the same configuration of CTRL but the soil model is switched off. The surface fluxes are prescribed using a sine function for an available energy of $460\,\text{W m}^{-2}$ at the diurnal maximum split into latent and sensible heat flux with a Bowen ratio of 0.5. In PRESCR_NORAD the radiation scheme is also switched off and a homogeneous cooling rate of $2.5\,\text{K day}^{-1}$ is prescribed throughout the entire atmospheric column. Each experiment consists of five ensemble members constructed using different initial random temperature perturbations at the lowest model level. Ensemble-averaged quantities are used only for the analysis of bulk convergence, and in what follows are denoted by the asterisk (*).

2.3 Methodology

2.3.1 Heat and water vapor budget formulation

To study the convergence of bulk flow properties, the heat and water vapor budgets for a large control volume covering the entire model domain in the horizontal are investigated. The top of the control volume is located at 4000 m height. Recalling that the model boundaries are periodic, the volume-averaged tendencies are thus representative of deep convective fluxes toward the upper atmosphere.

The processes contributing to the instantaneous local heating and cooling of the atmosphere are given by:

$$\frac{\partial \theta}{\partial t} = -\mathbf{v} \cdot \nabla \theta - \frac{1}{\rho c_p} (\nabla \cdot \mathbf{H}) - \frac{1}{\rho c_p} (\nabla \cdot \mathbf{R}) + L_m \tag{2.6}$$

where θ is the potential temperature, $\mathbf{v}$ the wind speed vector, ρ is the air density, c_p is the heat capacity at constant pressure, $\mathbf{H} = \rho c_p \overline{\mathbf{v}' \theta'}$ is the subgrid-scale sensible heat flux, $\mathbf{R}$ is the radiative energy flux, and L_m is the latent heating rate. All the terms in Eq. 2.6 are extracted using the budget tool implemented in the COSMO-Model [Langhans et al., 2012b].

To study the convergence of the bulk tendencies, the net effect of each process

is computed on a control volume V of total mass $M = \int_V \rho dV$ by integrating Eq. 2.6 over V. The volume-averaged density-weighted heat budget equation is:

$$\underbrace{\frac{1}{M} \int_V \rho \frac{\partial \theta}{\partial t} dV}_{\text{TOT}} = \underbrace{-\frac{1}{M} \int_V \rho \mathbf{v} \cdot \nabla \theta \, dV}_{\text{ADV}} + \underbrace{\frac{1}{M} \int_V -\frac{1}{c_p} (\nabla \cdot \mathbf{H}) dV}_{\text{UNRES}}$$

$$+ \underbrace{\frac{1}{M} \int_V -\frac{1}{c_p} (\nabla \cdot \mathbf{R}) dV}_{\text{RAD}} + \underbrace{\frac{1}{M} \int_V \rho L_m \, dV}_{\text{MIC}} \quad (2.7)$$

where TOT is the heat storage tendency, ADV is the heat advection, UNRES is the subgrid-scale sensible heat flux convergence, RAD is the radiative heat flux convergence and MIC is the microphysics contribution (primarily latent heat exchange due to condensation of water vapor and evaporation of rain). Similar to the heat budget equation, the water vapor budget equation can be written in its volume-integrated density-weighted form as:

$$\underbrace{\frac{1}{M} \int_V \rho \frac{\partial q_v}{\partial t} dV}_{\text{TOT}} = \underbrace{-\frac{1}{M} \int_V \rho \mathbf{v} \cdot \nabla q_v \, dV}_{\text{ADV}} + \underbrace{\frac{1}{M} \int_V -\frac{1}{l_v} (\nabla \cdot \mathbf{L}) dV}_{\text{UNRES}}$$

$$+ \underbrace{\frac{1}{M} \int_V \rho S_m \, dV}_{\text{MIC}} \quad (2.8)$$

where TOT is the water vapor storage tendency, ADV is the water vapor advection, UNRES is the subgrid-scale latent heat flux convergence and MIC is the microphysics contribution. q_v is the specific water vapor, l_v is the latent heat of vaporization, $\mathbf{L} = \rho l_v \overline{\mathbf{v}' q_v'}$ is the subgrid-scale latent heat flux, and S_m are microphysical source/sink rates.

2.3.2 Bulk convergence statistics

Since convection is similar to a stochastically random process in space and time, convergence analysis of bulk quantities must include some averaging. Therefore, the 5-day mean (in space and time, where the space averaging is taken over the entire computational domain) diurnal cycles of each ensemble member are considered. Consistently with Langhans et al. [2012c], to study the convergence of bulk flow properties the root-mean-squared difference ($RMSD_{\Delta x}^{i,j}$) between the diurnal cycle of a quantity ψ simulated with horizontal grid spacing Δx and $\Delta x/2$ is computed for each ensemble member

i (for Δx) and j (for $\Delta x/2$) as:

$$RMSD_{\Delta x}^{i,j} = \sqrt{\frac{1}{N} \sum_{n=1}^{N} [\psi_{\Delta x}^{i}(n) - \psi_{\Delta x/2}^{j}(n)]^2} \qquad (2.9)$$

where n is a specific time of the diurnal cycle, and $N = 240$ for output data every 6 minutes. Equation 2.9 can be interpreted as the simulation increment when moving from some resolution Δx to $\Delta x/2$. The ensemble-average $RMSD$ ($RMSD_{\Delta x}^{*}$) is then computed for each horizontal grid spacing Δx as:

$$RMSD_{\Delta x}^{*} = \frac{\sum_{i,j=1}^{E} RMSD_{\Delta x}^{i,j}}{E^2} \qquad (2.10)$$

where $E = 5$ is the number of ensemble members.

Finally, the ensemble-average normalized resolution increment ($NRI_{\Delta x}^{*}$, expressed in percent [%]) is computed for each horizontal grid spacing Δx by dividing $RMSD_{\Delta x}^{*}$ by the ensemble-averaged reference value as simulated by the highest-resolution run at $\Delta x = 500\,\mathrm{m}$ (ψ_{500}^{*}):

$$NRI_{\Delta x}^{*} = \frac{RMSD_{\Delta x}^{*}}{\psi_{500}^{*}} = \frac{RMSD_{\Delta x}^{*}}{\frac{\sum_{i=1}^{E} \frac{1}{N} \sum_{n=1}^{N} |\psi_{500}^{i}(n)|}{E}} \times 100 \qquad (2.11)$$

With this statistics the aim is to consider all the possible available different realizations between Δx and at $\Delta x/2$. Since each experiment at each horizontal resolution has five ensemble members, the total number of possible realizations is 25. Ensemble-average statistics give an idea of the robustness of the obtained results. The statistics must be interpreted as follows: the higher the value of $NRI_{\Delta x}^{*}$, the larger the difference between the diurnal cycles of that specific quantity simulated at Δx and at $\Delta x/2$. Note that $NRI_{\Delta x}^{*}$ is sensitive to both differences in amplitude and phase of the diurnal cycle. In the view of supporting the convection-resolving approach, one should generally hope for low values of $NRI_{\Delta x}^{*}$, which would be an indication of small differences between the simulated diurnal cycles at Δx and at $\Delta x/2$. A convergent behavior would be seen as a systematically decreasing $NRI_{\Delta x}^{*}$ as the finest horizontal grid spacing is approached.

2.4 Results

This section is divided into three parts. First some general characteristics of the simulations are described. Then, the bulk convergence of domain-averaged and integrated variables related to a large ensemble of convective cells is discussed. Finally, structural convergence of pooled grid-point statistics of individual clouds and updrafts is addressed.
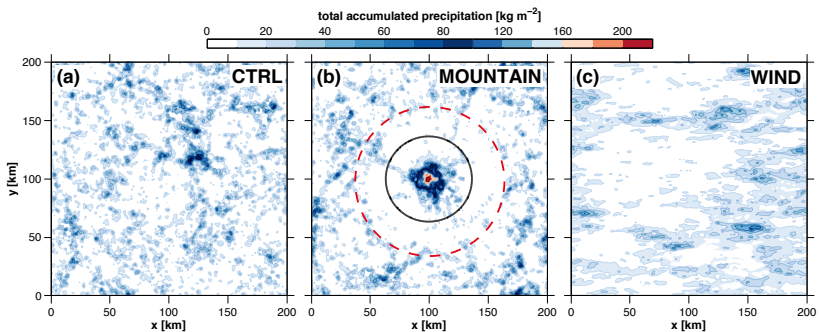
Figure 2.2: Spatial distribution of the 5-day total accumulated precipitation [kg m^{-2}] at $\Delta x = 500\,\text{m}$ in (a) CTRL, (b) MOUNTAIN and (c) WIND. The mountain topography in MOUNTAIN (black contours at 50 m height) is displayed in (b). The dashed red line in (b) identifies the near (within the circle) and far (outside the circle) fields.

2.4.1 Flow structure and evolution

To document the flow structure and evolution in the different experiments, the spatial distribution of the 5-day total accumulated precipitation is shown in Fig. 2.2. The flow evolution of PRESCR and PRESCR_NORAD is not shown because it is qualitatively similar to the one of CTRL. The rainfall in CTRL is rather homogeneously distributed. The plots of MOUNTAIN and WIND are markedly different from those of CTRL. In WIND precipitation organizes in larger-scale, band-like structures. In MOUNTAIN a zone of enhanced precipitation exists over the mountain, followed by an area of significantly reduced rainfall around the mountain (near-field). Finally, the total rainfall amounts increase again near the model boundaries (far-field). The dashed red line in Fig. 2.2b identifies these two regions.

Figure 2.3 illustrates the flow evolution in the morning and early afternoon hours in the three same experiments. In CTRL small-scale convective structures are observed in the morning hours. Clouds are homogeneously distributed over the model domain, with some degree of organization and clustering due to precipitation-driven cold pools, particularly in the afternoon. In MOUNTAIN the morning flow is characterized by a mesoscale circulation associated with the presence of the mountain in the center of the model domain. The updraft branch of this circulation and associated clouds are centered over the mountain summit. In the early afternoon and after the first precipitation event over the mountain summit, a large-scale cold pool is located in the center of the model domain. The propagation of the cold pool significantly reduces upward motion in the near-field as compared to the far-field [e.g. Hassanzadeh et al., 2015], which explains the rainfall distribution observed in Fig. 2.2b. In WIND a substantially higher degree of convective
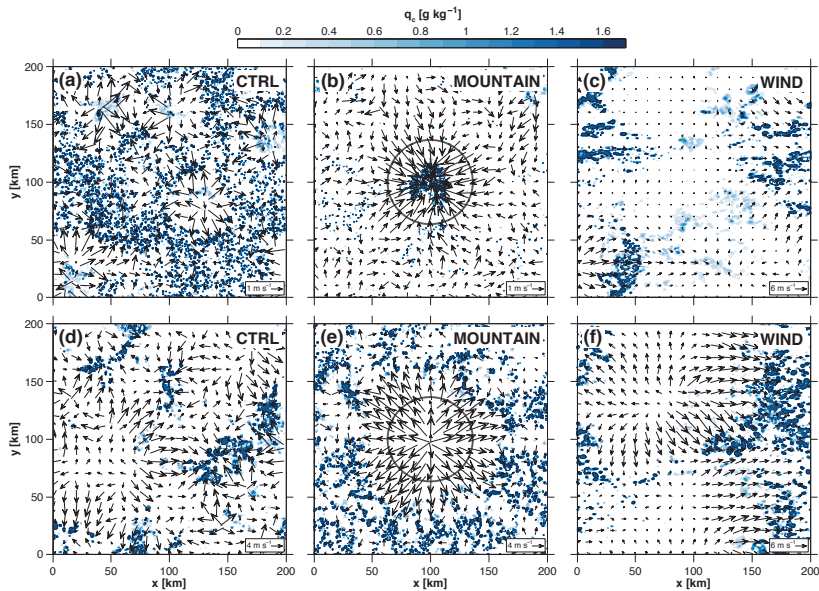
Figure 2.3: Horizontal wind speed [m s^{-1}] at the lowest model level (black vectors: the reference vector is displayed at the bottom right corner of each panel) and total cloud liquid water content in the atmospheric column (q_c [g kg^{-1}], color scale) at $\Delta x = 500$ m at (a-c) 11 LT and at (d-f) 14 LT of the first simulation day in (a,d) CTRL, (b,e) MOUNTAIN and (c,f) WIND. The horizontal wind speed is computed as a running hourly average centered 30 min before the displayed time to show the mean circulation and to account for the time response of deep convection to the surface forcing.

organization compared to CTRL is observed, which is consistent with the precipitation distribution in Fig. 2.2c. Clouds cluster into larger-scale structures already in the morning hours.

To better understand the scales involved in the flow evolution in the different experiments, power spectral densities (PSDs) of vertical wind and cloud liquid water mixing ratio at 6000 m height and horizontal velocity at the first model layer are computed and shown in Fig. 2.4. The horizontal velocity PSDs are indicative of the length scales of the surface forcing. The PSDs are averaged between 11 LT and 18 LT to capture the more active period of convection. The spectral representation of the topography in MOUNTAIN is included to visualize the dominant length scales imposed by the mountain. In WIND vertical motion is reduced at the small scale and there is more energy at the large scale compared to the other experiments. A similar behavior is observed for the cloud liquid water mixing ratio, consistently with the plots of Figs. 2.3c and 2.3f, but not for the PSD of horizontal velocity, which indicates that the large scales imposed in the simulation do not come from a forcing at the surface. Note that the energy peak at around 5 km in the PSD of horizontal velocity is approximately at the same length scale of the one in the PSD of vertical velocity (cf. Fig. 2.4a), and thus indicative of the characteristic size of the horizontal branch of the dominant convective motions in WIND.

In contrast, the PSD of horizontal velocity in MOUNTAIN shows a distinct peak at the very large scale (greater than 100 km). At those scales the mountain imposes energies of several orders of magnitude greater than at smaller scales (cf. Fig. 2.4d). On the other hand, no excess of energy at the same very large scale is observed in the PSDs of vertical velocity and cloud liquid water mixing ratio, suggesting that the larger scales imposed in the simulation in MOUNTAIN do come primarily from the mesoscale (horizontal) flow at the surface associated with the orography. This is in line with Barthlott et al. [2011], who noted that the vertical branch of the large-scale circulation imposed by the mountain collapses into the finescale.

Figures 2.5a-e show the vertical profiles of the mean diurnal cycle of convective mass flux in the different experiments. To illustrate only the upward mass transport by the convective clouds, the convective mass flux M_c is computed as:

$$M_c = \frac{1}{A} \int \rho w \, dx dy, \quad w > 1 \, m \, s^{-1}, \quad q_c > 10^{-6} \, kg \, kg^{-1} \qquad (2.12)$$

where A is the model domain, w is the vertical velocity, and q_c is the specific cloud liquid water content. The vertical distribution of the total convective mass flux is illustrated in Fig. 2.5f. Although the cloud base is slightly higher in PRESCR, the diurnal cycles in CTRL, MOUNTAIN, WIND and PRESCR are very similar, with a maximum between 12 LT and 13 LT located at a height of about 3000 m. On the other hand, in PRESCR_NORAD
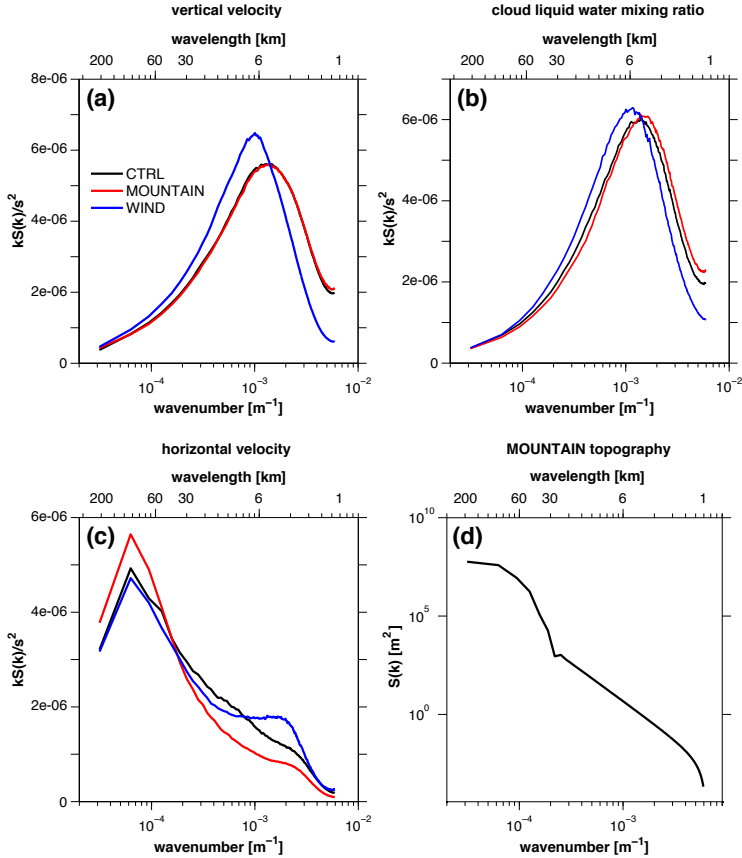
Figure 2.4: Normalized power spectral densities (PSDs) averaged between 11 LT and 18 LT of (a) vertical velocity, (b) cloud liquid water mixing ratio and (c) horizontal velocity at (a) and (b) 6000 m height and (c) the first model level at $\Delta x = 500$ m in CTRL, MOUNTAIN and WIND. (d) PSD of topography at $\Delta x = 500$ m in MOUNTAIN. The curves in (a-c) are normalized by the total variance, so that their integrals amount to unity. The PSDs of horizontal velocity are computed as an average between their latitudinal and longitudinal components.
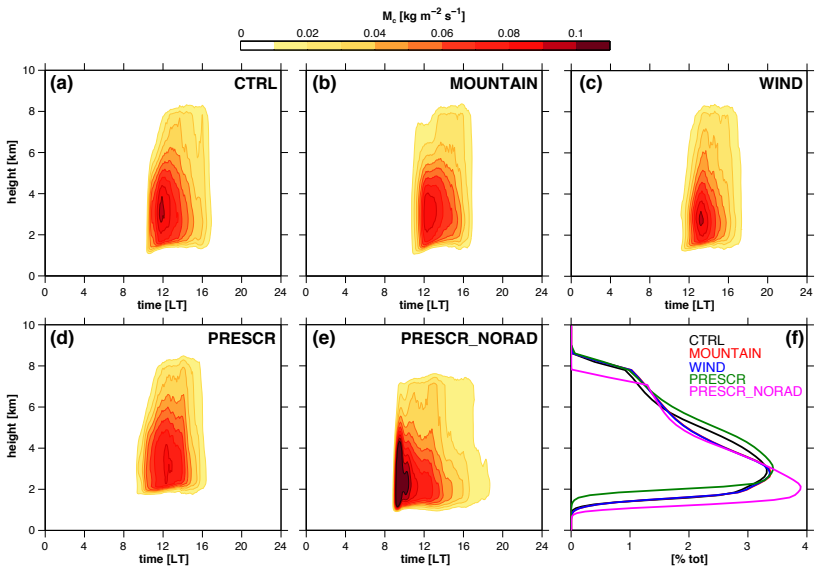
Figure 2.5: Vertical profiles of the mean diurnal cycle of domain-averaged convective mass flux (M_c [kg m^{-2} s^{-1}], see Eq. 2.12) at $\Delta x = 500$ m for (a) CTRL, (b) MOUNTAIN, (c) WIND, (d) PRESCR and (e) PRESCR_NORAD. The display threshold is 0.01 kg m^{-1} s^{-2}. **f** Vertical distribution of total convective mass flux (expressed in percent [%]).
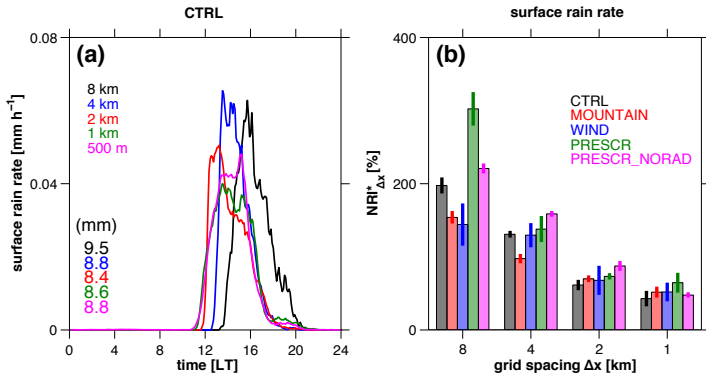
Figure 2.6: (a) Mean diurnal cycle of domain-averaged surface rain rate $[\mathrm{mm\,h^{-1}}]$ in CTRL. The total accumulated precipitation [mm] is displayed at the bottom left of the panel. (b) Ensemble-averaged normalized resolution increment ($NRI^*_{\Delta x}$ [%], see Eq. 2.11) versus the horizontal grid spacing (Δx) computed for the surface rain rate. The bars indicate the ensemble spread for each experiment, defined as the standard deviation.

the diurnal cycle is characterized by a sharp maximum earlier in the morning, and at a height of about 2000 m. Furthermore, the cloud base is much lower compared to all the other experiments. These are indications of a more explosive convective activity, possibly resulting from the prescribed homogeneous radiative cooling and associated destabilization of the atmospheric column.

2.4.2 Bulk convergence

In this section bulk convergence is investigated for domain-averaged and integrated variables related to deep moist convection. A detailed description and interpretation of the analysis method and involved statistics is given in Section 2.3.2. Since the mean diurnal cycles of the analyzed variables are similar in the different experiments, only the ones for CTRL are shown, but the bulk convergence behavior is analyzed and presented for all cases.

Figure 2.6a shows the mean diurnal cycle of domain-averaged surface rain rate in CTRL. The accumulated precipitation of each simulation is indicated at the bottom left of the panel. All simulations generate precipitation peaking in the afternoon, although the maximum is less intensive at finer grid spacings. Precipitation is generated earlier at higher resolution, and a phase shift of more than two hours is observed in the initiation time between the 500-m and 8-km simulations. This is explained by the fact that it takes more time to saturate a very large grid box. The 8-km run produces slightly more precipitation, whereas at all the other resolutions the precipitation totals are similar. Figure 2.6b illustrates the $NRI^*_{\Delta x}$ computed versus the horizontal
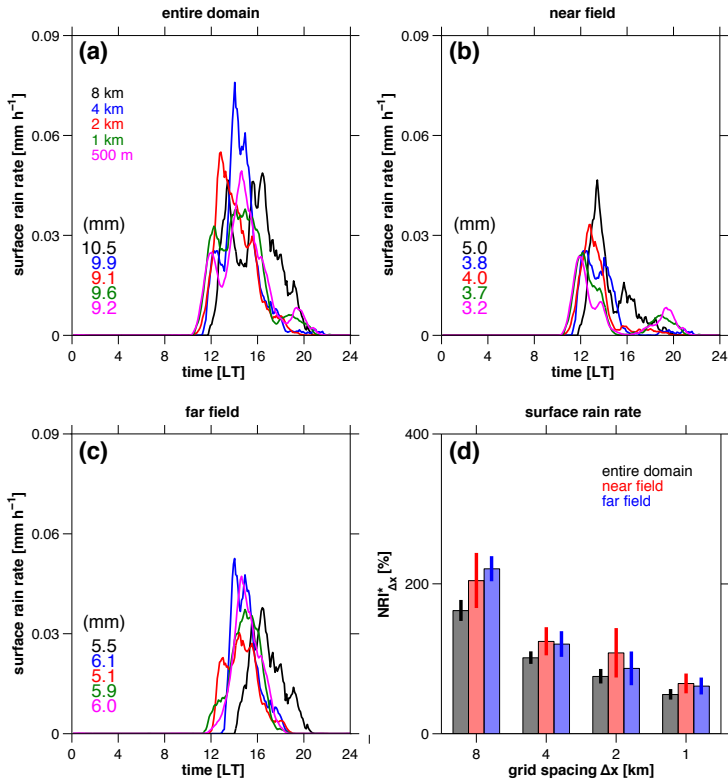
Figure 2.7: (a-c) As Fig. 2.6a but for MOUNTAIN for (a) the entire domain, (b) the near field and (c) the far field. The different regions are illustrated in Fig. 2.2b. (d) As Fig. 2.6b but for the different regions identified for MOUNTAIN in Fig. 2.2b.

grid spacing Δx for the surface rain rate in the different experiments. The bars indicate the ensemble spread for each experiment. All simulations systematically converge toward the 500-m solution. Smaller values of the $NRI^*_{\Delta x}$ are observed for MOUNTAIN and, to a lesser extent, for WIND compared to CTRL for the coarser resolutions, indicating lower sensitivities to Δx at those scales. On the other hand, slightly larger sensitivities to the horizontal grid spacing are in general observed for PRESCR and for PRESCR_NORAD compared to CTRL at all resolutions.

To better understand the dynamics over mountainous terrain and quantify the relative contributions of the near and far fields to the bulk convergence behavior observed in MOUNTAIN, a separate analysis is conducted for the average surface rain rate over three different domains: the entire domain, the

near field (the region within the red circle in Fig. 2.2b) and the far field (the region outside the red circle in Fig. 2.2b). The regions have been identified based on the mountain influence on the total accumulated precipitation (see Section 2.4.1). To compensate for the smaller domain considered, the analysis for the near and far fields is based on eight (rather than five) ensemble members to cover roughly the same number of convective cells in the analysis.

Figures 2.7a-c show the mean diurnal cycle of domain-averaged surface rain rate over the different regions identified in MOUNTAIN. Whereas the total precipitation amount is comparable for the two different regions, there are pronounced differences in the diurnal cycle. Within the near field two separate precipitation events are identifiable (cf. Fig. 2.7b), and they occur as a result of thermally-driven convection over the mountain summit. Due to a poor representation of the mountain and associated thermally-driven circulations at coarser resolutions, the secondary precipitation event is simulated only at $\Delta x = 1\,\mathrm{km}$ and $500\,\mathrm{m}$. This is consistent with what has been observed in e.g. Hohenegger et al. [2015] or Panosetti et al. [2016]. Although the initial large-scale forcing and thus the initiation of the first precipitation event over the mountain are successfully captured even at coarse resolutions, the model shows large sensitivity to the grid spacing in representing the coupling between convection and circulation in the afternoon. Note that the secondary precipitation event observed in the 8-km run, which is in phase with the observed afternoon surface rain rate peak in the far field (cf. Fig. 2.7c), does not occur in response to the thermally-driven circulations but rather to the diurnal cycle of solar radiation. This is possibly a result of a poor representation of the mountain and associated upslope and downslope wind systems (cf. Fig. 2.3) due to the very coarse grid.

Over the far field precipitation occurs uniquely in the afternoon hours (cf. Fig. 2.7c) and is primarily driven by cold-pool related convective activity similarly to CTRL. Although there is a better agreement between the different resolutions in the total precipitation amount compared to the near-field, the shift in the initiation timing is much more pronounced.

Figure 2.7d illustrates the $NRI^*_{\Delta x}$ computed versus the horizontal grid spacing Δx for the surface rain rate in the different regions. Although the magnitudes are not directly comparable to one another, convergence toward the 500-m solution is systematically observed for all regions.

Figure 2.8 illustrates the average diurnal cycle of the surface radiation balance. This can be defined as:

$$G = Q_{SW} + Q_{LW} + H + E \tag{2.13}$$

where Q_{SW} is the net shortwave radiation at the surface, Q_{LW} is the net longwave radiation at the surface, H and E are the surface sensible and latent heat fluxes, and G is the ground heat flux. The large differences observed in Q_{SW} are explainable by the considerable phase shift in the diurnal cycle of
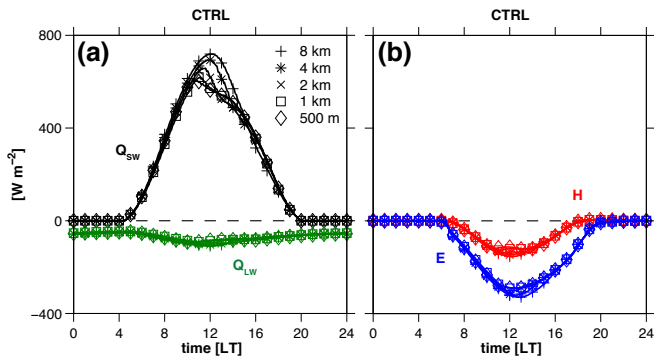
Figure 2.8: Mean diurnal cycles of (a) surface net shortwave (Q_{SW} [W m^{-2}], black lines) and net longwave (Q_{LW} [W m^{-2}], green lines) radiation and (b) sensible (H [W m^{-2}], lines) and latent (E [W m^{-2}], blue lines) heat flux in CTRL. The markers distinguish between the different horizontal grid spacings.

convection and related cloud cover across the different resolutions: for example, at $\Delta x = 8$ km clouds are triggered long after the maximum solar heating.

Figure 2.8 shows the $NRI^*_{\Delta x}$ computed for each of the four terms of the rhs of Eq. 2.13 in the different experiments. The analysis cannot be performed for PRESCR_NORAD because the radiative transfer scheme is switched off. For PRESCR the $NRI^*_{\Delta x}$ is computed only for Q_{SW} and Q_{LW} since the surface fluxes are prescribed. Although the values of the $NRI^*_{\Delta x}$ are considerably smaller compared to Fig. 2.6b for the surface rain rate, starting at $\Delta x = 4$ km the $NRI^*_{\Delta x}$ generally decreases toward smaller grid spacings for Q_{SW} and E, suggesting the beginning of convergence at those scales. The same does not hold for Q_{LW} and H, since the sensitivity to the horizontal grid spacing does not systematically change at smaller Δx. However, for most of the terms the resolution sensitivity is relatively close to the ensemble spread, which makes it hard to assess whether convergence is actually achieved or not. In particular, the largest ensemble spread is observed for WIND, especially at coarse resolution. This is possibly the result of the observed larger cloud clusters, for which small differences in the simulated structure and evolution can lead to substantial ones in the net surface radiation balance.

Finally, to quantify the relative contribution of the different terms in the heat (Eq. 2.7) and water vapor (Eq. 2.8) budget equations to the net heating and moistening of a control volume covering the entire horizontal domain and with a rigid top at 4000 m height (see Section 2.3.1 for a detailed description of the budget), the mean diurnal cycle of specific heat and water vapor tendencies within the control volume is shown in Fig. 2.10. In the morning until 7 LT and in the evening after 18 LT a net cooling of the control volume is observed as a result of radiative cooling. After 7 LT the atmosphere warms
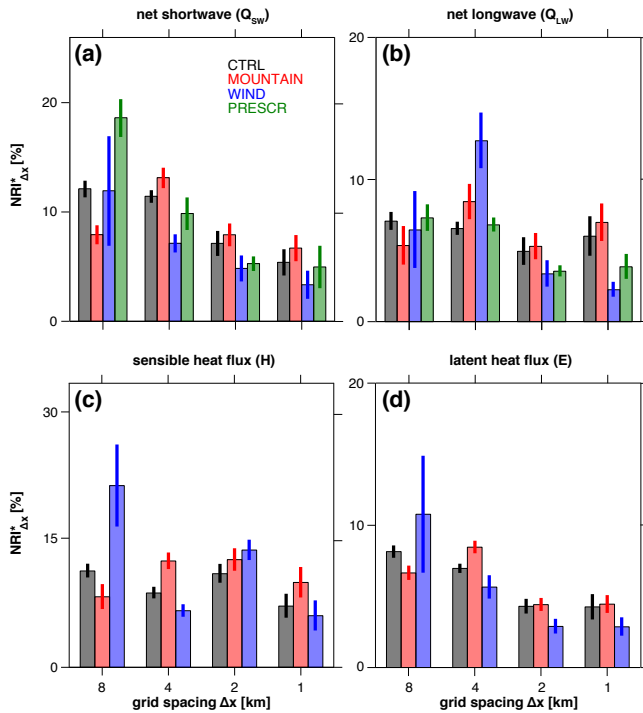
Figure 2.9: As Fig. 2.6b but computed for the different elements of the surface radiation balance (see Eq. 2.13).
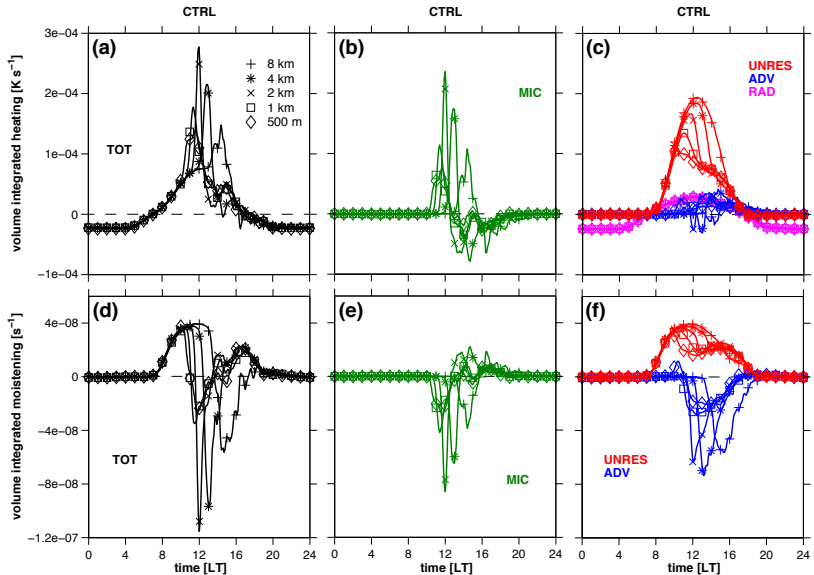
Figure 2.10: Mean diurnal cycles of volume-averaged density-weighted (a-c) heat and (d-f) water vapor tendencies in CTRL. TOT (black lines) is the net tendency, ADV (blue lines) the total (resolved) advection, UNRES (red lines) is the subgrid-scale (c) sensible and (f) latent heat flux convergence, MIC (green lines) the contribution from the microphysics and RAD (magenta lines) the radiative flux convergence. The magnitude of UNRES in (c) has been multiplied by 4 to better illustrate the sensitivity to Δx. The markers distinguish between the different horizontal resolutions. The integration volume covers the entire horizontal domain and has a top at 4000 m height.

due to radiative flux convergence and the unresolved fluxes, which mainly consist of surface latent heat flux. Note that the magnitude of these latter in Fig. 2.10c has been multiplied by 4 to better illustrate their sensitivity to Δx. Once convection sets in, additional warming is given by condensation of water vapor into cloud droplets. After 12 LT the net warming is reduced primarily because of evaporative cooling due to precipitation.

Figures 2.10d-f show a net moistening of the control volume due to the subgrid-scale surface latent heat flux convergence in the morning hours. Once clouds form, the positive contribution from the surface latent heat flux decreases and a net drying of the control volume is observed due to vertical water vapor advection associated with the mass exchange from the lower toward the higher atmosphere, and to condensation of water vapor into cloud droplets. After 14 LT a net moistening of the control volume is again observed primarily due to evaporation of rain drops. Note that, although the general time evolution is similar across the different resolutions, a clear phase shift and large differences in magnitude are visible in the mean diurnal cycles of all the tendencies shown.

Figure 2.11 show the $NRI_{\Delta x}^*$ computed for the volume-integrated, density-weighted total and microphysical heat and water vapor tendencies within the control volume in the different experiments. The tendencies due to the (resolved) advection and to the unresolved fluxes are not included in the analysis, since by definition they are both sensitive to changes in the horizontal grid spacing. The radiative flux convergence is not shown since it is relatively insensitive to the horizontal resolution (cf. Fig. 2.10c). Therefore the convergence behavior of the total net heating and moistening of the control volume is solely determined by the convergence behavior of the tendencies due to the microphysics. A convergent behavior is generally obtained starting at $\Delta x = 4\,\mathrm{km}$ for all the experiments. The values of the $NRI_{\Delta x}^*$ in MOUNTAIN and WIND are notably smaller than the ones in CTRL, particularly for the finest grid spacings, whereas the ensemble spread is comparable. The pronounced orographic forcing and the higher degree of organization in the presence of environmental wind shear reduce the differences in the simulated net exchange of heat and water vapor between the lower and upper troposphere. The convergence behavior of PRESCR is relatively similar to the one of CTRL with the exception of the 8-km runs which, consistently with what observed Fig. 2.6b for the surface rain rate and in Fig. 2.9a for the surface net shortwave radiation, exhibit larger differences with their next higher-resolution counterparts compared to all the other experiments. This suggests that important interactions between atmospheric and land-surface processes may happen at those scales. Whereas a convergent behavior is observed beginning at $\Delta x = 4\,\mathrm{km}$ also for PRESCR_NORAD, the resolution sensitivity is much higher compared to all the other experiment. This was partially observed, although to a much lesser extent, also in Fig. 2.6b for the surface rain rate. The more explosive convective activity observed in PRESCR_NORAD compared to
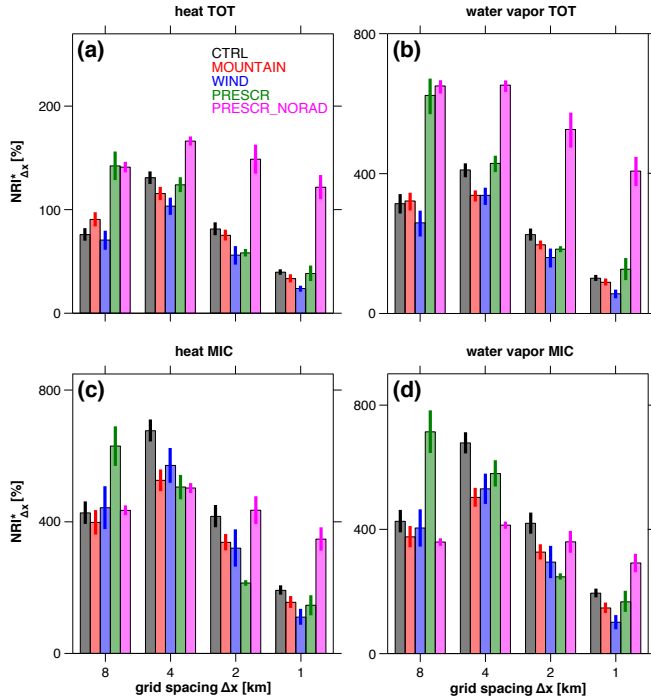
Figure 2.11: As Fig. 2.6b but computed for the volume-averaged density-weighted (a) and (b) total and (c) and (d) microphysical (a) and (c) heat and (b) and (d) water vapor tendencies.
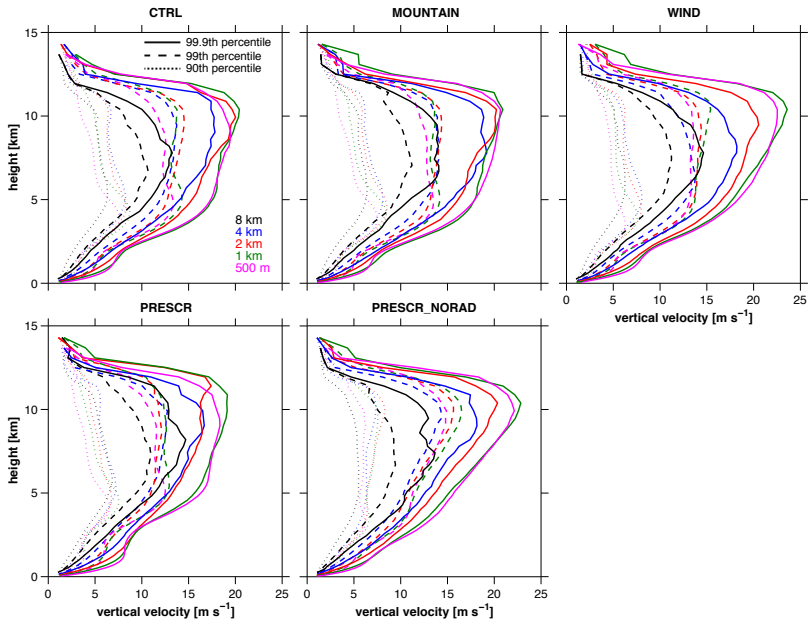
Figure 2.12: Vertical profiles of 90th (dotted lines), 99th (dashed lines) and 99.9th (solid lines) percentile of updraft velocity [m s⁻¹] between 12 LT and 18 LT. Updrafts are defined as grid points where vertical wind speed exceeds 1 m s⁻¹.

all the other experiments (cf. Fig. 2.5e and 2.5f) may explain the very large resolution sensitivities, since small differences in the initiation timing of convection will result in very large values of the $NRI^*_{\Delta x}$ when the magnitudes are stronger.

2.4.3 Structural convergence

In this section, statistical properties related to convection are examined and structural convergence is discussed for pooled grid-point values.

Figure 2.12 shows the averaged vertical profiles of the 90th, 99th and 99.9th percentile of updraft velocity between 12 LT and 18 LT. This analysis is inspired by Dauhut et al. [2015], and consistently with their study updrafts are defined as grid points where vertical wind speed exceeds 1 m s⁻¹. The profiles at $\Delta x = 8$ km and, to a lesser extent, at $\Delta x = 4$ km show that these coarse grid spacings do not allow the strongest updrafts to be reproduced. Convective overturning is forced to occur over larger scales as the model grid resolution is decreased within the gray zone, which leads to fewer, wider and weaker updrafts at coarse resolutions [e.g. Bryan and Morrison, 2012]. The vertical profiles between 1000 and 2000 m height suggest that convec-

tive motions within the boundary layer are poorly resolved at $\Delta x = 2\,\mathrm{km}$ and coarser grid spacings. Although for the 99.9th percentile the differences between $1\,\mathrm{km}$ and $500\,\mathrm{m}$ horizontal grid spacing are generally smaller than between $2\,\mathrm{km}$ and $1\,\mathrm{km}$, the same does not hold for the smaller percentiles. Dauhut et al. [2015] indeed showed that for such statistics convergence is obtained at scales much smaller than a few kilometers.

Although the overall shape of the vertical profiles in Fig. 2.12 is similar for the different experiments, a few small differences are noticeable. In MOUNTAIN the profiles for the 99.9th percentile are closer together compared to the other experiments, possibly because of the strong orographic forcing controlling the strength of the strongest updrafts. In WIND and in PRESCR_NORAD the 99.9th percentile values in the upper troposphere for the higher-resolution runs are higher compared to the other experiments. Whereas in the former experiment this can be explained by the reduced entrainment and consequently increased updraft strength within the observed larger cloud clusters, in the latter it may be due to the prescribed homogeneous radiative cooling and associated destabilization of the atmospheric column. In PRESCR_NORAD convective motions within the boundary layer are weaker compared to all the other experiments, which also suggest a more explosive convective activity (cf. Figs. 2.5e and 2.5f).

Figure 2.13 illustrates the probability density functions (PDFs) of convective mass flux at $3000\,\mathrm{m}$ height. This is the height at which it is on average the strongest for all the experiments (cf. Fig. 2.5). Note that differently from Eq. 2.12 no condition is applied here to w, and the contribution of non-cloudy grid points is accounted for. Although the shape of the PDFs at low and moderate updraft values is relatively consistent across the analyzed range of horizontal grid spacing, the range of values is wider for higher resolutions. The downward convective mass flux is less intense at coarser grid spacings, suggesting that the downdrafts need finer grids to be well resolved. The coarser grid spacings do not allow the strongest updrafts and downdrafts to be reproduced, consistently with what shown in Fig. 2.12. In general, no significant differences are identifiable between the different experiments, suggesting that the shape of the PDFs is largely controlled by the changes in horizontal grid spacing rather than by the physics of the specific case study analyzed. Nevertheless, a slightly stronger contribution stemming from moderate updrafts is observed at $\Delta x = 8\,\mathrm{km}$ in CTRL and in PRESCR_NORAD. Furthermore, the simulated updraft branch of the PDF in PRESCR is more similar across resolutions, and the largest values are smaller compared to all the other experiments. This suggests that the prescribed fluxes somehow control the strongest updrafts and ultimately have an impact on the model resolution sensitivity. A similar speculation could be made based on the vertical profiles shown in Fig. 2.12.

Although the total cloud cover does not systematically change with resolution (not shown), the simulated cloud field looks substantially different across the
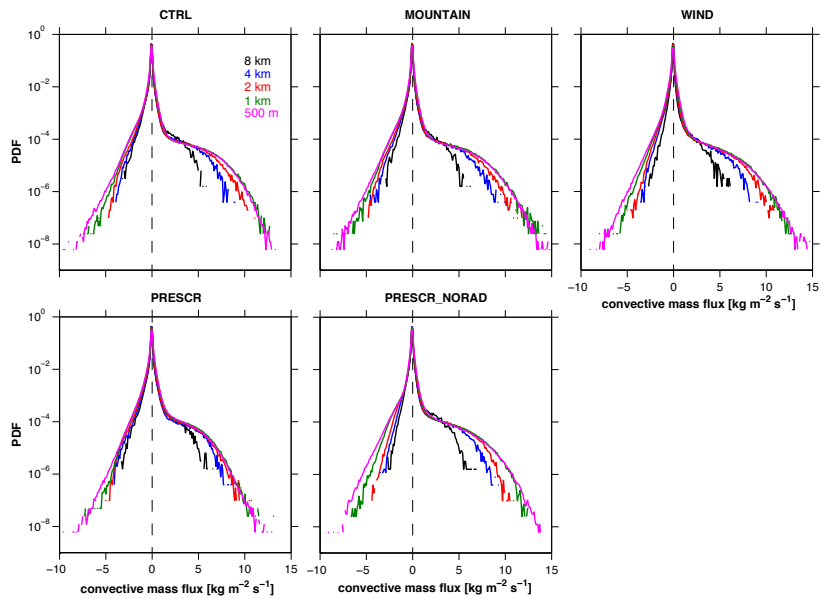
Figure 2.13: Probability density functions (PDFs) of convective mass flux at 3000 m height. The bin width is $0.1\,\mathrm{kg\,m^{-2}\,s^{-1}}$ and the data consist of the pooled grid point values taken over the entire duration of the simulations.

Figure 2.14: Display of liquid water path (LWP [kg m^{-2}]) simulated at different horizontal grid spacings in CTRL in a 120x120 km^2 subdomain located at the bottom left corner of the model domain. The display threshold is 0.01 kg m^{-2}. The horizontal grid spacing is indicated at the upper left corner of each panel.

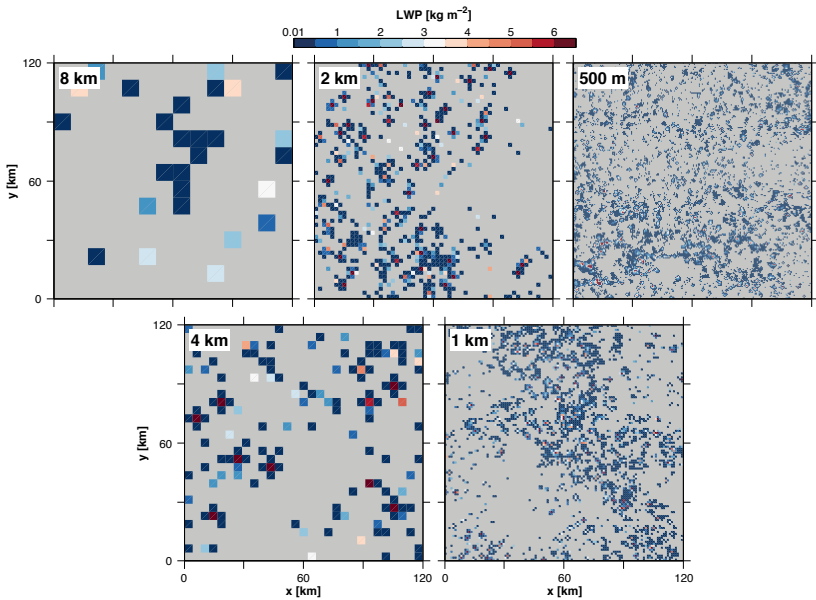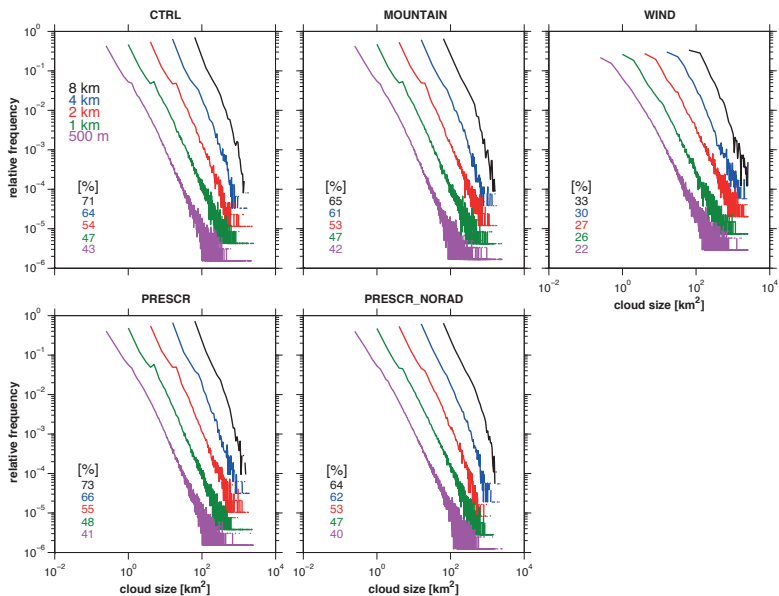**Figure 2.15:** As Fig. 2.13 but for the cloud horizontal area $[\text{m}^2]$ (cloud-size distribution). The bin width is $\Delta x^2\,\text{m}^2$ for each displayed horizontal grid spacing. The numbers at the bottom left of each panel indicate the percentage of grid-scale clouds (i.e. clouds that are only one grid box in size). The PDF has been computed based on the LWP. The cloud horizontal area is defined as the connected area of cloudy points. A cloudy point is identified by $LWP > 0.01\,\text{kg}\,\text{m}^{-2}$. Cloudy points are connected once they share a common edge.

analyzed range of horizontal grid spacings. Figure 2.14 shows snapshots of liquid water path (LWP) simulated at different Δx in CTRL at the initiation time of precipitation for a subsection of the model domain. The cloud field is dominated by very large-scale structures at coarse grid spacings, whereas smaller and more numerous cloud features are simulated with smaller grid spacings. Also the spatial distribution of clouds is not consistent across the analyzed range of horizontal resolutions.

Figure 2.15 shows the cloud-size distributions for the different experiments. The numbers at the bottom left corner of each panel in Fig. 2.15 indicate the percentage of grid-scale clouds (i.e. clouds that cover only one grid box in size). For all experiments most of the simulated clouds are grid-scale, but their relative frequency systematically decreases with increasing resolution. For almost all the experiments there are substantially less grid-scale clouds at $\Delta x = 2\,\text{km}$ and finer grid spacings, and the PDFs are flatter compared to coarser resolutions. In WIND the fraction of grid-scale clouds is about 50% of the one in CTRL, and more large-scale clouds are generated. This is

consistent with Section 2.4.2.

2.5   Summary and discussion

In this study, idealized simulations of deep moist convection were performed to assess the convergence behavior of a convection-resolving model (CRM) at horizontal grid spacings (Δx) of 8, 4, 2, 1 km and 500 m. A convergent behavior is seen as systematic decrease in resolution sensitivity with smaller grid spacing. Two types of convergence estimates were investigated: bulk convergence addressing domain-averaged and integrated variables related to the water and energy budgets, and structural convergence addressing the statistics and scales of individual clouds and updrafts. The simulations were based upon the setup introduced by Schlemmer et al. [2011], which is representative of summertime European climatological conditions. Different experiments were carried out to identify those physical processes and parameterizations which foster convergence or yield a lower resolution sensitivity.

The bulk properties under investigation were the domain-averaged surface rain rate and surface radiation budget, and the integrated atmospheric heat and water vapor tendencies. For the model and experiments considered, results revealed that bulk convergence generally begins at $\Delta x = 4$ km. The only exceptions were the domain-averaged outgoing longwave radiation and sensible heat flux, for which the resolution sensitivity did not systematically reduce at finer grid spacings, suggesting that these processes depend on small structures that are not well resolved at the kilometer-scale.

The presence of orography generally reduced the sensitivity to the horizontal grid spacing compared to simulations over flat terrain. The orographic forcing yields energetic structures at scales much larger than Δx, thereby improving the model performance in simulating the surface forcing and the triggering of deep moist convection even at coarse resolutions. Also the presence of environmental wind shear was found to sometimes reduce the resolution sensitivity. The higher degree of convective organization in the presence of environmental wind shear leads to clustering of clouds and updrafts into larger-scale structures and to the removal of some energy at the small scales, rendering it less difficult to be captured even at coarse resolutions. However, a larger ensemble spread was generally observed compared to all the other experiments.

Bulk convergence was observed also in simulations in which the land-surface and radiation schemes were switched off. However, the sensitivity to the horizontal grid spacing did not reduce or sometimes even increased. In particular, we systematically observed more pronounced differences between the 8-km and 4-km simulations when switching off the land-surface scheme compared to all the other experiments, suggesting that important interactions between atmospheric and land-surface processes may happen at those scales. Switching off the surface radiation scheme generally led to strong resolution

sensitivities also at fine grid spacings, primarily due to a more explosive convective activity as a result of the prescribed homogeneous radiative cooling and associated destabilization of the atmospheric column, and consequently larger differences in the mean diurnal cycles of the analyzed variables.

Structural convergence was addressed based on the analysis of percentiles of updraft velocities and probability density functions of convective mass fluxes and cloud horizontal area. Results revealed that structural convergence is not yet fully achieved at scales of $\mathcal{O}(1\,\mathrm{km})$. Shallow convection within the planetary boundary layer started to be partially resolved only at $\Delta x = 4\,\mathrm{km}$. The maximum updraft velocity generally increased with finer grid spacings. The cloud field looked substantially different across the analyzed range of horizontal grid spacings, with smaller and more numerous clouds simulated at higher resolution. Most of the simulated clouds were only one grid box in size. This is in line with Bryan et al. [2003] and Hanley et al. [2015], who did not find convergence of cloud system properties at convection-resolving grid spacings. Despite this, for some statistics related to updraft velocity and convective mass flux the resolution sensitivity decreased at $\Delta x = 4\,\mathrm{km}$ and lower. Similar results were obtained by e.g. Verrelle et al. [2015] in their idealized simulations of mesoscale convective systems.

To summarize, although a horizontal grid spacing of $\Delta x = 500\,\mathrm{m}$ is too coarse to fully resolve the complex boundary layer dynamics and small-scale processes such as entrainment and detrainment, bulk convergence of a number of variables related to deep moist convection could be obtained at convection-resolving horizontal grid spacings of $\mathcal{O}(1\,\mathrm{km})$ and for a wide range of different experiments. This result is particularly encouraging as the resolution required to simulate the domain-averaged and integrated quantities appears much coarser that the one required to successfully capture the structural details of convective systems. Our results contribute toward understanding the feasability of convection-resolving simulations and support the physical validity of the approach. Compared to the previous results obtained by Langhans et al. [2012c], bulk convergence was demonstrated on smaller domains, shorter time scales and for a wider range of environmental cases. Considering the size of the analyzed domain $(200 \times 200\,\mathrm{km}^2)$, which roughly corresponds to a GCM grid box, our findings are of particular interest for superparameterizations, considering the relatively low sensitivity found for the bulk net tendencies to the horizontal grid spacings at $\Delta x = 2\,\mathrm{km}$ and lower.

With regard to structural convergence, this paper extends the findings of previous idealized studies by investigating a larger number of convective cells and timescales longer than a few hours only (at which the model can still be quite sensitive to the initialization).

One key limitation of the study relates to the consideration of idealized simulations only. Additional studies are also needed to address the convergence behavior of convection-resolving simulations for synoptic situations different than summertime deep convection, such as cases with frontal systems or,

more in general, without a pronounced diurnal cycle of solar radiation.

3

Bulk and structural convergence at convection-resolving scales in real-case simulations of summertime moist convection over land

Davide Panosetti[1], Linda Schlemmer[1], and Christoph Schär[1]

Abstract Convection-resolving models (CRMs) are established as a solid framework to simulate moist convection in both numerical weather prediction and regional-scale climate projections. However, capturing the different scales of the governing processes is challenging. Previous studies have shown that the size and properties of individual clouds and updrafts do not converge until horizontal grid spacings (Δx) of $\mathcal{O}(100\,\mathrm{m})$. We refer to this as *structural convergence*. On the other hand, a few recent studies have demonstrated that domain-averaged and integrated tendencies related to a large ensemble of convective cells converge at the kilometer scale. We refer to this as *bulk convergence*.
This study investigates both the bulk convergence of the mean diurnal cy-

---

[1]Institute for Atmospheric and Climate Science, ETH Zurich, Universitätstrasse 16, 8092 Zurich, Switzerland

cle and spatial distribution of precipitation, clouds and convective transport, and structural convergence of cloud-scale statistics in real-case convection-resolving simulations. Two 9-day episodes of quasiperiodic diurnal moist convection are simulated at $\Delta x = 8.8$, 4.4, 2.2, 1.1 km and 550 m over the Alps and over Central Germany to compare the results in the presence and in the absence of a mesoscale orographic forcing.

Results reveal that bulk convergence is systematically achieved in both episodes for the spatial distribution of the analyzed quantities. For their mean diurnal cycle, bulk convergence is generally observed in simulations over the Alps, but not over Central Germany, indicating that the presence of a mesoscale orographic forcing reduces the resolution sensitivity of the bulk flow properties. Structural convergence is confirmed to be not yet fully achieved at the kilometer scale. In particular, the size and strength of the simulated convective updrafts and the size of the smallest clouds are largely determined by Δx.

3.1 Introduction

The diversity of scales involved in the initiation and development of moist convection requires a sophisticated modeling approach. Large uncertainties in state-of-the-art global (GCM) and regional-scale (RCM) climate models are related to the representation of clouds and convection. Dai and Trenberth [2004] observed a too early onset of summertime convection in a GCM in comparison to observations. Brockhaus et al. [2008] reported a similar issue in a RCM with parameterized convection. In the context of numerical weather prediction (NWP) processes such as convective showers are poorly represented in models with horizontal grid spacings (Δx) larger than 10 km at which not even large deep convective cells are explicitly resolved [e.g. Clark et al., 2016].

The increasing computational resources have allowed simulations of moist convection at the so-called "convection-resolving" Δx of $\mathcal{O}(1\,\mathrm{km})$. At these resolutions the fundamental non-hydrostatic processes of deep convective thunderstorms are explicitly resolved [Klemp and Wilhelmson, 1978; Weisman et al., 1997] and deep convection parameterization can be switched off. Today such convection-resolving models (CRMs: often referred to as convection-permitting or cloud-resolving models in the literature, see e.g. Prein et al., 2015) are largely employed for research purposes and by national weather services for limited-area NWP [e.g. Saito et al., 2007; Weusthoff et al., 2010; Tang et al., 2013; Brousseau et al., 2016]. The general experience is that CRMs perform better than convection-parameterizing models in both NWP [e.g. Richard et al., 2007; Lean et al., 2008; Weisman et al., 2008] and regional-scale climate simulations [e.g. Kendon et al., 2012; Ban et al., 2014]. Moreover, recent studies have established CRMs as a solid framework for decade-long continental-scale climate simulations [e.g. Ban et al., 2015; Liu

et al., 2016; Leutwyler et al., 2016, 2017; Prein et al., 2017].

Owing to the increased resolution CRMs can also benefit from a better representation of the underlying orography, coastal lines and land surface heterogeneity [e.g. Leroyer et al., 2014], which may trigger convective clouds. Over mountainous regions such as the Alps, thermally-driven wind systems can locally trigger convective cells even in otherwise fair-weather conditions [e.g. Banta, 1990; Houze, 1993; Kirshbaum, 2011; Kirshbaum et al., 2018]. Frei and Schär [1998] have shown a summertime precipitation enhancement over the Alpine region compared to over the rest of Europe. Panziera et al. [2018] observed peaks in extreme rainfall over the Jura mountains and the Northern Alps in their high-resolution radar-based precipitation climatology over Switzerland. Features such as cloud self-organization, gust fronts from earlier clouds and precipitation-driven cold pools are also better represented in CRMs compared to coarser-resolution models and contribute to a more realistic simulation of the diurnal cycle of convection [e.g. Lean et al., 2008; Hohenegger et al., 2015].

However, there is also evidence [e.g. Bryan and Rotunno, 2005; Petch, 2006; Panosetti et al., 2016] that convection is under-resolved at Δx of $\mathcal{O}(1\,\mathrm{km})$. In reality clouds comprise a myriad of interacting processes which have important motions at scales much smaller than the ones represented on a CRM grid. The continuous energy spectrum of convection does not break at the kilometer scale and horizontal grid spacings of $\mathcal{O}(100\,\mathrm{m})$ or even lower may be needed to properly resolve convective clouds [Bryan et al., 2003]. Moreover, the effects of turbulence parameterizations are poorly understood [e.g. Wyngaard, 2004; Skamarock, 2004], although they may be important in controlling the scales of motion. This "no-men's land" in which the partition between grid-scale and subgrid-scale processes is unclear is often referred to as the *grey zone* of convection.

The truncation of the energy cascade at the scale of the model grid leads to relatively large sensitivities of the smallest simulated convective features [e.g. Langhans et al., 2012c; Panosetti et al., 2018], turbulence and entrainment [e.g. Bryan et al., 2003; Wyngaard, 2004; Bryan and Morrison, 2012; Ricard et al., 2013], microphysics [e.g. van Ypersele de Strihou and Marbaix, 2013; White et al., 2017] and convective updrafts [e.g. Lebo and Morrison, 2015; Jeevanjee, 2017] to the employed Δx. These studies suggest that cloud-scale properties do not converge until Δx of a few hundred meters or even smaller. We refer to this as *structural convergence*, since the focus is on the size and properties of individual clouds and convective updrafts.

On the other hand, recent studies have shown that domain-averaged and integrated properties related to a large ensemble of convective cells often converge at the kilometer scale. These include idealized simulations of deep convection [Verrelle et al., 2015; Panosetti et al., 2018], and real-case simulations of thermally-driven orographic convection over the Alps [Langhans et al., 2012c] and cold fronts over the UK [Harvey et al., 2017]. These find-

ings lend support to the use of CRMs, since they demonstrate that large-scale flow properties are relatively unaffected by further refinement of the mesh grid beyond the kilometer scale. We refer to this as *bulk convergence*, since the focus is on the bulk flow properties.

However, these studies are based primarily on highly idealized setups or considered only single episodes in real-case simulations. This raises concerns as whether bulk convergence is indeed an intrinsic property of convection-resolving simulations, or it can be achieved only in idealized setups, in which the influence of external parameters such as small-scale orography or land use is generally limited, or in the presence of a pronounced mesoscale forcing such as Alpine-scale thermally-driven wind systems [Langhans et al., 2012c]. Furthermore, the low resolution sensitivity found for bulk flow properties in real-case simulation has not been compared with any measure quantifying atmospheric predictability, such as the average ensemble spread. In Panosetti et al. [2018] the resolution sensitivity was observed to be much larger than the ensemble spread for most of the analyzed quantities. However, in their idealized simulations the ensemble was constructed by using different initial random temperature perturbations at the lowest model level to break the symmetry of an otherwise flat homogeneous model domain. This may result in a relatively small ensemble spread compared to real-case setups, in which ensembles are generated by perturbing the initial conditions of an already strongly heterogeneous model domain. Finally, in all these previous studies bulk convergence was addressed only for the mean diurnal cycle of the analyzed variables, but never for their spatial distribution, which is equally important for both NWP and climate projections.

This study investigates both the bulk convergence of the mean diurnal cycle and spatial distribution of precipitation, clouds and convective transport of mass, heat and water vapor, and structural convergence of scales and properties of individual clouds and convective updrafts in real-case convection-resolving simulations. A revised metric to address bulk convergence compared to previous studies [e.g. Langhans et al., 2012c; Panosetti et al., 2018] is presented that allows for a systematic comparison of the resolution sensitivity with the average ensemble spread, and thus a more thorough assessment of bulk convergence. To these aims, the Consortium for Small-Scale Modeling (COSMO) model is run to study the diurnal cycle of convection and precipitation in real-case setups over land. Two 9-day episodes are considered, one of thermally-driven orographic convection over the Alps [e.g. Langhans et al., 2012c] and one of diurnal airmass convection over Central Germany [e.g. Keller et al., 2016], to compare the results in the presence and in the absence of a mesoscale orographic forcing.

The numerical model and the experimental design are presented in Section 3.2. In Section 3.3, the methods used to compute the heat and water vapor budgets and to address bulk and structural convergence are described. In Section 3.4 some general characteristics of the simulations are presented and

bulk and structural convergence are investigated for the mean diurnal cycle, spatial distribution and statistical distributions of precipitation, clouds, convective mass fluxes and heat and water vapor tendencies. The summary and conclusions are given in Section 3.5.

3.2 Model description

3.2.1 Model

The simulations are performed with version 5.0 of the Consortium for Small-Scale Modeling (COSMO) model [Baldauf et al., 2011]. The COSMO model is a non-hydrostatic limited-area model designed for both NWP and climate modeling on a broad range of spatial scales. It employs a split-explicit method to integrate the equations forward in time with a third-order Runge-Kutta discretization [Wicker and Skamarock, 2002] for the slow modes. A fifth-order upwind scheme is used for horizontal advection temperature, pressure, and horizontal and vertical winds, and a second-order scheme [Bott, 1989] is employed for horizontal advection of moist quantities.

The physical parameterizations used in this study include a radiative transfer scheme based on the δ-two-stream approach [Ritter and Geleyn, 1992], in which radiation interacts with both subgrid and grid-scale clouds, a single-moment bulk cloud-microphysics scheme with three ice categories (ice, snow, graupel; Reinhardt and Seifert, 2006), a 10-layer land-surface model (TERRA_ML; Heise et al., 2003), and a Louis surface transfer scheme [Louis, 1979] to calculate the transfer coefficients which yield the surface sensible and latent heat fluxes based on Monin-Obukhov Similarity Theory. No convection parameterization is employed. A 1.5-order scheme based on a prognostic equation for the turbulent kinetic energy (TKE) [Raschendorfer, 2001] with a level 2.5 closure [Mellor and Yamada, 1974, 1982] is used to compute the vertical eddy viscosities for heat K_h^V and momentum K_m^V. $K_{h,m}^V$ are determined using the Prandtl-Kolomogorov specification as:

$$K_{h,m}^V = \phi_{h,m} l_v \sqrt{2e} \tag{3.1}$$

The characteristic length scale l_v for vertical mixing is calculated according to Blackadar [1962]:

$$l_v = \frac{kz}{1 + (kz)/l_\infty} \tag{3.2}$$

where k is the von-Karman constant, z is the altitude, and l_∞ is the asymptotic Blackadar length scale which is set to $100\,\mathrm{m}$ in the current study. $\phi_{h,m}$ are stability-dependent coefficients, and $\overline{e} = (\overline{u_i' u_i'})/2$, with $i = 1, 2, 3$, is the subgrid-scale TKE per unit mass. The overbar denotes a time mean. The prime indicates a subgrid-scale variable.

The eddy viscosities for second-order horizontal diffusion $K_{h,m}^H$ are computed
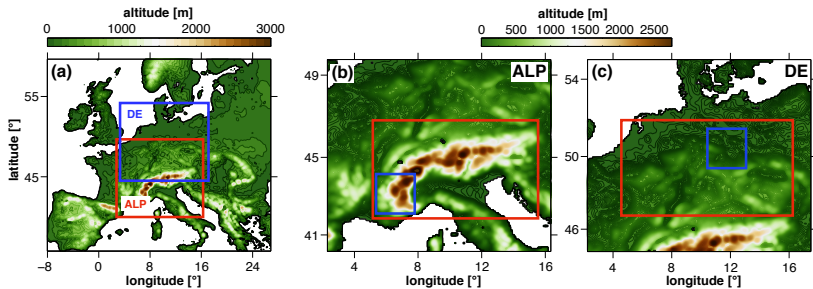
Figure 3.1: (a) Integration domain and topography [m] of the 12-km driving model. The integration domains of ALP and DE are illustrated by the blue and red boxes respectively. (b) and (c) Same as (a) but for (b) ALP and (c) DE at $\Delta x = 2.2$ km. The analysis domains for each set of simulations are illustrated by the red boxes. The blue boxes in (b) and (c) illustrate the regions for which Fig. 3.3 is computed.

based on the two-dimensional (2D) grid-scale rate of strain:

$$K_{h,m}^{H} = [c_s \sqrt{\Delta x \Delta y}]^2 \sqrt{[(D_{11} - D_{22})^2 + 4D_{12}^2]} \qquad (3.3)$$

where $D_{ij} = \frac{1}{2} \left(\frac{\partial u_i}{\partial x_j} + \frac{\partial u_j}{\partial x_i} \right)$ is the 2D grid-scale rate of strain, and $c_s = 0.25$ is the Smagorinsky constant.

3.2.2 Experimental setup

All the simulations are initialized and hourly boundary conditions are provided by a 12-km simulation covering a large domain centered over Continental Europe (Fig. 3.1a). The 12-km simulation is initialized and driven by the ERA-Interim reanalysis data at a horizontal resolution of $0.7°$ [Dee et al., 2011]. Initial soil moisture is obtained from a 10-year long climate simulation with parameterized convection over the same model domain [Ban et al., 2014].

Two sets of simulations are run at $\Delta x = 8.8, 4.4, 2.2, 1.1$ km and 550 m. The long time steps used are 80, 40, 20, 10 and 5 s, respectively. 2D and 3D fields are written to file at every hour before postprocessing. Each set of simulations is integrated over a horizontal domain of 1160×1090 km^2 centered over the Alps (ALP) and Central Germany (DE) (Figs. 3.1b and 3.1c). The model uses a pressure-based hybrid vertical coordinate with 60 stretched levels. The vertical grid spacing varies from 20 m near the surface to 800 m above 18 km. The model top is located at 21 km. At the upper domain boundary a rigid lid is employed, and a Rayleigh damping layer extends from 11.5 km to the top of the domain to minimize spurious reflections of gravity waves. 10 soil layers are used with varying thickness from 1 cm for the uppermost layer to

5.76 m for the lowermost, and the total soil depth is 15.34 m.

Land use data are retrieved from the high-resolution ($\Delta x = 300$ m) GLOB-COVER dataset. Soil data are derived from the Harmonized World Soil Database (HWSD) TERRA at a grid cell size of 1 km. Topography data sterns from the ASTER Global Digital Elevation Map (GDEM; horizontal resolution of approx. 30 m at the Equator). The resolution of the external parameters is kept constant across resolutions to avoid more detailed structures on finer grids. This is done to isolate the effect of the model grid spacing from the effects due to the modified external forcing. Details on the interpolation used to obtain nearly identical representation of the surface parameters at all grid spacings in both physical and spectral space are given in the appendix. The episodes considered in this study cover two 9-day periods of quasiperiodic diurnal moist convection with very little large-scale forcing, 11-20 July 2006 for ALP and 04-13 June 2007 for DE. In summertime over Europe, convection often occurs in response to the diurnal cycle of incoming solar radiation. The simulations start at 1200 h the day before (10 July 2006 for ALP and 03 June 2007 for DE) to allow for a short high-resolution spin up. The analysis is performed over two analysis domains of equal area illustrated by the red boxes in Figs. 3.1b and 3.1c.

For each set of simulations an ensemble is run at $\Delta x = 2.2$ km. The ensemble consists of 14 members constructed using different initial conditions obtained starting the simulation earlier or later than the reference 2.2-km run (on a -7 to +7 hour interval). The choice of this particular resolution is limited by computational constraints, and the resulting ensemble spread must be taken as representative of all the other resolutions.

3.3 Methods

3.3.1 Heat and water vapor budgets

To study the convergence of bulk flow properties, the heat and water vapor budgets of a large control volume covering the analysis domain in the horizontal and with a rigid top at 4000 m altitude are investigated. The volume-averaged tendencies are thus representative of deep convective fluxes towards the upper atmosphere (plus a small contribution from lateral fluxes in and out of the control volume).

The processes contributing to the instantaneous local heating and cooling of the atmosphere are given by:

$$\frac{\partial \theta}{\partial t} = -\mathbf{v} \cdot \nabla \theta - \frac{1}{\rho c_p}(\nabla \cdot \mathbf{H}) - \frac{1}{\rho c_p}(\nabla \cdot \mathbf{R}) + L_m \qquad (3.4)$$

where θ is the potential temperature, $\mathbf{v}$ the wind speed vector, ρ is the air density, c_p is the heat capacity at constant pressure, $\mathbf{H} = \rho c_p \overline{\mathbf{v}'\theta'}$ is the subgrid-scale sensible heat flux, $\mathbf{R}$ is the radiative energy flux, and L_m is the latent heating rate. All the terms in Eq. 3.4 are extracted using the budget

tool implemented in the COSMO model [Langhans et al., 2012b].
The net effect of each process on the control volume V of total mass $M = \int_V \rho dV$ is computed by integrating Eq. 3.4 over V. The volume-averaged density-weighted heat budget equation is:

$$\underbrace{\frac{1}{M} \int_V \rho \frac{\partial \theta}{\partial t} dV}_{\text{TOT}} = \underbrace{-\frac{1}{M} \int_V \rho \mathbf{v} \cdot \nabla \theta \, dV}_{\text{ADV}} + \underbrace{\frac{1}{M} \int_V -\frac{1}{c_p} (\nabla \cdot \mathbf{H}) dV}_{\text{UNRES}}$$

$$+ \underbrace{\frac{1}{M} \int_V -\frac{1}{c_p} (\nabla \cdot \mathbf{R}) dV}_{\text{RAD}} + \underbrace{\frac{1}{M} \int_V \rho L_m \, dV}_{\text{MIC}} \quad (3.5)$$

where TOT is the net heat tendency, ADV is the grid-scale advection, UNRES is the subgrid-scale sensible heat flux convergence, RAD is the radiative flux convergence, and MIC is the contribution from microphysical processes (primarily latent heat exchange due to condensation of water vapor and evaporation of rain).

Similar to the heat budget equation, the water vapor budget equation can be written in its volume-averaged density-weighted form as:

$$\underbrace{\frac{1}{M} \int_V \rho \frac{\partial q_v}{\partial t} dV}_{\text{TOT}} = \underbrace{-\frac{1}{M} \int_V \rho \mathbf{v} \cdot \nabla q_v \, dV}_{\text{ADV}} + \underbrace{\frac{1}{M} \int_V -\frac{1}{l_v} (\nabla \cdot \mathbf{L}) dV}_{\text{UNRES}}$$

$$+ \underbrace{\frac{1}{M} \int_V \rho S_m \, dV}_{\text{MIC}} \quad (3.6)$$

where TOT is the net water vapor tendency, ADV is the grid-scale water vapor advection, UNRES is the subgrid-scale latent heat flux convergence, and MIC is the microphysics contribution. q_v is the specific water vapor, l_v is the latent heat of vaporization, $\mathbf{L} = \rho l_v \overline{\mathbf{v}' q_v'}$ is the subgrid-scale latent heat flux, and S_m are microphysical source/sink rates.

3.3.2 Bulk convergence

To study the convergence of bulk flow properties a simple metric is considered that illustrates the resolution sensitivity of the mean diurnal cycle or spatial distribution of a quantity. The root-mean-squared difference between the mean diurnal cycle ($RMSD^t_{\Delta x}$) or spatial distribution ($RMSD^s_{\Delta x}$) of a quantity ψ simulated at horizontal grid spacing Δx and $\Delta x/2$ is considered. In the former case, the $RMSD^t_{\Delta x}$ is computed as:

$$RMSD^t_{\Delta x} = \sqrt{\frac{1}{N} \sum_{n=1}^{N} [\psi_{\Delta x}(n) - \psi_{\Delta x/2}(n)]^2} \quad (3.7)$$

where n is a specific time of the mean diurnal cycle, $N = 24$ for hourly output data and the superscript t (time) indicates that the quantity is computed for the mean diurnal cycle of ψ. In the latter case, first the data is coarse-grained to the coarsest resolution ($\Delta x = 8.8\,\mathrm{km}$) and then the $RMSD_{\Delta x}^{s}$ is computed as:

$$RMSD_{\Delta x}^{s} = \sqrt{\frac{1}{X} \sum_{x=1}^{X} [\psi_{\Delta x}(x) - \psi_{\Delta x/2}(x)]^2} \qquad (3.8)$$

where x is a specific grid point, X is the total number of grid points of the coarse-grained field and the superscript s (space) indicates that the quantity is computed for the spatial distribution of ψ integrated in time.

To compare the resolution sensitivity with a measure to quantify atmospheric predictability, the average ensemble spread for temporal and spatial analysis $E_{2.2\,km}^{t,s}$ is computed for each 2.2-km simulation as:

$$E_{2.2\,km}^{t,s} = \sqrt{\frac{1}{N,X} \sum_{n,x=1}^{N,X} \sigma^2(n,x)} \qquad (3.9)$$

where the square root of the average ensemble variance σ^2 is considered [e.g. Fortin et al., 2014]. To compute the normalized resolution increment $NRI_{\Delta x}^{t,s}$ both Eq. 3.7 and Eq. 3.8 are normalized by Eq. 3.9:

$$NRI_{\Delta x}^{t,s} = \frac{RMSD_{\Delta x}^{t,s}}{E_{2.2\,km}^{t,s}} \qquad (3.10)$$

A value of 1 for the $NRI_{\Delta x}^{t,s}$ thus means that the $RSMD_{\Delta x}^{t,s}$ equals the average ensemble spread $E_{2.2\,km}^{t,s}$. A value larger than 1 indicates that the increment in the simulated quantity from one resolution to the next finer one is larger than the average ensemble spread. In this case, a systematic decrease in the $RSMD_{\Delta x}^{t,s}$ with increasing resolution would indicate bulk convergence, whereas the opposite would reject the hypothesis of bulk convergence. On the other hand, a value smaller than 1 indicates that the increment in the simulated quantity from one resolution to the next finer one is smaller than the average ensemble spread. This in turn indicates that it is impracticable to assess whether bulk convergence is achieved or not. Note that in the case of the mean diurnal cycle the $NRI_{\Delta x}^{t}$ is sensitive to both differences in amplitude and phase.

This revised metric allows for a more thorough assessment of bulk convergence compared to previous studies [e.g. Langhans et al., 2012c; ?] in which the employed normalization factor did not allow for a systematic comparison between the resolution sensitivity and the model ensemble spread.

3.3.3 Structural convergence

To address structural convergence the scales and properties of single convective updrafts and clouds are considered. Differently from bulk convergence, for which a large ensemble of convective clouds must be considered, any averaging or integration is done at the scale of the single convective clouds or updrafts. To this aim, spectral analysis of the vertical velocity field and cloud-scale statistics such as cloud-size distributions and probability density functions (PDFs) of mean updraft velocity inside the single convective clouds are presented in Section 3.4.3.

Individual clouds are identified by means of an algorithm based on the liquid water path (LWP) to avoid capturing large-scale anvils. A cloudy grid point is identified by $LWP > 0.01\,\mathrm{kg\,m^{-2}}$. The cloud size is defined as the connected area of cloudy points. Cloudy points are connected once they share a common edge. The average vertical velocity within each cloud is computed as a mean from cloud base to cloud top.

3.4 Results

This section is divided into three parts. First, some general characteristics of the simulations are described. Second, bulk convergence is discussed for the mean diurnal cycle and spatial distribution of precipitation, clouds and convective transport of mass, heat and water vapor. Third, structural convergence of cloud-scale statistics is addressed by means of spectral analysis of vertical wind speed and probability density functions of cloud size and updraft velocities.

3.4.1 General characteristics

Figure 3.2 shows time series and the mean diurnal cycle of domain-averaged surface precipitation obtained from the two sets of simulations. The simulations are characterised by quasiperiodic diurnal convective precipitation. Convection appears to be particularly intense during the first 4-5 days of simulation in ALP, and during the last 4 days of simulation in DE. In both episodes precipitation peaks in the late afternoon, although the maximum in DE generally occurs 1-2 hours later compared to ALP. This is due to the thermally-driven wind systems in ALP, which generate mass and moisture convergence over the Alps and favor a faster transition to deep convection. The absence of nighttime precipitation in ALP compared to DE may also be linked to thermally-driven wind systems, as downslope winds forming in the late evening dampen local convective activity and export moisture out of the Alpine region [e.g. Langhans et al., 2013; Schmidli, 2013].

The changes induced by different horizontal grid spacing in ALP are more systematic and less pronounced compared to DE. This is explained by the different nature of convection in ALP and DE. In ALP the forcing is dominated
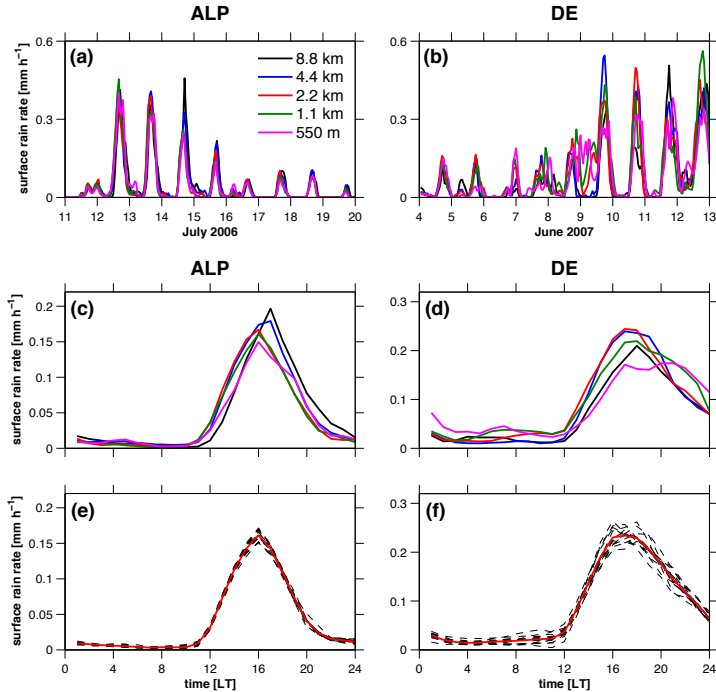
Figure 3.2: (a) and (b) Time series of surface rain rate [mm h⁻¹] in (a) ALP and (b) DE. (c) and (d) Mean diurnal cycle of surface rain rate [mm h⁻¹] in (c) ALP and (d) DE. The colors distinguish between the different horizontal grid spacings. (e) and (f) As (c) and (d) but for the $\Delta x = 2.2\,\text{km}$ ensemble. The dashed black lines illustrate the mean diurnal cycle simulated by the single ensemble members.
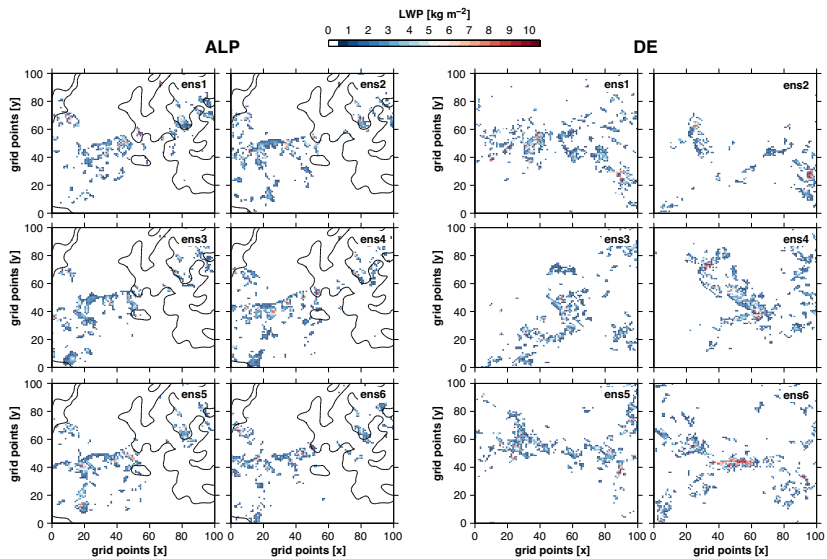
Figure 3.3: Display of liquid water path (LWP) [kg m^{-2}] in 6 of the 14 ensemble members at $\Delta x = 2.2$ km (left panels) at 1600 h 12 July in ALP and (right panels) at 1700 h 09 June in DE. The regions are illustrated by the blue boxes in Figs. 3.1b and 3.1c. The black contours indicate the areas where the terrain altitude is larger than 1000 m.

by the mesoscale thermally-driven wind systems. In DE surface heating and moistening and boundary-layer growth are the main drivers of convective activity. At $\Delta x = 8.8\,$km the onset time of precipitation is delayed compared to finer resolutions in both experiments, which is explained by the fact that it takes longer time to saturate a very large grid box. Several studies have highlighted the need for a convection parameterization at resolutions as fine as $4\,$km [e.g. Verrelle et al., 2015], as convective motions are clearly unresolved at those scales. At $\Delta x = 550\,$m precipitation is less intense in the afternoon hours and more intense in the evening hours compared to coarser resolutions. This is more evident in DE than in ALP.

The ensemble spread is much larger in DE compared to ALP, also owing to the lack of orographic forcing. To further analyze the predictability of the single convective cells in the two episodes, Fig. 3.3 compares snapshots of clouds in two small subdomains in 6 of the 14 ensemble members at 1600 h 12 July in ALP and at 1700 h 09 June in DE. These specific times are chosen to capture the more active periods of convection in the two episodes, but similar results can be obtained for different times. The spatial distribution of clouds in ALP is remarkably similar within the ensemble, whereas in DE the clouds are rather randomly distributed. This is likely due to the reduced level of mesoscale orographic forcing in DE.

The spatial distribution of the 9-day total accumulated precipitation and integrated LWP and convective mass flux (M_c) is shown in Fig. 3.4 for ALP and in Fig. 3.5 for DE. To illustrate only the upward mass transport by the convective clouds, M_c is computed at each grid point as:

$$M_c = \rho w, \quad w > 1\,m\,s^{-1}, \quad q_c > 10^{-6}\,kg\,kg^{-1} \tag{3.11}$$

where w is the vertical velocity and q_c is the specific cloud liquid water content. After the computation all data is coarse-grained to $\Delta x = 8.8\,$km to better compare the differences induced by further refining the mesh grid.

The rainfall in DE is rather homogeneously distributed, whereas in ALP it is limited to the mountains. Precipitation is enhanced, particularly over the southwestern sector of the Alps, and increasingly absent over the Po Valley. Overall it is striking to observe that the rainfall distribution is consistently captured even at very coarse resolutions in ALP. On the other hand, similar precipitation patterns in DE are observed only at $\Delta x = 2.2, 1.1\,$km and $550\,$m, with the 4.4 and 8.8-km simulations partially and completely missing the maximum in the western sector of the analysis domain. Also, the area of light precipitation is significantly smaller at coarse resolutions. On the other hand, the spatial distribution of LWP and M_c is similarly captured in both sets of simulations. Nevertheless, the structural changes at finer resolutions differ for the two variables. The largest values of LWP are generally observed at coarse resolutions, whereas the opposite holds for M_c.

To quantify the relative contribution of the different terms in the heat (Eq. 3.5) and water vapor (Eq. 3.6) budget equations to the net heating and moistening of the lower atmosphere, the mean diurnal cycle of specific heat and
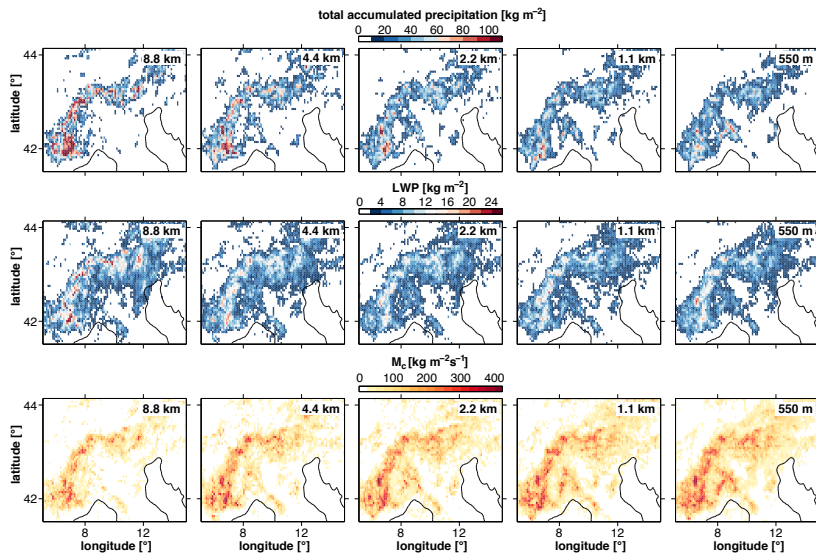
Figure 3.4: Spatial distribution of the 9-day (top panels) total accumulated precipitation [kg m^{-2}] and integrated (middle panels) liquid water path (LWP) [kg m^{-2}] and (bottom panels) convective mass flux (M_c) [kg m^{-2} s^{-1}] at different horizontal grid spacings in the analysis domain in ALP (cf. Fig. 3.1b). The data is coarse-grained to $\Delta x = 8.8$ km.
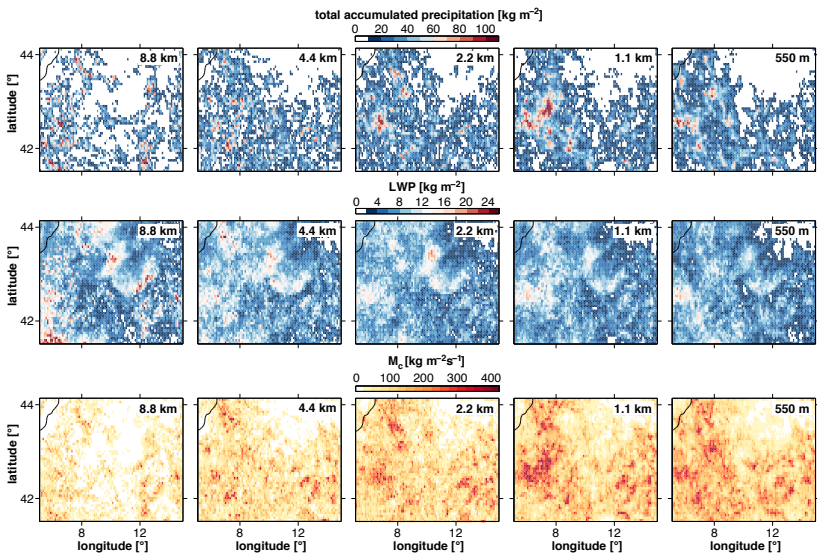
Figure 3.5: Same as Fig. 3.4 but for DE. The analysis domain is illustrated in Fig. 3.1c.

water vapor tendencies within a control volume is shown in Fig. 3.6 (see Section 3.3.1 for a detailed description of the budgets and the control volume). A net warming mostly driven by radiative flux convergence and subgrid-scale surface sensible heat flux convergence is observed between 0800 and 1700 h in both simulation sets. Once convection sets in in the afternoon, additional warming is provided by condensation of water vapor into cloud droplets, followed by cooling due to evaporation of precipitation. The net advective tendencies show a more or less pronounced late-afternoon cooling largely caused by precipitation-driven cold pools (not shown). Nighttime radiative cooling is observed during the remaining hours. The main process contributing to the net diurnal moistening of the control volume is subgrid-scale latent heat flux convergence. Once clouds form, the net moistening decreases due to vertical water vapor advection associated with the mass exchange from the lower towards the higher troposphere, and partly to condensation of water vapor into cloud droplets. Evaporation of rain drops is a minor contributor, at least in ALP, to a net moistening of the control volume. Note that in ALP the drying of the control volume due to advection is more pronounced than in DE in the early morning and late evening. This is due to downslope winds (horizontal advection) which export moisture out of the Alpine region.

In both sets of simulations the net heating tendencies show a reduced resolution sensitivity compared to the net moistening tendencies, suggesting
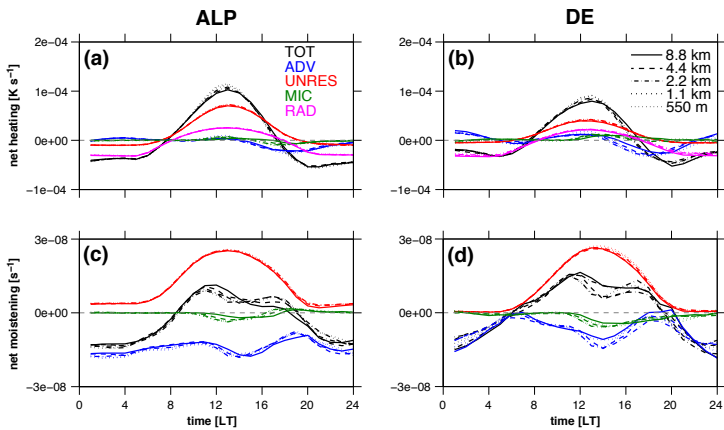
Figure 3.6: Mean diurnal cycle of volume-averaged density-weighted (a) and (b) heat and (c) and (d) water vapor tendencies in (a) and (c) ALP and (b) and (d) DE. TOT (black lines) is the net tendency, ADV (blue lines) the total (resolved) advection, UNRES (red lines) is the subgrid-scale (a,b) sensible and (c,d) latent heat flux convergence, MIC (green lines) the contribution from the microphysics and RAD (magenta lines) the radiative flux convergence. The line style distinguishes between the different horizontal resolutions. The integration volume covers the entire analysis domain in the horizontal (cf. Figs. 3.1b and 3.1c) and has a top at 4000 m altitude.

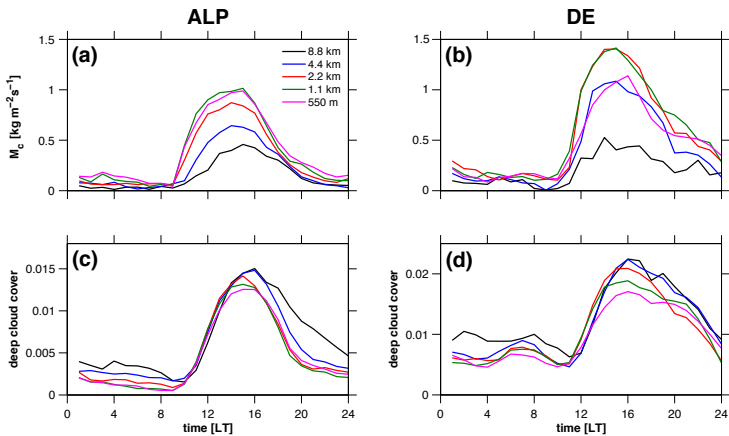**Figure 3.7:** Mean diurnal cycle of domain-averaged (a) and (b) convective mass flux at 4000 m altitude and (c) and (d) deep cloud cover in (a) and (c) ALP and (b) and (d) DE. A cloudy point is identified by $LWP > 5\,\mathrm{kg\,m^{-2}}$ to sample deep convective clouds only. The colors distinguish between the different horizontal grid spacings.

that these processes are mainly driven by large-scale forcings (a significant contribution is given by the radiative flux convergence). The exceptions are the 8.8-km simulations, which deviate substantially from the behavior of the other resolutions for both tendencies. As for the net moistening tendencies, these are more sensitive to Δx in DE compared to ALP, particularly regarding the net advection.

Figures 3.7a and 3.7b show the mean diurnal cycle of domain-averaged M_c at 4000 m altitude in ALP and DE. The resolution sensitivity is considerably larger compared to the one observed in Fig. 3.6 for net heat and water vapor tendencies and in Fig. 3.2 for the surface rain rate, suggesting a higher precipitation efficiency in wider (but weaker) updrafts. Although the phase of the diurnal cycle is relatively consistent at all resolutions, the diurnal peak is lower at larger Δx, with the exception of the 550-m simulation in DE.

The mean diurnal cycle of deep cloud cover is shown in Figs. 3.7c and 3.7d. A very large LWP threshold of $5\,\mathrm{kg\,m^{-2}}$ is used to sample deep convective clouds only. The initiation timing of deep convection is relatively consistent across resolutions in both episodes, but the maximum cloud cover is larger at coarse resolutions. Furthermore, in ALP the late-evening and nighttime deep cloud cover is comparably larger at $\Delta x = 4.4$ and $8.8\,\mathrm{km}$. At finer resolutions the sensitivities appear to be much larger in DE compared to ALP.
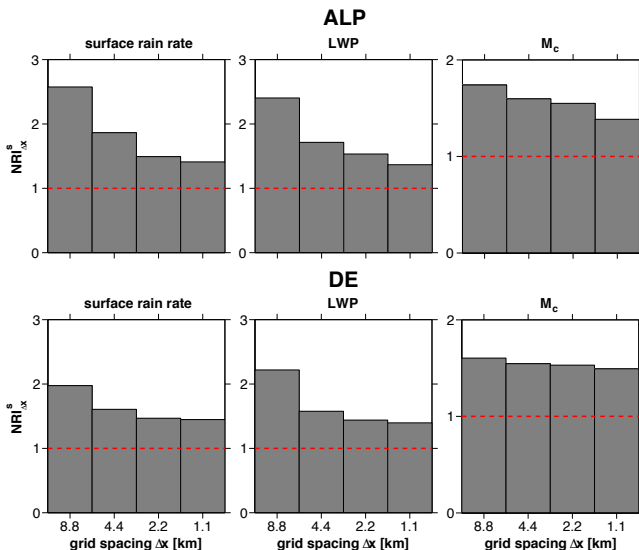
Figure 3.8: normalized resolution increment ($NRI^s_{\Delta x}$, see Eq. 3.10) versus the horizontal grid spacing (Δx) [km] computed for the spatial distribution of the 9-day total accumulated precipitation, integrated liquid water path (LWP) and integrated convective mass flux (M_c) at 4000 m altitude in (top panels) ALP and (bottom panels) DE. The red lines indicate the point at which the resolution sensitivity $RMSD^t_{\Delta x}$ equals the average ensemble spread $E^t_{2.2\,km}$.

3.4.2 Bulk convergence

In this section the bulk convergence of the spatial distribution and the mean diurnal cycle of precipitation, clouds and convective transport of mass, heat and water vapor is discussed. A detailed description and interpretation of the analysis method is given in Section 3.3.2.

Figure 3.8 illustrates the $NRI^s_{\Delta x}$ computed versus Δx for the spatial distribution of the 9-day total accumulated precipitation and integrated LWP and M_c. The red lines indicate the point at which the resolution sensitivity $RMSD^s_{\Delta x}$ equals the average ensemble spread $E^s_{2.2\,km}$. The resolution sensitivity systematically decreases for both episodes and for all the analyzed variables and is larger than the model ensemble spread, which indicates that bulk convergence is achieved.

Figure 3.9 illustrates the $NRI^t_{\Delta x}$ computed versus Δx for the mean diurnal cycle of surface rain rate, the total and microphysical heat tendencies, the total, advective and microphysical water vapor tendencies, M_c at 4000 m altitude and the deep cloud cover. In ALP bulk convergence is achieved for all variables except for the surface rain rate and for the total heat tendencies.
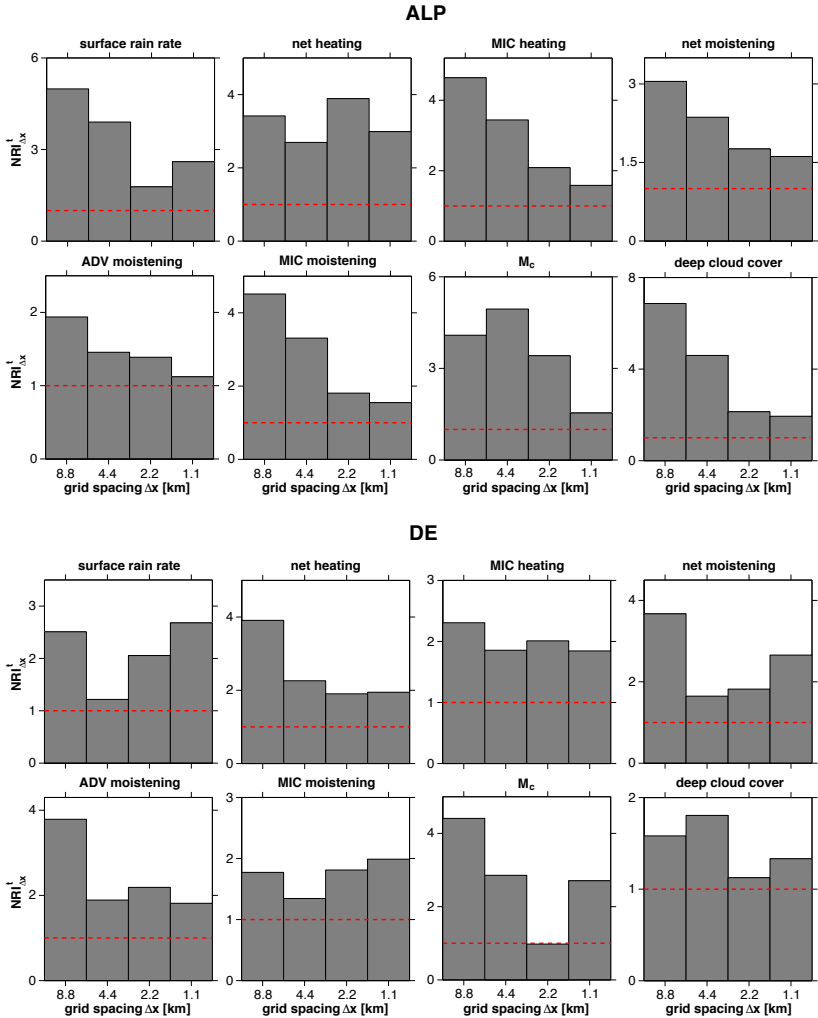
Figure 3.9: As Fig. 3.8 but computed for the mean diurnal cycle ($NRI^t_{\Delta x}$, see Eq. 3.10) of surface rain rate, the net and microphysical heat tendencies, the net, advective and microphysical water vapor tendencies, the convective mass flux (M_c) at 4000 m altitude and the deep cloud cover in (top panels) ALP and (bottom panels) DE.

Note that the large $NRI_{\Delta x}^t$ for the 550-m simulation in ALP for the surface rain rate is largely caused by a slight phase shift in the mean diurnal cycle compared to the 1.1-km simulation (cf. Fig. 3.2b) and discussed in Section 3.4.1. As for the total heat tendencies, these are likely to not converge given that they are mostly determined by the grid-dependent subgrid-scale sensible heat flux convergence (cf. Figs. 3.6a and 3.6b). Advection and microphysics are only minor contributors, although these latter tendencies were shown to converge. This is not the case for the total water vapor tendencies, which are largely determined by the resolved advection, and for which also the microphysical contribution is more relevant compared to the total heat tendencies. In DE the resolution sensitivity rarely decreases with Δx and very large values of the $NRI_{\Delta x}^t$ are observed even at fine resolutions. This highlights that bulk convergence is far from reached at these scales over flat terrain.

3.4.3 Structural convergence

In this section, structural convergence of cloud-scale statistics is addressed. A detailed description of the analysis method is given in Section 3.3.3. All statistics are computed for the analysis domains illustrated in Figs. 3.1b and 3.1c.

Figure 3.10 shows the power spectral densities (PSDs) of vertical velocity at 6000 m altitude averaged over the 9-day periods between 1500 h and 2200 h at different horizontal grid spacings for both sets of simulations. The altitude is chosen to analyze only deep convective cells. In Figs. 3.10b and 3.10d the PSDs are multiplied by the wavenumber k to illustrate the energy peak.

All the PSDs deviate quite substantially from the expected k^{-3} dependence on the larger scales, suggesting that a pronounced large-scale atmospheric forcing is absent in both ALP and DE. All the PSDs show a more or less pronounced k$^{-5/3}$ dependence at the mesoscale, whereas at higher wavenumbers the model dissipation removes energy from the resolved scales at finer grid spacings. The effective resolution is about $6\Delta x$ in ALP (4-6Δx in DE) at Δx = 1.1 km and coarser resolutions. At Δx = 550 m the model is more diffusive with an effective resolution of about $10\Delta x$. This may explain the reduced convective activity and precipitation observed in Section 3.4.1, particularly in DE, in which boundary-layer growth plays a more important role than in ALP determining the evolution of convection. Baldauf et al. [2011] showed how reducing the Blackadar length scale l_∞ to 60 m fosters the initiation of convection in a case study of airmass convection over Germany. The spectral peak is shifted to larger wavenumbers at finer Δx, and does not converge at the kilometer scale. This is consistent with e.g. Bryan et al. [2003] and Langhans et al. [2012c]. However, possibly owing to the orographic forcing in ALP, the spectral peak is clearly distinguishable beginning at Δx = 2.2 km, whereas in DE only at Δx = 1.1 km. Note also that there is a good agreement in ALP between the different resolutions with respect to the spectral curves for wavelengths larger than $5\Delta x$, but not in DE.
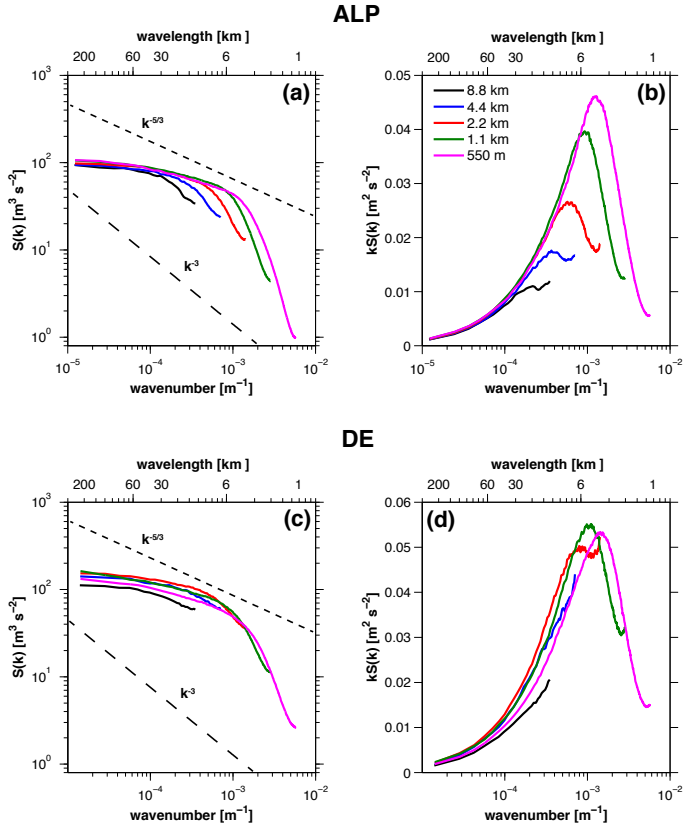
Figure 3.10: Power spectral densities (PSDs) of vertical velocity at 6000 m height averaged between 1500 h and 2200 h in (a) and (b) ALP and (c) and (d) DE. The colors distinguish between the different horizontal grid spacings. In (b) and (d) the PSDs are multiplied by the wavenumber k to illustrate the energy peak.
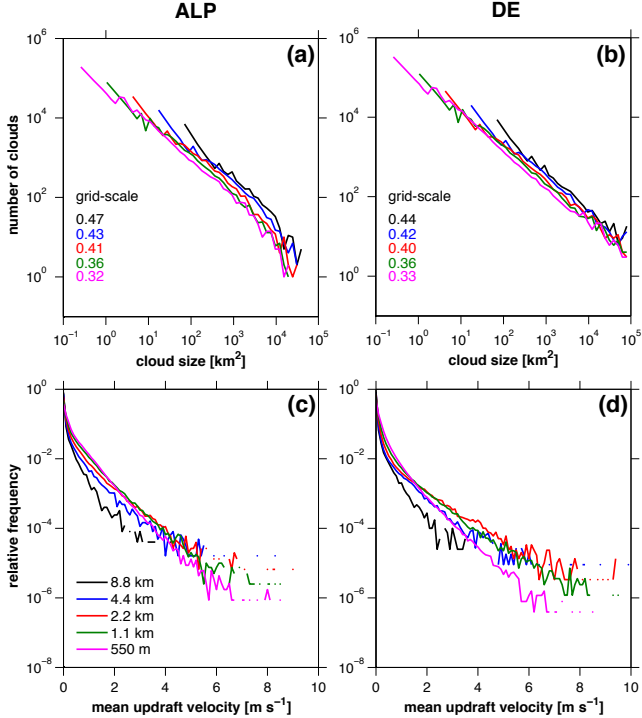
Figure 3.11: (a) and (b) Cloud-size distribution [m^2] in (a) ALP and (b) DE. The bins consist of 50 logarithmically spaced points in the interval [10^{-1},10^5]. The numbers at the bottom left of each panel indicate the fraction of grid-scale clouds (i.e. clouds that are only one grid box in size). (c) and (d) PDFs of mean updraft velocity within the clouds. The bin width is 0.1 m s^{-1}. In all panels the colors distinguish between the different horizontal grid spacings. A detailed description on the computation of these two quantities is given in Section 3.3.3.

Figures 3.11a and 3.11b show the cloud-size distribution computed at each Δx for the two episodes. The numbers at the bottom left corner of each panel indicate the fraction of grid-scale clouds (i.e. clouds that cover only one grid box in size) at every Δx. Although their relative frequency systematically decreases at smaller Δx, the majority of the simulated clouds are grid-scale. This suggests that the size of the smallest convective clouds is largely determined by Δx within the analyzed range of horizontal grid spacings.

There is a good agreement between the model resolutions with respect to the size of the largest cloud clusters, particularly in DE, although there is a tendency for more large clouds at coarse resolution. However, for a given size within the resolved range, more clouds are simulated at coarser resolutions. This is particularly true when the cloud size approaches the size of the model grid.

Figures 3.11c and 3.11d show the probability density functions (PDFs) of mean updraft velocity within the clouds. The PDFs look substantially different across the analyzed range of Δx. A larger frequency of weak updraft velocities is simulated at fine resolutions, owing to the larger numbers of simulated small shallow clouds. Also the frequency of the strongest updrafts changes substantially with the resolution. In particular, at $\Delta x = 8.8\,\text{km}$ the strongest updrafts are not captured. These are indication that convergence of cloud-scale updraft statistics is not reached within the analyzed range of Δx.

3.5   Summary and conclusions

This study investigated both the bulk convergence of domain-averaged and integrated tendencies related to a large ensemble of convective cells and the structural convergence of scales and properties of individual clouds and convective updrafts. Two 9-day episodes of quasiperiodic diurnal moist convection were simulated at horizontal grid spacings $\Delta x = 8.8$, 4.4, 2.2, 1.1 km and 550 m over the Alps (ALP) and over Central Germany (DE) to compare the results in the presence and in the absence of a mesoscale orographic forcing. A revised metric to address bulk convergence was presented to allow for a systematic comparison between the resolutions sensitivity and the model ensemble spread, and thus a more thorough assessment of bulk convergence. The averaged ensemble spread was estimated by means of a 14-member ensemble at $\Delta x = 2.2\,\text{km}$. The choice of this particular resolution was limited by computational constraints, and the resulting ensemble spread must be taken as representative of all the other resolutions. Bulk convergence is obtained when the resolution sensitivity systematically decreases at smaller Δx and is larger than the model ensemble spread.

Bulk convergence was assessed for the mean diurnal cycle and spatial distribution of precipitation, clouds and convective transport of mass, heat and water vapor. Results showed that bulk convergence was systematically achieved for

the spatial distribution of the analyzed quantities. For their mean diurnal cycle, bulk convergence was generally observed in ALP, but not in DE, indicating that the mesoscale thermally-driven forcing reduces the resolution sensitivity of the bulk flow properties. The only exception was the net heating of the lower troposphere, which depended largely on the grid-dependent subgrid-scale sensible heat flux convergence. In DE not only the resolution sensitivity, but also the model ensemble spread was generally larger than in ALP. Also, the clouds in the different ensemble members in DE were randomly distributed in space, whereas in ALP their spatial distribution was surprisingly consistent.

Structural convergence was addressed based on spectral analysis of updraft velocities, cloud-size distributions and probability density functions of mean updraft velocity within the clouds. In line with numerous previous studies [e.g. Bryan et al., 2003; Hanley et al., 2015], a large sensitivity of cloud-scale features was observed in this study. In particular, the size and strength of the convective updrafts, as well as the size of the smallest simulated convective features were found to be largely dependent on Δx, and structural convergence was confirmed to be not yet achieved at the kilometer scale.

This study extends the previous literature by analysing bulk and structural convergence at convection-resolving scales in real-case simulations, rather than focusing solely on one of the two or analyzing idealized simulations. Furthermore, the revised statistics used in this study allowed for a more thorough assessment of bulk convergence. From a practical point of view, the results presented in this study contribute towards an enhanced credibility of convection-resolving models (CRMs). Whereas these models are too coarse to explicitly simulate the scale interactions between small-scale turbulent, microphysical and convective processes, kilometer-scale resolutions are often sufficient for real-case simulations, provided that the focus is on bulk properties and feedbacks rather than on the structure of convective clouds. From the results presented in this study it is evident that, whereas at $\Delta x = 8.8\,\mathrm{km}$ convection is largely unresolved, already at $\Delta x = 4.4\,\mathrm{km}$ the most important bulk properties are consistently captured compared to finer resolutions. In particular the spatial distribution of precipitation, clouds and convective transport appears not to be governed by the small scales, independently from the underlying terrain and dynamical regime. However, for the mean diurnal cycle, this applies solely to episodes of thermally-driven convection over mountainous terrain rather than airmass convection over flat terrain. Furthermore, our analysis confirmed that there is little hope that CRMs would achieve convergence in terms of small-scale structures associated with convective clouds. The goal of kilometer-scale simulations should thus not primarily be to resolve individual convective clouds (which are anyway not predictable).

One key limitation of this study is that the average ensemble spread was estimated only by means of an ensemble at $\Delta x = 2.2\,\mathrm{km}$ due to computational
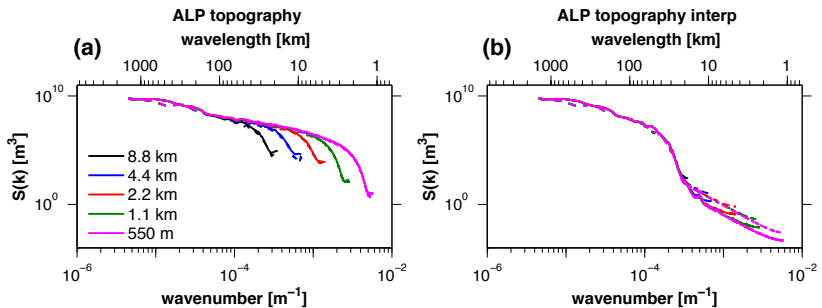
Figure 3.12: Power spectral densities computed for the topography in ALP (a) interpolated on each of the employed model grids and (b) filtered to the 8.8-km grid and successfully interpolated to the higher-resolution grids.

constraints. The increasing computational resources could soon allow to verify whether the estimate is valid also at smaller Δx. Furthermore, the way the ensemble was constructed probably made it under-dispersive. More accurate estimates are necessary to confirm the results presented in this study with regard to bulk convergence.

3.6 Appendix A. Topography filtering

A nearly identical representation of the external parameters at all grid spacings in both physical and spectral space is obtained by interpolating the Δx = 8.8 km external parameters to all the other resolutions. Discrete external parameters (soil type, land fraction, urban area fraction, lake fraction) are interpolated using nearest-neighbor interpolation. All the other parameters (topography, plant characteristics, roughness length, sky view factor and longwave surface emissivity) are interpolated using bilinear interpolation. A 2D Gaussian low-pass filter with an energy cut-off wavelength of approximately 40 km is then applied at all resolutions to remove the variance at smaller wavelengths. A fifth-order Raymond [1988] low-pass filter is applied to the 8.8-km topography prior to the interpolation.
Figure 3.12 shows the power spectral densities computed for the topography in ALP from the raw and interpolated set of external parameters files.

3.7 Appendix B. Sensitivity to model timestep

To touch on the issue of the timestep dependency, with particular regard to the microphysical scheme, two additional sets of simulations are run with a fixed timestep of 5 s at all horizontal grid spacings. A simple bulk convergence analysis based on the mean diurnal cycle of domain-averaged surface rain rate is presented in Fig. 3.13. The left panels illustrate the mean diurnal cycle of
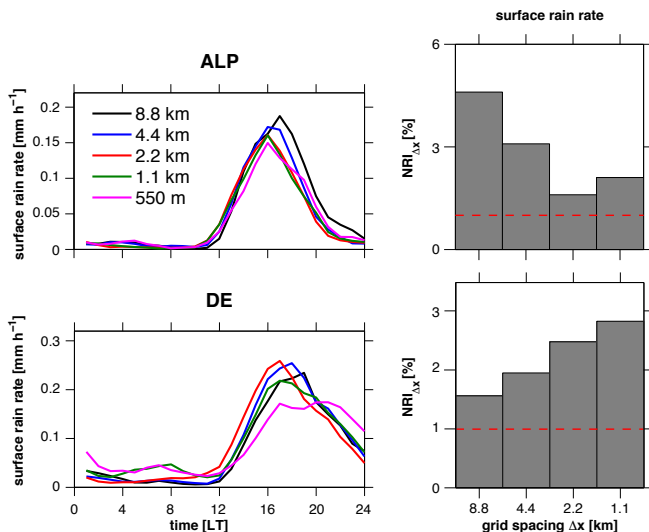
Figure 3.13: As (left panels) Fig. 3.2 and (right panels) Fig. 3.9 but for the sets of simulations with a fixed model timestep of 5 s.

precipitation in ALP and DE. There are only marginal differences compared to the diurnal cycles in Figs. 3.2c and 3.2d, with a slightly earlier initiation of precipitation observed at $\Delta x = 8.8$ km with the 5-s timestep. The right panels illustrate the $NRI_{\Delta x}^{t}$ computed versus Δx for the mean diurnal cycles of surface rain rate in the set with fixed model timestep. The convergence analysis leads to very similar results compared to Fig. 3.9 for the surface rain rate, with the only exception of a smaller $NRI_{\Delta x}^{t}$ at $\Delta x = 8.8$ km owing to the earlier initiation of precipitation. These results suggest that, for the case studies analyzed in this study, the horizontal resolution sensitivity is only marginally affected by the induced changes in model timestep to ensure a fixed CFL criterion at all resolutions.

4

On the subgrid-scale turbulence parameterization at convection-resolving scales and sensitivities of the mean flow properties and characteristics of individual convective cells

Davide Panosetti[1], Linda Schlemmer[1], and Christoph Schär[1]

Abstract   The design of subgrid-scale turbulence parameterizations which work well across the entire range of the so-called "terra incognita", i.e. the scales between the mesoscale limit (no turbulence resolved) and the large-eddy simulation limit (energy-containing eddies resolved), is a big challenge for convection-resolving modeling. Despite several attempts, there is still disagreement on which approach is the best to adopt with regard to turbulence treatment at the kilometer scale. This study aims at investigating the sensitivities stemming from the formulation of subgrid-scale turbulent pro-

[1]Institute for Atmospheric and Climate Science, ETH Zurich, Universitätstrasse 16, 8092 Zurich, Switzerland

cesses with respect to both the mean flow properties and the characteristics of the single convective cells at horizontal grid spacings $\Delta x = 8.8$, 4.4, 2.2, 1.1 km and 550 m. A 1D TKE-based turbulence scheme devised for mesoscale modeling with grid-independent but tunable asymptotic Blackadar turbulent length scale l_∞ and a 3D Smagorinsky turbulence closure devised for LES are compared. Real-case simulations over the Alps and over Central Germany are conducted to compare the results over mountainous and flat terrain. Results show that the mean flow properties are more sensitive to the subgrid-scale turbulence parameterization than to Δx, whereas the opposite is valid for the characteristics of the individual convective cells. Smaller values of l_∞ in the 1D model are associated with lower diffusion, stronger convective cells, reduced cloud cover but thicker clouds, lower cloud base and increased precipitation. These sensitivities are generally more pronounced at coarse resolutions and over flat terrain. Changing the value of l_∞ has little impact on cloud-scale statistics such as the number of grid-scale clouds and the average distance between the cloud clusters, but larger l_∞ reduces the mean updraft velocity of the convective cores. The employment of a 3D Smagorinsky closure at the kilometer scale generally yields similar results of a 1D model with very large values of l_∞, indicating that 3D closures are too diffusive and should not be applied to simulations with $\Delta x = 1.1$ km or coarser resolutions. However, the two become comparable at subkilometer scales, suggesting that 3D closures yield reasonable performances also at scales of a few hundreds meters, and thus larger than those for which they were designed, and that they should preferably be used at scales smaller than a few hundred meters.

4.1 Introduction

Atmospheric turbulence acts over a wide range of spatial scales, from characteristic turbulence production scales (those of the largest boundary-layer thermals) to the Kolmogorov microscale where molecular forces dissipate the turbulent kinetic energy. Modeling atmospheric turbulence in atmospheric models is essential because eddies impact both the mean flow through mixing and the convective clouds through entrainment/detrainment processes.

Two types of models are in principle employed in atmospheric science. Large-eddy simulation (LES) models [e.g. Deardorff, 1970] are able to represent the convective boundary layer (CBL) quite accurately [e.g. Huang et al., 2009] and are used to study turbulent processes and, more recently, boundary-layer clouds in idealized setups. LES models are generally run over relatively small domains due to their large demand for computational resources. Although these models can resolve the largest CBL eddies, they still rely on a parameterization scheme for the small-scale turbulence. At larger scales, such as for operational numerical weather prediction (NWP) and climate models, the horizontal grid spacing ranges from a few hundred kilometers (for global climate models) down to the kilometer scale (for NWP and regional-scale cli-

mate models). It is likely that in the future such models will be operating at subkilometer scales. In such models even the largest CBL eddies are poorly or not at all represented on the grid, and thus a turbulence parameterization must be employed to account for the effects of subgrid-scale miixing as well as entrainment/detrainment processes.

Turbulence parameterization in state-of-the-art NWP and regional-scale climate models generally acts only along one dimension (1D), since at these scales the CBL is assumed to be horizontally homogeneous. This assumption allows for the computation of a vertical turbulent flux only. However, it has been proved by LES studies that in the CBL the horizontal production of turbulence cannot be neglected [e.g. Honnert and Masson, 2014]. This is generally compensated with the use of a digital filter in the horizontal, or a specific formulation for two-dimensional (2D) horizontal diffusion. On the other hand, the small-scale turbulence parameterized in LES models is assumed to be isotropic, and thus three-dimensional (3D) closures are employed. However, as first remarked by Wyngaard [2004], at kilometer-scale resolutions the turbulence structures are neither entirely subgrid-scale nor explicitly resolved. He called this the "terra incognita". At these resolutions in principle neither 1D turbulence schemes devised for mesoscale modeling nor 3D turbulence closures devised for LES should be employed [e.g. Bryan et al., 2003; Honnert et al., 2011].

Several studies have been conducted with the aim of adapting the current approach to turbulence parameterization at the kilometer scale to the terra incognita. These include, for instance, the use of blended 3D Smagorinski with a 1D non-local turbulence scheme [Boutle et al., 2014], the extension of the traditional Mellor and Yamada [1974] scheme by modifying the turbulent length scales using statistics derived from LES [Ito et al., 2015], and the employment of hybrid local/non-local schemes [Shin and Hong, 2015]. However, there is still disagreement on which approach it is best to adopt with regard to turbulence treatment at the kilometer scale.

In this chapter we explore the sensitivities of the mean flow properties and the characteristics of the simulated convective cells to the employment of a 1D TKE-based turbulence parameterization devised for mesoscale modeling with a fixed (but varying in magnitude) asymptotic Blackadar turbulent length scale, and a 3D turbulence closure devised for LES at different horizontal grid spacings. Several previous studies have reported large sensitivities in real-case simulations over Central Europe to both the asymptotic Blackadar turbulent length scale in the 1D model [e.g. Baldauf et al., 2011], particularly for cases with low synoptic forcing, and the employment of a 1D vs 3D model at the kilometer scale [e.g. Barthlott and Hoose, 2015]. In this study, real-case simulations over the Alps and over Central Germany are run to compare the results over flat and mountainous terrain.

The numerical model and the experimental design are presented in Section 4.2. In Section 4.3.1 the sensitivities related to the mean flow properties

are presented. In Section 4.3.2 the structural changes in the cloud field are discussed. The summary and conclusions are given in Section 4.4.

4.2 Methods

4.2.1 Model description

For this study a series of numerical simulations are performed using version 5.0 of the Consortium for Small-Scale Modeling (COSMO) model [Baldauf et al., 2011]. The COSMO model is a non-hydrostatic, fully compressible limited-area model designed for both operational high-resolution NWP and research applications on a broad range of spatial scales. It employs an Arakawa C-grid for horizontal differencing on a rotated latitude/longitude grid. A third-order Runge-Kutta scheme [Wicker and Skamarock, 2002] is used for time integration. A fifth-order upwind scheme is used for horizontal advection temperature, pressure, and horizontal and vertical winds, and a second-order scheme [Bott, 1989] is employed for horizontal advection of moist quantities.

The physical parameterizations include a single-moment bulk microphysics scheme after Reinhardt and Seifert [2006] which includes riming processes (graupel formation) and predicts cloud water, rain water, cloud ice, snow and graupel, and a radiative transfer scheme based on the δ-two-stream approach [Ritter and Geleyn, 1992] in which radiation interacts with both subgrid- and grid-scale clouds. A 10-layer land-surface model (TERRA_ML; Heise et al., 2003) is implemented, and a Louis surface transfer scheme [Louis, 1979] is used to calculate the transfer coefficients which yield the surface sensible and latent heat fluxes based on Monin-Obukhov Similarity Theory.

Two different methods to parameterize turbulence are considered in this study: a 1D TKE-based turbulence scheme devised for mesoscale modeling and a 3D Smagorinsky turbulence closure devised for LES. None of these two models was originally designed to operate at scales of $\mathcal{O}(1\,\mathrm{km})$. Both methods describe the subgrid-scale turbulent fluxes by applying the eddy-viscosity assumption and the gradient-diffusion hypothesis (K-theory).

1D TKE-based parameterization

The 1D model is based on a prognostic equation for turbulent kinetic energy (TKE) [Raschendorfer, 2001] and can be classified as Mellor-Yamada level 2.5 [Mellor and Yamada, 1974]. This scheme uses the so-called boundary layer approximation by imposing horizontal homogeneity of the variables. The vertical eddy viscosities for heat K_h^V and momentum K_m^V are determined using the Prandtl-Kolomogorov specification as:

$$K_{h,m}^V = \phi_{h,m} l_v \sqrt{2e} \qquad (4.1)$$

The characteristic Blackadar length scale l_v [Blackadar, 1962] for vertical mixing is calculated according to:

$$l_v = \frac{kz}{1 + (kz)/l_\infty} \tag{4.2}$$

where k is the von-Karman constant, z is the altitude, and l_∞ is an asymptotic length scale which is varying in the different experiments (see Table 4.1 for details). $\phi_{h,m}$ are stability-dependent coefficients, and $\bar{e} = \overline{(u_i' u_i')}/2$, with $i = 1, 2, 3$, is the subgrid-scale TKE per unit mass. The overbar denotes a time mean, and the primes indicate subgrid-scale variables.

In the horizontal, second-order horizontal diffusion is computed following Smagorinsky [1963]. The eddy viscosities $K_{h,m}^H$ are related to the 2D grid-scale rate of strain as:

$$K_{h,m}^H = [c_s \sqrt{\Delta x \Delta y}]^2 \sqrt{[(D_{11} - D_{22})^2 + 4D_{12}^2]} \tag{4.3}$$

where $D_{ij} = \frac{1}{2}\left(\frac{\partial u_i}{\partial x_j} + \frac{\partial u_j}{\partial x_i}\right)$ with $i = 1, 2$ is the 2D grid-scale rate of strain, and $c_s = 0.25$ is the Smagorinsky constant.

3D Smagorinsky closure

The 3D model was designed for LES applications to simulate the energy transfer from the resolved to the unresolved scales across an inertial subrange of locally isotropic, 3D turbulence. Therefore, all variances of turbulent fluctuations appearing in the Reynolds-averaged equations are considered [Doms et al., 2011]. Following Lilly [1962] and Smagorinsky [1963] the eddy viscosities for momentum are given by:

$$K_m^{H,V} = l_s^2 D \sqrt{1 - \frac{Ri}{Pr}} \tag{4.4}$$

where $D = \sqrt{2D_{ij}D_{ji}}$ is the grid-scale rate of strain, and l_s is given by Deardoff's proposal as $l_s = c_s(\Delta x \Delta y \Delta z)^{1/3}$ with the Smagorinsky constant c_s set again to 0.25. Ri the deformation Richardson number, which is a function of moist static stability [see Langhans et al., 2012c], and Pr is the Prandtl number.

4.2.2 Experimental setup

The simulations are initialized and hourly boundary conditions are provided by a 12-km run driven by ERA-Interim reanalysis data at a horizontal resolution of 0.7° [Dee et al., 2011] covering a large domain centered over Continental Europe (Fig. 4.1a). Initial soil moisture is obtained from a 10-year long climate simulation with parameterized convection over the same model
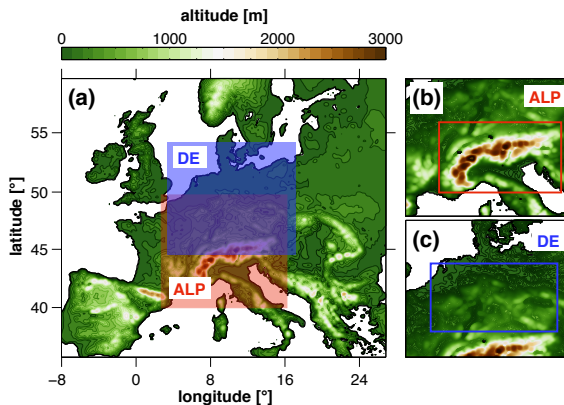
Figure 4.1: (a) Integration domain and topography [m] of the 12-km driving model. The integration domains of ALP and DE are illustrated by the blue and red boxes respectively. (b,c) Same as (a) but for (b) ALP and (c) DE at $\Delta x = 2.2\,\text{km}$. The analysis domains for each set of simulations are illustrated by the red and blue boxes.

domain [Ban et al., 2014].

The simulations are run at $\Delta x = 8.8, 4.4, 2.2, 1.1\,\text{km}$ and 550 m. The long time steps used are 80, 40, 20, 10 and 5 s, respectively. The model output is dumped to file at every hour. The integration domains are $1160 \times 1090\,\text{km}^2$ large and centered over the Alps (ALP) and Central Germany (DE) (Figs. 4.1b and 4.1c). In the vertical direction, a pressure-based hybrid coordinate is used with 79 stretched model levels from the surface to the model top at 21 km. The vertical grid spacing varies from 20 m near the surface to 800 m above 18 km. At the upper domain boundary a rigid lid is employed, and a Rayleigh damping layer extends from 11.5 km to the top of the domain to minimize spurious reflections of gravity waves. 10 soil layers with thickness ranging from 1 cm for the uppermost layer to 5.76 m for the lowermost are used, and the total soil depth is 15.34 m.

The soil type is determined from the Harmonized World Soil Database (HWSD) TERRA at a grid cell size of 1 km. Land use data are retrieved from the high-resolution ($\Delta x = 300\,\text{m}$) GLOBCOVER dataset. The ASTER Global Digital Elevation Map (GDEM; horizontal resolution of roughly 30 m at the Equator) is used for topography data. For this study the resolution of the external parameters is kept constant across resolutions to avoid more detailed structures on finer grids and to isolate the changes due to different Δx from those due to the modified external forcing (for details see Panosetti et al., 2019).

Two 9-day episodes of quasiperiodic diurnal moist convection, 11-20 July 2006 for ALP [e.g. Langhans et al., 2012c] and 04-13 June 2007 for DE [e.g.

Name	Turbulencescheme	Gridspacing
l20	1D TKE, $l_\infty = 20$	8.8, 4.4, 2.2, 1.1 km
l60	1D TKE, $l_\infty = 60$	8.8, 4.4, 2.2, 1.1 km
l100	1D TKE, $l_\infty = 100$	8.8, 4.4, 2.2, 1.1 km, 550 m
l200	1D TKE, $l_\infty = 200$	8.8, 4.4, 2.2, 1.1 km
l320	1D TKE, $l_\infty = 320$	8.8, 4.4, 2.2, 1.1 km
3D	3D Smagorinsky	8.8, 4.4, 2.2, 1.1 km, 550 m

Table 4.1: List of different configurations with regard to subgrid-scale turbulence treatment

Keller et al., 2016] are considered in this study. These two episodes are representative of frequently-observed summertime conditions in Europe in which convection occurs in response to the diurnal cycle of incoming solar radiation, often in the absence of large-scale forcing. The analysis is performed over two domains of equal area illustrated by the red and blue boxes in Figs. 4.1b and 4.1c. The experiments and the different configurations are listed in Table 4.1. Five different values of the asymptotic Blackadar turbulent length scale l_∞ are tested for the 1D model for each of the two episodes. These include the range of values (l60-l200) which are typically used for operational and research purposes in COSMO [e.g. Baldauf et al., 2011; Ban et al., 2014; Leutwyler et al., 2016; Panosetti et al., 2019] but also in other NWP models such as the European Center for Medium-Range Weather Forecasts (ECMWF) Integrated Forecast System (IFS), and two values which are generally considered very large (l320) and very small (l60) and are rarely used for real-case applications. $\Delta x = 550$ m simulations are run only for l100 (which is within the range of the commonly-used values of l_∞) and for 3D due to the large computational resources required.

4.2.3   Heat and water vapor budgets formulation

To study the sensitivity of the large-scale flow properties, the heat and water vapor budgets of a large control volume covering the analysis domain in the horizontal are considered. The top of the control volume is located at 4000 m altitude so that the volume-averaged tendencies are representative of deep convective fluxes toward the upper atmosphere (plus a small contribution from lateral fluxes in and out of the control volume).
The processes contributing to the instantaneous local heating and cooling of the atmosphere are given by:

$$\frac{\partial \theta}{\partial t} = -\mathbf{v} \cdot \nabla \theta - \frac{1}{\rho c_p}(\nabla \cdot \mathbf{H}) - \frac{1}{\rho c_p}(\nabla \cdot \mathbf{R}) + L_m \qquad (4.5)$$

where θ is the potential temperature, $\mathbf{v}$ the wind speed vector, ρ is the air density, c_p is the heat capacity at constant pressure, $\mathbf{H} = \rho c_p \overline{\mathbf{v}'\theta'}$ is the

subgrid-scale sensible heat flux, $\mathbf{R}$ is the radiative energy flux, and L_m is the latent heating rate. The primes denote subgrid-scale variables. The overbar indicates a time average. All the terms in Eq. 4.5 are extracted using the budget tool implemented in the COSMO-Model [Langhans et al., 2012b].

To study the convergence of the bulk tendencies, the net effect of each process is computed on a control volume V of total mass $M = \int_V \rho dV$ by integrating Eq. 4.5 over V. The volume-averaged density-weighted heat budget equation is:

$$
\underbrace{\frac{1}{M}\int_V \rho \frac{\partial \theta}{\partial t} dV}_{\text{TOT}} = \underbrace{-\frac{1}{M}\int_V \rho \mathbf{v}\cdot\nabla\theta\, dV}_{\text{ADV}} + \underbrace{\frac{1}{M}\int_V -\frac{1}{c_p}(\nabla\cdot\mathbf{H})dV}_{\text{UNRES}}
$$

$$
+ \underbrace{\frac{1}{M}\int_V -\frac{1}{c_p}(\nabla\cdot\mathbf{R})dV}_{\text{RAD}} + \underbrace{\frac{1}{M}\int_V \rho L_m\, dV}_{\text{MIC}} \quad (4.6)
$$

where TOT is the heat storage tendency, ADV is the heat advection, UNRES is the subgrid-scale sensible heat flux convergence, RAD is the radiative flux convergence and MIC is the microphysics contribution (primarily latent heat exchange due to condensation of water vapor and evaporation of rain).

Similar to the heat budget equation, the water vapor budget equation can be written in its volume-integrated density-weighted form as:

$$
\underbrace{\frac{1}{M}\int_V \rho \frac{\partial q_v}{\partial t} dV}_{\text{TOT}} = \underbrace{-\frac{1}{M}\int_V \rho \mathbf{v}\cdot\nabla q_v\, dV}_{\text{ADV}} + \underbrace{\frac{1}{M}\int_V -\frac{1}{l_v}(\nabla\cdot\mathbf{L})dV}_{\text{UNRES}}
$$

$$
+ \underbrace{\frac{1}{M}\int_V \rho S_m\, dV}_{\text{MIC}} \quad (4.7)
$$

where TOT is the water vapor storage tendency, ADV is the water vapor advection, UNRES is the subgrid-scale latent heat flux convergence and MIC is the microphysics contribution. q_v is the specific water vapor, l_v is the latent heat of vaporization, $\mathbf{L} = \rho l_v \overline{\mathbf{v}' q_v'}$ is the subgrid-scale latent heat flux, and S_m are microphysical source/sink rates. Note that for both the heat and water vapor budgets all the tendencies are diagnosed except ADV, which is derived as residual.

4.3 Results

This section is divided into two parts. First the sensitivities related to the (bulk) mean flow properties is presented. Second, the changes in the characteristics of the simulated cloud field are discussed.

4.3.1 Mean flow properties

Figures 4.2a and 4.2b illustrate the domain-averaged surface precipitation in ALP and DE simulated at different Δx and with different subgrid-scale turbulence parameterizations. In ALP the precipitation systematically decreases at smaller Δx and with a larger l_∞ when the 1D model is employed. With the 3D model, the precipitation increases at smaller Δx. In DE the changes due to both Δx and l_∞ are less systematic, although there is a tendency for less precipitation with larger l_∞, particularly at coarse resolutions, and for an increased precipitation at smaller Δx when the 3D model is employed. Figures 4.2c and 4.2d illustrate the changes in liquid water path (LWP) due to Δx and the employed turbulence model. The LWP decreases for larger values of l_∞ in the 1D model in both episodes. There is little sensitivity to Δx when the 1D model is employed, but this becomes larger when the 3D model is employed, with a tendency for lower LWP at smaller Δx, particularly in ALP. Figures 4.2e and 4.2f show the changes in cloud cover. The cloud cover increases for larger l_∞, indicating that the simulated clouds are thinner, since the smaller amount of liquid water is distributed among a larger number of grid boxes. On the other hand, consistently with what observed in Figs. 4.2c and 4.2d the cloud cover decreases with smaller Δx, indicating that there are no significant changes in the thickness of the simulated cloud field with resolution. The cloud cover when the 3D model is employed is generally comparable with the one of a 1D model with large values of l_∞. Figures 4.2g and 4.2h show the sensitivities for the average cloud base height. For both episodes the changes due to the employed subgrid-scale turbulence parameterization are much more pronounced than the changes due to Δx when the 1D model is employed. In particular, the larger l_∞ the higher the average cloud base, with the sensitivities being larger in DE compared to ALP. On the other hand, with the 3D model the average cloud base decreases at smaller Δx. To illustrate the sensitivities of the different terms of the heat (Eq. 4.6) and water vapor (Eq. 4.7) budget equations for the lower atmosphere (see Section 4.2.3 for a detailed description of the budget), the mean diurnal cycle of specific heat and water vapor tendencies within the control volume are shown in Figs. 4.3 and 4.4. Only the mean diurnal cycles at $\Delta x = 2.2$ km are shown but a similar behavior is observed at all resolutions. The tendencies averaged over the entire diurnal cycle for the diabatic terms are shown in Fig. 4.5. Similar sensitivities are observed in DE, therefore the data is shown only for ALP. Considerable compensation is observed among the diabatic tendencies (see also Langhans et al., 2012c) which reveal significant dependence on the subgrid-scale turbulence treatment and, to a lesser extent, on Δx when the 3D model is employed. When l_∞ in the 1D model is smaller, subgrid-scale processes such as entrainment of heat and detrainment of moisture at the top of the PBL decrease. Thus, the control volume remains cooler and more humid. This in turn increases condensation of water vapor and latent heat release, which compensates for the changes
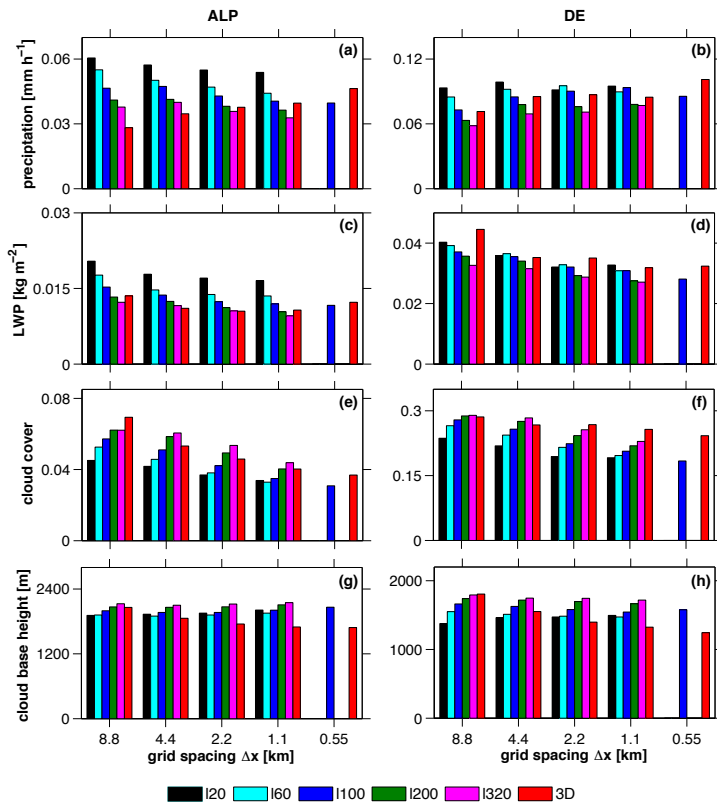
Figure 4.2: 9-day domain-averaged (a) and (b) surface precipitation [mm h^{-1}], (c) and (d) cloud cover and (e) and (f) cloud base height [m] versus the horizontal grid spacing (Δx) in (a), (c) and (e) ALP and (b), (d) and (f) DE. The colors distinguish between the different subgrid-scale turbulence treatments.
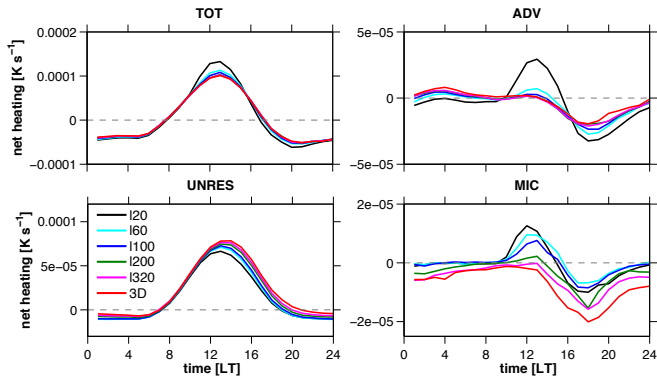
Figure 4.3: Mean diurnal cycles of volume-averaged density weighted heat tendencies in ALP. TOT is the net tendency, ADV the total advection, UNRES is the subgrid-scale sensible heat flux convergence and MIC is the contribution from the microphysics. The colors distinguish between the different subgrid-scale turbulence treatments. The integration volume covers the entire analysis domain in the horizontal and has a top at 4000 m altitude.
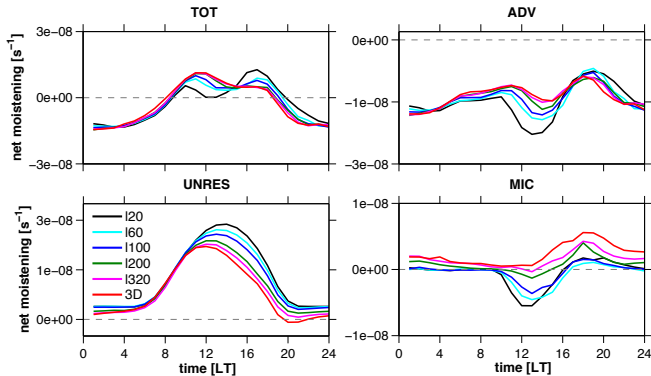

Figure 4.4: As Fig. 4.3 but for the water vapor tendencies. UNRES is the subgrid-scale latent heat flux convergence.
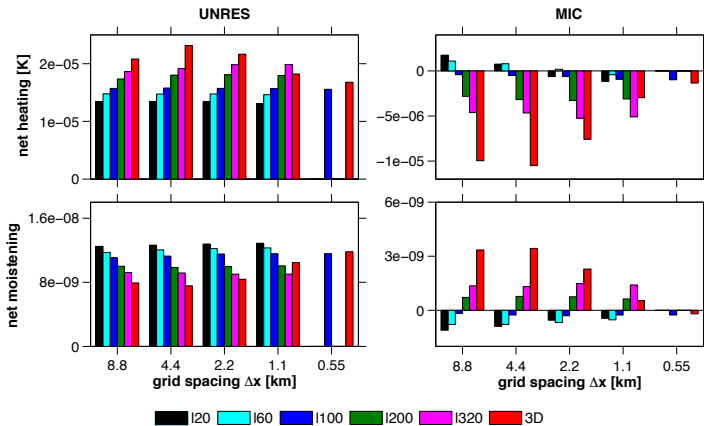
Figure 4.5: As Fig. 4.2 but for the diabatic tendencies of the heat (left) and water vapor (right) budgets in ALP.

in the subgrid-scale tendencies. A similar reasoning applies to the Smagorinsky length scale l_s in the 3D model. This explains what is observed in Figs. 4.2c-f, since a cooler lower atmosphere and an increased condensation leads to larger values of LWP and a lower cloud base height.

Owing to this compensation the changes in the net tendencies are mostly modulated by the (total, but primarily vertical) advection, which is stronger when the diffusivity is lower. As a result, the control volume is warmer during the diurnal peak, drier during the early afternoon hours and more humid during the late afternoon hours.

4.3.2 Characteristics of the individual convective cells

To identify the dominant size of the convective updrafts a spectral analysis is performed on the vertical velocity field. Figure 4.6 shows the power spectral densities (PSDs) computed for the vertical velocity at 6000 m altitude in ALP for all experiments. The PSDs are averaged between 8 LT and 20 LT to capture the most active period of convection.

The computed spectras are extremely sensitive to l_∞ when the 1D model is employed. The larger l_∞, the less the variance (i.e. total energy) in the resolved vertical velocity field. Furthermore, a very diffusive setup generally shifts the energy peak toward smaller wavenumbers (or larger length scales), although the sensitivity is larger at coarser resolutions and much smaller compared to the changes due to Δx. At $\Delta x = 8.8$ km for most of the experiments the energy peaks at the smallest resolvable scale, indicating that none of the energy transfer from the dominant to the smallest length scales is explicitly resolved by the model. In this context, the 3D model is comparable to a very
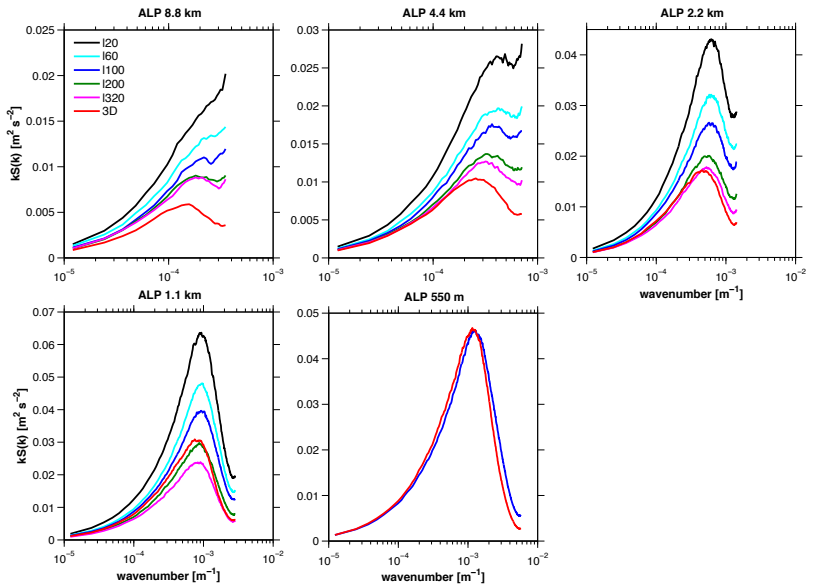
Figure 4.6: Power spectral densities of vertical velocity averaged between 8 LT and 20 LT in ALP. The wavenumber k is computed as $2\pi/\lambda$.
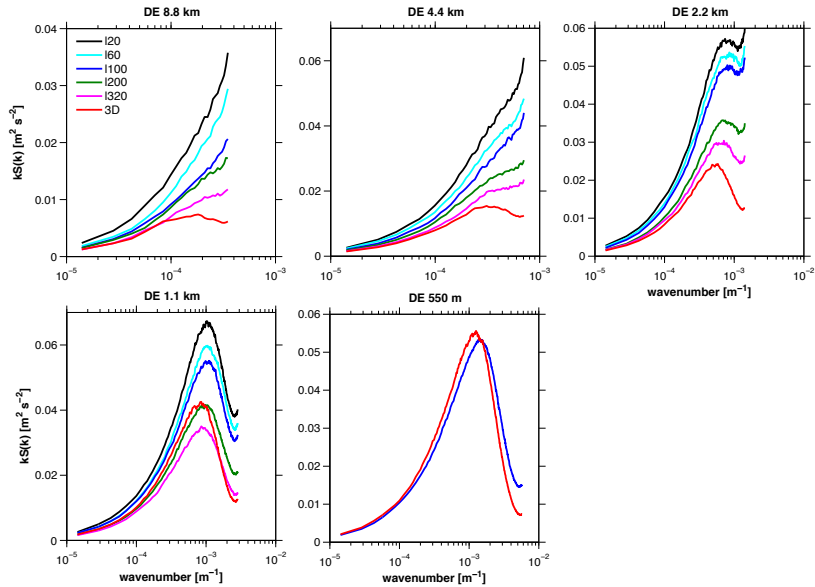
Figure 4.7: As Fig. 4.6 but for DE.

diffusive setup for the 1D model at all resolutions except $\Delta x = 550\,\mathrm{m}$, at which the PSDs are comparable between the two turbulence models. This indicates that from a turbulence perspective the two schemes perform similarly at these scales. Figure 4.7 is as Fig. 4.6 but for DE. Although all the features discussed above are valid for DE as well, only at $\Delta x = 1.1\,\mathrm{km}$ the dominant scales of motion are larger than the model grid. This is explained by the different orography in ALP and DE, in that over mountainous terrain the upslope winds generate circulations that are larger than the model grid and the spectral energy peak shifts toward smaller and more resolvable wavenumbers. Figures 4.8a and 4.8b illustrate the sensitivities related to the fraction of grid-scale clouds (i.e. clouds that are only one grid box in size) in the different simulations. Although there is a general tendency for a larger fraction of grid-scale clouds for small values of l_∞ when the 1D model is employed, for this statistics the changes due to Δx are much more relevant. In particular, the smaller Δx the lower the fraction of grid-scale clouds. Whereas this applies also when the 3D model is employed, the grid-scale cloud fraction increases by 10-15% at all resolutions compared to the 1D model.

Figures 4.8c and 4.8d are as Figs. 4.8a and 4.8b but for the average distance (in number of grid points) between the clouds. Also for this statistics the sensitivity is dominated by Δx when the 1D model is employed, with greater number of grid points between the simulated convective cells at smaller res-
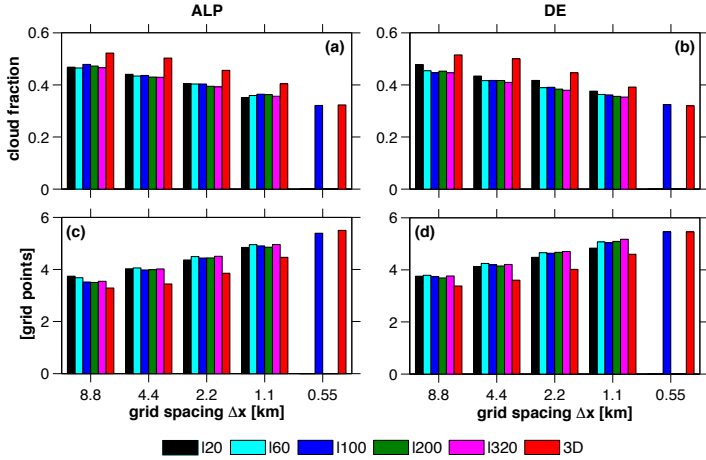
Figure 4.8: As Fig. 4.2 but for (a) and (b) the grid-scale cloud fraction (i.e. clouds that are only one grid box in size) and (c) and (d) for the average distance between the clouds (in number of grid points) in (a) and (c) ALP and (b) and (d) DE.

olutions. No correlation can be found between the average distance between the clouds and the value of l_∞ in the 1D model. The employment of a 3D model reduces the average distance at all resolutions, but the numbers are comparable with the 1D model at subkilometer scales.   Figure 4.9 show the probability density functions (PDFs) of mean updraft velocity within each of the cloud clusters in ALP. Figure 4.10 is as Fig. 4.9 but for DE. The larger the value of l_∞ in the 1D model the lower the mean updraft velocity within the cloud clusters. This is consistent with Section 4.3.1, and highlights that the convective cells are less vigorous and generate less precipitation when l_∞ is larger. Also consistently with the statistics presented above, the 3D model performance always corresponds to the one of a strongly diffusive 1D model, but the two become comparable at subkilometer scales.

4.4   Summary and conclusions

In this study the sensitivities of the mean flow properties and the characteristics of the individual convective cells to the employment of a 1D TKE-based turbulence parameterization devised for mesoscale modeling with a fixed (but varying in magnitude) asymptotic Blackadar turbulent length scale l_∞ and a 3D Smagorinsky turbulence closure devised for LES at convection-resolving scales were explored. Two 9-day episodes of reoccurring diurnal moist convection over the Alps and over Central Germany were considered and several
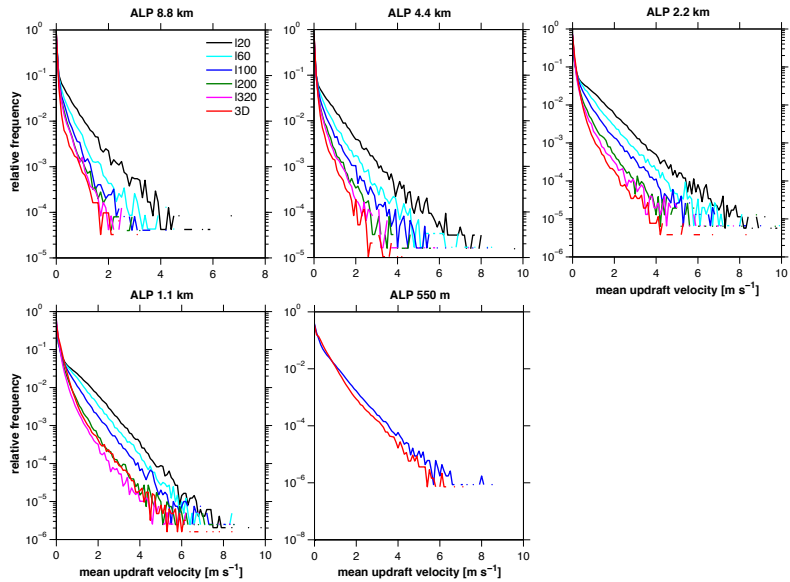
Figure 4.9: Probability density functions of mean updraft velocity within the clouds in ALP. The colors distinguish between the different subgrid-scale turbulence treatments.
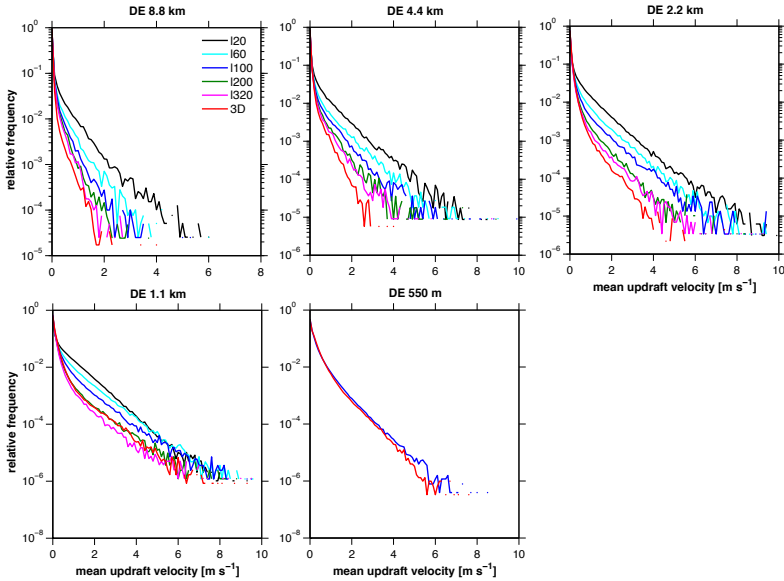
Figure 4.10: As Fig. 4.9 but for DE.

simulations at horizontal grid spacings $\Delta x = 8.8$, 4.4, 2.2, 1.1 km and 550 m were run to compare the results over mountainous and flat terrain.

Results showed that changing the value of l_∞ in the 1D model has a significant impact on the mean flow properties for a fixed Δx, and that for the range of resolutions considered in this study the changes due to the subgrid-scale turbulence treatment are much larger than the changes due to larger or smaller Δx. In particular, more diffusion, an increased cloud cover, thinner clouds, higher cloud base and reduced precipitation were observed for larger l_∞. Significant compensation was found for the diabatic terms of the heat and water vapor budgets of the lower atmosphere, with increased condensation (and latent heat release) making up for the reduced tendencies due to the subgrid-scale fluxes. Weaker (grid-scale) convective transport was also observed for larger l_∞.

The characteristics of the individual convective cells also changed depending on the value of l_∞. However, the changes were comparable or often less significant than the changes induced by different Δx. Spectral analysis of updraft velocity showed that the total variance is reduced for larger l_∞, but the spectral peak (i.e. the dominant length scale) does not change with l_∞ for a fixed Δx. Little sensitivity to l_∞ was found for the fraction of the total number of simulated clouds that are only one grid box in size, as well as for the average distance between the clouds, which are mostly determined by Δx.

On the other hand, significant dependency was found for the mean updraft velocity of the cloud clusters, with weaker updraft cores for larger l_∞.

The employment of a 3D Smagorinsky turbulence closure generally yielded similar results to the employment of a 1D model with very large values of l_∞, except for a larger number of grid-scale clouds at all resolutions. This indicates that 3D turbulence closure are too diffusive when applied at Δx larger than 1 km. However, the two schemes became comparable at $\Delta x = 550$ m, suggesting that 3D turbulence closures yield reasonable performances at scales of a few hundreds meters, and thus larger than those for which they were designed.

This analysis confirms the results of previous studies [e.g. Baldauf et al., 2011] that the asymptotic Blackadar length scale l_∞ is a sensitive parameter in simulations of airmass convection over land. It also extends the previous findings by showing that these sensitivities are slightly larger over flat than mountainous terrain, and that the mean flow properties are more sensitive to l_∞ than to Δx, whereas the opposite applies to statistics at the scale of single clouds or single convective updrafts. Overall, these results confirm that the parameterization of the planetary boundary layer is of great importance at convection-resolving scales, and highlight the high demand for scale-aware turbulence closures. On the other hand, this study supports previous findings [e.g. Honnert, 2016] that 3D turbulence closures should be applied at Δx of a few hundred meters and finer resolutions.

5

Conclusions and Outlook

The resolution sensitivity and convergence behavior of convection-resolving simulations of summertime deep convection over land were analyzed in this thesis. In this last chapter, the conclusions emerging from each of the three chapters are synthesized and possible directions for future research are presented.

5.1 Conclusions

A first-of-its-kind systematic comparison between the *bulk convergence* of domain-averaged and integrated properties related to a large ensemble of convective cells and the *structural convergence* of scales and properties of individual clouds and updrafts was presented in Chapter 2. Idealized simulations were performed and a number of different experiments were conducted. Results highlighted that bulk convergence is generally achieved at the kilometer scale in idealized simulations for the domain-averaged surface rain rate, the integrated atmospheric heat and water vapor budgets, and for a few terms of the surface radiation budget. This was observed in the presence and in the absence of orography and environmental vertical wind shear, as well as in simulations in which the land-surface and radiation schemes were switched off. In contrast, despite the evidence that for some statistics related to updraft velocity and convective mass fluxes the resolution sensitivity decreases at the kilometer scale and finer grid spacings, structural convergence was not yet fully achieved. In particular, smaller and more numerous clouds

were observed at higher resolutions, and the maximum updraft velocity and the size of the smallest simulated clouds were found to be very sensitive to the employed horizontal grid spacing.

Chapter 3 extended the results of Chapter 2 by addressing bulk and structural convergence at convection-resolving scales in real-case simulations. Bulk convergence was analyzed not only for the mean diurnal cycle of precipitation, cloud cover and convective fluxes of heat, water vapor and mass, but also for the spatial distribution of their integrated values. A new statistics was introduced to systematically compare the resolution sensitivity with the average ensemble spread, thus allowing for a more thorough assessment of bulk convergence. Two episodes of quasiperiodic thermally-driven convection over the Alps and airmass convection over Central Germany were investigated to compare the results in the presence and in the absence of a mesoscale orographic forcing. Results revealed that bulk convergence is systematically achieved for the spatial distribution of the analyzed quantities in both episodes. For their mean diurnal cycle, bulk convergence was generally observed only in simulations over the Alps, highlighting the role of the mesoscale orographic forcing in fostering the convergence of bulk flow properties. Structural convergence was confirmed to be not yet fully achieved at the kilometer scale. In particular, large sensitivities to the employed resolution of the mean updraft velocity inside the convective clouds and the size of the smallest simulated clouds were observed.

In Chapter 4, the sensitivities of the mean flow properties and the characteristics of the individual convective cells to the employment of a 1D TKE-based turbulence parameterization devised for mesoscale modeling with a grid-independent but tunable vertical Blackadar asymptotic turbulent length scale, and a 3D turbulence closure devised for LES at different horizontal grid spacings were explored. Several real-case simulations were run over the Alps and over Central Germany to compare the results over mountainous and flat terrain. Results showed that smaller asymptotic turbulent length scales in the 1D model are associated with reduced diffusion, stronger convective cells, lower cloud base, thicker clouds but reduced cloud cover, and more precipitation. These sensitivities are more pronounced at coarse resolutions and over flat terrain. On the other hand, the size of the smallest simulated convective features were relatively insensitive to the employed subgrid-scale turbulence parameterization, and largely determined by the model grid spacing. The employment of a 3D turbulence closure yielded similar results to a largely diffusive 1D model at the kilometer scale and coarser resolution, suggesting that 3D schemes should not be applied at such scales. However, the two became comparable at subkilometer scales, indicating that 3D schemes yield reasonable results at scales larger than those for which they were designed, and that they are more suitable for mesh grids smaller than a few hundred meters.

The results presented in this thesis demonstrate that the resolution sensitiv-

ity of bulk flow properties is much lower than the one of cloud-scale statistics at convection-resolving scales. This implies that kilometer-scale resolutions are often sufficient for simulations of diurnal moist convection over land, provided that the focus is on the bulk properties and feedbacks rather than on the structural details of convective clouds. In particular, the spatial distribution of precipitation, clouds and convective transport appears to converge at the kilometer scale, independently from the underlying terrain and dynamical regime. This applies less rigorously to the mean diurnal cycle of the analyzed quantities, for which both the initiation time and diurnal peak appear to be sensitive to the horizontal grid spacing. On the other hand, the analysis presented in this thesis confirmed that the treatment of subgrid-scale turbulence is a major source of uncertainty in convection-resolving simulations. In particular the mean flow properties are sensitive to the employed turbulence parameterization. On the other hand, the findings presented in this thesis highlight that 3D turbulence closures are in principle applicable to convection-resolving simulations employing horizontal grid spacings finer than 1 km.

Bulk convergence was generally achieved for a variety of model setups and environmental cases in idealized simulations. Moreover, bulk convergence was proven on smaller domains and at shorter time scales compared to previous studies. In real-case simulations, bulk convergence is systematically achieved for the spatial distribution of the analyzed quantities, independently of the underlying terrain. For their mean diurnal cycle, bulk convergence can be generally observed over mountainous terrain in the presence of a mesoscale orographic forcing such as Alpine-scale thermally-driven wind systems, but not over flat terrain. The strong spatial heterogeneity and complexity of the model external parameters is likely to be the reason why convergence can be less rigorously demonstrated in real-case simulations compared to idealized simulations. Other factors such as the time frequency and spatial resolution of the model boundary conditions may also contribute. Nevertheless, the analysis presented in this thesis highlights that the hypothesis of bulk convergence at the kilometer scale cannot be rejected. This result is particularly encouraging in the view of convection-resolving climate simulations, and supports the physical validity of the approach.

The overall conclusion of this thesis is that kilometer-scale resolutions are often sufficient to successfully simulate the bulk flow properties and the feedbacks between convective clouds and the large-scale environment. On the other hand, this thesis confirms that convection-resolving models operate at horizontal grid spacings that are too coarse to simulate the full scale interactions between small-scale turbulence and convective processes. In particular, subgrid-scale turbulence parameterization must be formulated with care in convection-resolving models, and may be important to ultimately determine the mean flow properties.

5.2 Outlook

Several scientific questions emerge from the results presented in this thesis. Moreover, several aspects related to kilometer-scale modeling of moist convection over land, and particularly over mountainous terrain, remain unanswered. Further research efforts are necessary to address the following questions:

- The main result of this thesis is that the resolution required to successfully capture the feedbacks between convection and the large scale is lower than the one required to simulate the structural details of the cloud field. However, the analysis was limited to heat, water vapor and mass fluxes. Momentum fluxes are equally important, particularly over mountainous terrain. A potential extension of this thesis is to investigate the resolution requirements to successfully simulate how convection feeds back onto the divergent component of the large-scale flow.

- The sole focus on the horizontal grid spacing in this thesis and several other studies is motivated by previous findings [e.g. Bryan et al., 2003; Skamarock, 2004] demonstrating that the effective resolution of convection-resolving models is limited by the horizontal rather than by the vertical grid spacing. However, a sufficiently well resolved PBL is key to a realistic simulation of the initiation and development of moist convection over land, and particularly over mountainous terrain (see also Appendix A). More effort needs to be put into understanding more about the role of vertical resolution.

- In Appendix B both the average and grid-scale flow properties were shown to be sensitive to the resolution of the model external parameters (topography, land surface, ...) in real-case simulations. An emerging extension of this study is to separate the effect caused by a better resolved topography and the effect caused by better resolved surface fields (such as land use, urban areas, etc..).

- Chapter 4 and Appendix A of this thesis confirmed that the simulation of moist convection at convection-resolving scales is sensitive to the employed subgrid-scale turbulence parameterization. Although there is an indication that 3D turbulence closures devised for LES are in principle applicable to convection-resolving models employing horizontal grid spacings finer than 1 km, the problem that the physical assumptions of these turbulence schemes are not valid across the wide range of scales within the grey zone of convection still remains. More research in this direction is further motivated by the incoming generation of global climate models, which include the possibility to use local grid refinement [e.g. Icosahedral Non-hydrostatic general circulation model

(ICON; Wan et al. [2013] and Laboratoire de Météorologie Dynamique general circulation model (LMDZ; Hourdin et al. [2006]). This challenges the current way turbulence is parameterize in that it will be no longer feasible to tune the schemes to certain resolutions.

• The PBL schemes tested in Chapter 4 are widely employed in operational NWP and state-of-the-art regional-climate models. A common feature is that they are constructed using the classic downgradient eddy-diffusion approach which assumes that turbulent mixing in the PBL is mainly characterized by a downgradient transport carried out by local eddies. However, in the upper mixed layer of the PBL mixing is also characterized by organized nonlocal updrafts which are directed *up* the local gradient [e.g. Hong and Pan, 1996; Zhou et al., 2018], such that more recently-developed schemes include a countergradient correction term in addition to the classic downgradient eddy-diffusion term. A potential extension of this study is to investigate the physical representation of the gradient and countergradient terms across resolutions and choice of the subgrid-scale turbulence treatment, and their association with fluxes due to local and nonlocal eddies. To do so, very high-resolution simulations at grid spacings of $\mathcal{O}(100\,\text{m})$ or even smaller may be carried out within selected subdomains.

• Although there is evidence that traditional convection parameterizations do not work well at convection-resolving scales (see Appendix A), running with explicit convection at kilometer-scale resolutions may still lead to issues such as an insufficient vertical transport from the PBL to the free troposphere due to a misrepresentation of shallow cumulus convection. More effort is needed, for instance, to incorporate the vertical transport and detrainment of condensate of shallow cumulus clouds into existing turbulence parameterizations.

A

Idealized large-eddy and convection-resolving simulations of moist convection over mountainous terrain

Davide Panosetti[1], Steven Böing[1,2], Linda Schlemmer[1], and Jürg Schmidli[1,3]

Abstract On summertime fair-weather days, thermally-driven wind systems play an important role in determining the initiation of convection and the occurrence of localized precipitation episodes over mountainous terrain. This study compares the mechanisms of convection initiation and precipitation development within a thermally-driven flow over an idealized double-ridge system in large-eddy (LES) and convection-resolving (CRM) simulations. First, LES at a horizontal grid spacing of 200 m is employed to analyze the developing circulations and associated clouds and precipitation. Second,

[1]Institute for Atmospheric and Climate Science, ETH Zurich, Universitätstrasse 16, 8092 Zurich, Switzerland

[2]School of Earth and Environment, University of Leeds, LS2 9JT, Leeds, UK

[3]Institute for Atmosphere and Climate, Goethe-University, Altenhöferallee 1, D-60438 Frankfurt am Main, Germany

CRM simulations at horizontal grid length of 1 km are conducted to evaluate the performance of a kilometer-scale model in reproducing the discussed mechanisms.

Mass convergence and a weaker inhibition over the two ridges flanking the valley combine with water vapor advection by upslope winds to initiate deep convection. In the CRM simulations, the spatial distribution of clouds and precipitation is generally well captured. However, if the mountains are high enough to force the thermally-driven flow into an elevated mixed layer, the transition to deep convection occurs faster, precipitation is generated earlier, and surface rainfall rates are higher compared to the LES. Vertical turbulent fluxes remain largely unresolved in the CRM simulations and are underestimated by the model, leading stronger upslope winds and increased horizontal moisture advection toward the mountain summits. The choice of the turbulence scheme and the employment of a shallow convection parameterization in the CRM simulations change the strength of the upslope winds, thereby influencing the simulated timing and intensity of convective precipitation.

A.1 Introduction

Moist convection is an important driver of day-to-day weather and is a major component of the water and energy cycles. It is thus essential to understand and accurately simulate it in both weather forecasting and climate prediction models. A large part of the inaccuracy of state-of-the-art numerical models in forecasting clouds and precipitation results from difficulties in simulating the triggering and the evolution of convective processes [e.g. Dai and Trenberth, 2004; Brockhaus et al., 2008]. One of the most relevant mechanisms initiating moist convection is the convergence of boundary-layer (BL) air. Therefore, a successful simulation of convection initiation also depends on a reasonable representation of BL processes [Petch et al., 2002].

Mountains of all scales can produce convergence at low levels and thus exert a strong local control on the formation of clouds and the rainfall distribution. The mechanisms leading to orographic convection and precipitation have been extensively reviewed in the literature [e.g. Banta, 1990; Houze, 1993]. Among the prominent mechanisms are thermally-driven wind systems. These wind systems determine the airmass exchange between mountainous regions and the adjacent plains and are observed on a wide range of scales, from the whole mountain range [e.g. Reiter and Tang, 1984; Lugauer and Winkler, 2005], to the scale of single valleys and slopes [e.g. Wagner, 1932]. Slope winds are an example of the latter category and are driven by horizontal density gradients generated by differential surface heating between the mountain peaks and the surrounding plains and valleys [e.g. Egger, 1990; Whiteman, 1990]. On fair-weather days, slope winds are important for the transport and mixing of heat, moisture, and other constituents over mountainous terrain [Schmidli, 2013]. Convergence of upslope winds is an important convection

initiation mechanism. Midlevel moistening associated with convective transport is narrowly focused over the mountain ridges [e.g. Orville, 1968; Banta, 1990; Damiani et al., 2008] and, if the wind is weak or absent, builds up for some time, leading to strong preconditioning and favoring the transition from shallow to deep convection [e.g. Kirshbaum, 2011]. Cloud organization [e.g. Kirshbaum and Grant, 2012] and a supportive environment are also important contributing factors.

Recent enhancements in computing capacities have increasingly allowed for the running of convection-resolving numerical models (CRMs: often referred to as convection-permitting models in the literature; see e.g. Prein et al., 2015). CRMs are mesoscale models with horizontal grid spacings of $\mathcal{O}(1\,\text{km})$. Several studies have shown that even at grid spacings as large as $4\,\text{km}$ deep convection can be successfully modeled without a convection parameterization scheme [e.g. Weisman et al., 1997; Hohenegger et al., 2008; Baldauf et al., 2011]. The use of CRMs is motivated by previous encouraging results in both numerical weather prediction (NWP) [e.g. Done et al., 2004; Lean et al., 2008; Schwartz et al., 2009] and regional-scale climate simulations [e.g. Hohenegger et al., 2008; Kendon et al., 2012; Ban et al., 2014]. CRMs also appropriately represent the bulk feedbacks between moist convection and the larger-scale flow [Langhans et al., 2012c]. However, despite large improvements in recent years, CRMs still have issues simulating both the spatial distribution and temporal evolution of precipitation [e.g. Xu et al., 2002; Bryan et al., 2003]; this can in part result from their inability to represent shallow convection and of an inappropriate treatment of subgrid-scale turbulence.

The latter problem is well explained in Wyngaard [2004]. Before computing resources allowed higher-resolution mesoscale modeling, there were two distinguished types of models: mesoscale models [$\mathcal{O}(10\,\text{km})$ mesh size], covering larger domains, and large eddy simulation models [LES; $\mathcal{O}(100\,\text{m})$ horizontal grid spacing], covering smaller domains in idealized studies. Their fundamental difference with regard to turbulence treatment is symbolized by the parameter $\alpha = l/\Delta$, where l is the energy-containing turbulence scale ($1\,\text{km}$ is a good order of magnitude for convective conditions), and Δ is the grid size. In mesoscale modeling, $\alpha << 1$ and therefore none of the turbulence can be resolved. In LES, on the other hand, the finer grid allows for explicit resolution of the largest BL eddies, and $\alpha >> 1$. Turbulence in mesoscale models is often treated by simple one-dimensional (1D) turbulence schemes, which assume that the net effect of turbulence consists in a mostly vertical downgradient flux. In LES, three-dimensional (3D) subgrid-scale models are employed to account for the horizontal fluxes as well. However, in CRMs the model resolution is roughly equal to the characteristic turbulence scales of convective structures ($\alpha \sim 1$; Craig and Dörnbrack, 2008), and thus neither LES nor 1D turbulence schemes are strictly applicable. This is why this range of scales is called "terra incognita" [Wyngaard, 2004].

Numerical simulations in the terra incognita do not only have issues with

turbulence treatment, but it is also questionable whether a shallow convection scheme should be employed. Most of the convection parameterization schemes employed in CRMs have in fact been devised for global climate models [e.g. Tiedtke, 1989; Kain and Fritsch, 1990], and are thus based on assumptions that are often violated at such horizontal grid spacings. Furthermore, in CRMs the model grid size is roughly equal to or even larger than the typical horizontal size of shallow clouds. Therefore a shallow convection parameterization might still be necessary to capture sufficient moisture transport from the boundary layer into the mid-troposphere.

In mountainous terrain, many problems with regard to turbulence and shallow convection parameterization in CRMs are accentuated. Most turbulence parameterization schemes assume horizontally homogeneous conditions and have been validated against observational data over flat terrain [e.g. Mellor and Yamada, 1982; Rotach and Zardi, 2007]. This also affects the performance of the convection parameterization scheme, in which the triggering and the closure often depend on turbulent processes in the subcloud layer [e.g. Kirshbaum, 2011].

LES at horizontal mesh spacing of $\mathcal{O}(100\,\mathrm{m})$ is needed to explicitly resolve most of the underlying turbulent processes, and can be used to address some of the CRM's deficiencies. Previous LES studies of orographic convection have focused on single hills or ridges [e.g. Kirshbaum, 2011; Kirshbaum and Grant, 2012] where, in the absence of a background flow, there is a strong preferential location for convective initiation over the mountain summit. A few recent idealized studies [e.g. Serafin and Zardi, 2010; Schmidli and Rotunno, 2010; Schmidli, 2013; Wagner et al., 2014] have examined the more complex case of a double mountain ridge, where the differential heating mechanisms between the valley atmosphere and the surroundings are crucial to determine where convective cells form. However, these studies only consider a dry atmosphere, and thus do not account for any effect related to condensation, cloud cover, deep convection and precipitation.

In this study, an analysis of the important processes for the initiation and subsequent development of moist convection and precipitation within a thermally-driven flow is performed using LES modeling over idealized mountain ridges. A primary focus is on the role of moisture transport by the upslope winds and of vertical mixing. CRM simulations are also run to investigate the performance of a coarser-resolution model in reproducing the discussed mechanisms. In the CRM simulations, different turbulence schemes and a shallow convection parameterization are tested to understand if an optimal configuration exists to better match the LES results.

The numerical model and the experimental design are presented in Section A.2. In Section A.3, the methodology used to compute the water vapor budget and the subgrid-scale vertical fluxes of zonal momentum is described. In Section A.4, the processes leading to convection initiation and precipitation development over a double mountain ridge are investigated using LES. Sec-

tion A.5 compares the LES with CRM simulations. In the CRM simulations, different turbulence schemes and a shallow convection parameterization are tested to understand if an optimal configuration exists to better match the LES results. The summary and conclusions are given in Section A.6.

A.2 Model description

A.2.1 Model

For this study we use version 5.0 of the Consortium for Small-Scale Modeling (COSMO) model [Baldauf et al., 2011]. The COSMO model is a non-hydrostatic, fully compressible limited-area atmospheric prediction model, designed for both operational high-resolution NWP and research applications on a broad range of spatial scales, from the meso-γ (horizontal scales between 2 and 20 km) to the meso-β (horizontal scales between 20 and 200 km). The model is used in different configurations for operational NWP purposes at several European weather services, and has been further developed into a regional climate modeling system [Rockel et al., 2008].

We conduct simulations at horizontal grid spacings of 200 m (hereafter referred to as COSMO-LES) and 1 km (COSMO-1). The time integration is performed with a third-order Runge-Kutta scheme [Klemp and Wilhelmson, 1978; Wicker and Skamarock, 2002]. A fifth-order advection scheme is used for temperature, pressure, and horizontal and vertical winds, and a second-order scheme [Bott, 1989] is employed for horizontal advection of moist quantities. The parameterizations include a radiative transfer scheme based on the δ-two-stream approach [Ritter and Geleyn, 1992], in which radiation interacts with both subgrid and grid-scale clouds, and a single-moment bulk microphysics scheme with three ice categories (ice, snow, graupel) after Reinhardt and Seifert [2006].

Subgrid-scale turbulent mixing in COSMO-LES is parameterized by a 3D Smagorinsky-Lilly closure [Langhans et al., 2012d]. COSMO-1 employs a 1D (vertical) turbulent scheme after Raschendorfer [2001]. It is a 1.5-order scheme based on a prognostic equation for turbulent kinetic energy (TKE) with a level 2.5 closure, following Mellor and Yamada [1974]. The different turbulence schemes tested for COSMO-1 during sensitivity studies are as follows: the 3D Smagorinsky-Lilly turbulence closure, a hybrid 1D/2D scheme that uses a Smagorinsky-Lilly closure in the horizontal and the 1D scheme in the vertical, and another 3D turbulence closure designed for LES [Deardorff, 1973; Herzog et al., 2002]. The latter utilizes a prognostic equation for subfilter-scale TKE. The tested convection parameterization is the Tiedke mass-flux scheme with moisture-convergence closure [Tiedtke, 1989]. The scheme distinguishes between shallow (restricted to a maximum depth of 250 hPa from the cloud base to the cloud top), midlevel and deep convection. In the sensitivity studies for COSMO-1, only the shallow convection part of the scheme is turned on.

The atmospheric part of the system is coupled to the second-generation, 10-layer land surface model TERRA_ML [Heise et al., 2003] which provides values of surface temperature and specific humidity. A Louis surface transfer scheme [Louis, 1979] is used to calculate the transfer coefficients that yield the surface sensible and latent heat fluxes based on Monin-Obukhov similarity theory.

A.2.2 Setup

The model domain covers $380 \times 60\,\mathrm{km}^2$. The horizontal grid spacing is $200\,\mathrm{m}$ in COSMO-LES and $1\,\mathrm{km}$ in COSMO-1, resulting in 1900×300 and 380×60 grid points in the horizontal respectively. A generalized smooth level vertical (SLEVE) coordinate is used [Schär et al., 2002; Leuenberger et al., 2010]. The vertical domain extends up to $21.5\,\mathrm{km}$. COSMO-LES uses 177 vertical levels, and the grid spacing increases from $10\,\mathrm{m}$ at the lowest level to a maximum of $400\,\mathrm{m}$ at $21.5\,\mathrm{km}$. COSMO-1 has 81 vertical levels, with vertical grid length varying from $20\,\mathrm{m}$ near the surface to $800\,\mathrm{m}$ above $18\,\mathrm{km}$. The soil layer thickness varies from $2\,\mathrm{cm}$ to $5.76\,\mathrm{m}$, and the soil total depth is $11.50\,\mathrm{m}$. Soil parameters and plant characteristics are prescribed using equilibrated values from simulations of diurnal convection in a mid-European climate [Schlemmer et al., 2011]. The time step is $2\,\mathrm{s}$ in COSMO-LES and $10\,\mathrm{s}$ in COSMO-1. The 3D fields are written to output every 6 min. The lateral boundary conditions are periodic in both horizontal directions. At the upper domain boundary a rigid lid is employed, and a Rayleigh damping layer extends from $11.5\,\mathrm{km}$ to the top of the domain to minimize spurious reflections of gravity waves. The Coriolis force is set to zero. To break the symmetry of the initial fields, the potential temperature is disturbed at the lowest model level with random perturbations of $\pm 0.02\,\mathrm{K}$. Incoming solar radiation is uniformly distributed on the entire domain and is determined for $48.25°\mathrm{N}$, $0°\mathrm{E}$ (which is comparable to the Black Forest region in Central Europe) on 12 July 2006 following Schlemmer et al. [2011].

The case is based upon the setup introduced by Kirshbaum [2011], who constructed it from data retrieved during an intensive observational period (IOP 8b) from the Convective and Orographically Induced Precipitation Study (COPS) [Wulfmeyer et al., 2011]. The initial temperature and moisture profiles are idealized from a COPS sounding that was launched at 0800 UTC [1000 local time (LT)] upstream of the southern Black Forest using a four-layer temperature profile and a three-layer humidity profile (see Fig. 1 in Kirshbaum, 2011). The resulting initial flow is characterized by a stable layer up to $1\,\mathrm{km}$, an elevated mixed layer (ML) between $1\,\mathrm{km}$ and $3\,\mathrm{km}$, a pseudoadiabatic layer up to $12.5\,\mathrm{km}$, and a stable stratosphere. This makes the environment convectively inhibited (CIN $\approx 310\,\mathrm{J\,kg^{-1}}$) and conditionally unstable, which are commonly observed features in Europe during summertime. The simulations start at 0600 LT and end at 2000 LT to capture the full diurnal cycle. To test the sensitivity to the background wind, we use a

Expt	Δx	*Orography*	*Configuration*
LESf	200 m	none	3Dsmag
LESs5	200 m	single 500 m	3Dsmag
LESd5	200 m	double 500 m	3Dsmag
LESd15	200 m	double 1500 m	3Dsmag
CRMd5	1 km	double 500 m	1D, 1Dsh, hyb, 3Dsmag, 3Ddear
CRMd15	1 km	double 1500 m	1D, 1Dsh, hyb, 3Dsmag, 3Ddear

Table A.1: List of experiments and different configurations.

Configuration	*Turb. scheme*	*Shall. conv. scheme*
1D	1D vertical + hor. diff.	off
1Dsh	1D vertical + hor. diff.	on
hyb	1D vertical + 2D Smag hor.	off
3Dsmag	3D Smag	off
3Ddear	3D Deardorff	off

Table A.2: List of different CRM configurations.

hyperbolic tangent profile for horizontal wind near the surface defined by:

$$u(z) = u_{max} \, tanh(z/H) \tag{A.1}$$

where u is the horizontal wind speed, $u_{max} = 1.5$ or $3 \, \mathrm{m \, s^{-1}}$, z is the altitude (m) and $H = 2000 \, \mathrm{m}$ is a length scale. Two-dimensional topography, corresponding to two infinite ridges and an infinite valley in the y-direction, is used. This provides more robust statistics by averaging in the y-direction, when necessary. The mountain profile used in this study is described in Schmidli et al. [2011]. Two different valley depths of 500 m and 1.5 km respectively are employed, and the sloping sidewall width is set to 45 km. This leads to a crest-to-crest distance of 90 km. These numbers are chosen such that the idealized ridges roughly represent the dimensions of the Vosges-Black Forest mountain system. Furthermore, using a smooth terrain in both the CRM and LES minimizes the differences in their topographic representations. To allow for free development of the mountain-plain circulation without any interference from the model boundaries, the model domain is centered on the valley floor, and thus the flat terrain surrounding the mountain sector extends for 100 km away from the foothills. The simulations and the different configurations are listed in Table A.1 and Table A.2. In the sensitivity studies in Section A.5, we have repeated each simulation three times for the CRM simulations and twice for the LES, using different initial random temperature perturbations at the lowest model level to check for robustness of the results with respect to the turbulent fluctuations. Differences between

the simulations were generally small, although there were some cases where the convection was slightly stronger over the western or eastern mountain in individual LES simulations. We use the mean of these simulations [denoted by asterisks (*)] in the discussion of several figures.

A.3 Methodology

A.3.1 The water vapor budget

The processes contributing to the instantaneous local moistening and drying of the BL atmosphere are given by:

$$\frac{\partial q_v}{\partial t} = -\mathbf{v} \cdot \nabla q_v - \frac{1}{\rho l_v}(\nabla \cdot \mathbf{L}) + S_m \tag{A.2}$$

where q_v is the specific water vapor, $\mathbf{v}$ the wind speed vector, ρ is the air density, l_v is the latent heat of vaporization, $\mathbf{L} = \rho l_v \overline{\mathbf{v}' q_v'}$ is the subgrid-scale latent heat flux, and S_m are microphysical source/sink rates (primarily condensation and evaporation of rain). The overbar denotes a time mean. The primes indicate subgrid-scale variables. All the terms in Eq. A.2 are extracted using the moisture budget tool implemented in COSMO [Langhans et al., 2012b].

To compute the net effect of each process on a small control volume V of total mass M in the subcloud layer at the mountain top, Eq. A.2 is integrated over V. The volume-averaged density-weighted water vapor budget equation is:

$$\underbrace{\frac{1}{M}\int_V \rho \frac{\partial q_v}{\partial t} dV}_{\text{TOT}} = \underbrace{\frac{1}{M}\int_V -\rho \mathbf{v} \cdot \nabla q_v \, dV}_{\text{ADV}} + \underbrace{\frac{1}{M}\int_V -\frac{1}{l_v}(\nabla \cdot \mathbf{L}) dV}_{\text{UNRES}}$$

$$+ \underbrace{\frac{1}{M}\int_V \rho S_m \, dV}_{\text{MIC}} \tag{A.3}$$

where TOT is the water vapor storage tendency, ADV is the water vapor advection, UNRES is the subgrid-scale latent heat flux convergence, and MIC is the microphysics contribution.

The total ADV can be further split into a horizontal (HADV) and vertical (ZADV) component:

$$\underbrace{-\frac{1}{M}\int_V \rho \mathbf{v} \cdot \nabla q_v \, dV}_{\text{ADV}} = \underbrace{-\frac{1}{M}\int_V \rho v_{hn} \cdot \nabla q_v \, dV}_{\text{HADV}}$$

$$\underbrace{-\frac{1}{M}\int_V \rho w \cdot \nabla q_v \, dV}_{\text{ZADV}} \tag{A.4}$$

where v_{hn} is the horizontal velocity component normal to the sidewalls (positive for inward-directed flow, negative for outward-directed flow), and w is the vertical velocity. In Sections A.4.1 and A.4.2 the control volume is located over the western ridge summit (arbitrarily chosen over the eastern one, given the symmetry of the model domain), is $10\,\text{km}$ wide in the x-direction, and extends vertically from the surface up to the cloud base. Since the analysis in Sections A.4.1 and A.4.2 is limited to the time period that precedes the onset of precipitation, the contribution of microphysical processes is neglected. In Section A.4.4 the control volumes are located over the foothills east and west of the mountain sector, are $30\,\text{km}$ wide in the x-direction, and extend vertically from the surface up to the BL top.

A.3.2 The subgrid-scale vertical fluxes of zonal momentum

In the CRM simulations, the subgrid-scale fluxes are computed by a 1D (vertical) turbulence scheme (see Section A.2.1). If one defines τ_{uw} to be the subgrid-scale vertical component of the zonal turbulent momentum flux tensor (a similar parameterization applies to the meridional turbulent momentum flux tensor τ_{vw}), in the boundary layer approximation, it is parameterized as:

$$\tau_{uw} = -\rho K_m^V \frac{\partial u}{\partial z} \tag{A.5}$$

where K_m^V is the vertical diffusion coefficient or eddy viscosity, ρ is the air density, and u is the horizontal wind speed. The quantity K_m^V is determined using the Prandtl-Kolmogorov specification as:

$$K_m^V = \phi_m \Lambda \sqrt{2e} \tag{A.6}$$

The characteristic Blackadar length scale l_v for vertical mixing is calculated according to Blackadar [1962]:

$$l = \frac{kz}{1 + (kz)/l_\infty} \tag{A.7}$$

where k is the von-Karman constant, and $l_\infty = 200\,\text{m}$ is an asymptotic length scale. ϕ_m is a stability-dependent coefficient, and $\overline{e} = \overline{(u_i' u_i')}/2$, with $i = 1, 2, 3$, is the subgrid-scale TKE per unit mass.

When run in LES mode, COSMO treats vertical and horizontal eddy viscosities with a 3D Smagorinsky-Lilly mixing-length turbulence model. For momentum fluxes, the residual stress-tensor is defined as:

$$\tau_{ij} = -2K_m D_{ij} \tag{A.8}$$

$$D_{ij} = \frac{1}{2}\left(\frac{\partial U_i}{\partial x_j} + \frac{\partial U_j}{\partial x_i}\right) \tag{A.9}$$

where D_{ij} is the grid-scale rate of strain. Here, isotropy is assumed. The eddy viscosity includes the effect of buoyancy and is given by:

$$K_m = (c_s l_s)^2 \overline{D} \sqrt{max(0, 1 - \frac{Ri}{Ri_c})} \qquad (A.10)$$

with the characteristic filtered rate of strain $\overline{D} = (2D_{ij}D_{ij})^{1/2}$ and the Smagorinsky length scale l_s given by Deardoff's proposal as $l_s = (\Delta x \Delta y \Delta z)^{1/3}$. The Smagorinsky constant c_s in this study is set to 0.25. Ri_c is the critical Richardson number and Ri the deformation Richardson number, which is a function of moist static stability (see Langhans et al., 2012c).

A.4 Large eddy simulations

A.4.1 Flow evolution and structure

To document the spatial distribution and time evolution of clouds and surface precipitation under the presence or abscence of mountains, three LES runs are compared: one with flat terrain only (LESf), one with an isolated single ridge (LESs5) and one with an isolated double ridge (LESd5). We begin by examining the case in which the mountain summits are at 500 m altitude, and thus within the surface stable layer (see Section A.2.2), and in which the background wind is absent.

The top panels in Fig. A.1 are Hovmöller diagrams illustrating the onset time and spatial distribution of updraft velocities and clouds. The bottom panels in Fig. A.1 show the surface rain-rate and the ice water path. The amount of cloud ice (at high levels) is an indicator of the presence of deep convective cells.

In LESf the cloud liquid water path is very homogeneous and a strong response of convection to the diurnal cycle of incoming solar radiation is observed: this starts with the development of a dry convective boundary layer, which is followed by shallow cumulus convection. The strongly inhibited environment (see Section A.2.2) prevents the transition from shallow to deep convection, and no precipitation is produced throughout the whole simulation. In LESs5 shallow clouds are initiated in the morning at the mountain ridge summit by upslope wind convergence. Convective precipitation is generated just before noon. Over the surrounding plains convection exhibits a diurnal cycle similar to the one in Fig. A.1a for LESf except at the mountain ridge foot, where it is more intense and it lasts until the late afternoon. In LESd5 we observe similar features as in LESs5 at both mountain ridges, with convection and precipitation peaking at the summits. The deep convective events are less strong than the one in LESs5, as indicated by the smaller cloud ice content. Shallow clouds form over the valley in the afternoon, in response to relatively strong updraft motion.
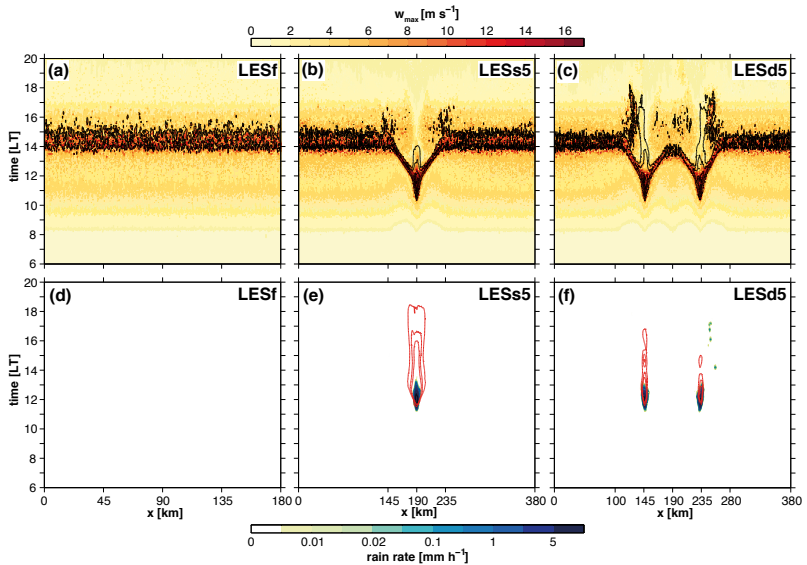
Figure A.1: (a-c) Hovmöller diagrams of maximum vertical velocity in the y-z plane (w_{max} [m s^{-1}], color scale) and y-averaged cloud liquid water path (black contours: 0.01, 0.1, 0.5 1 2 and 3 g kg^{-1}) for (a) LESf, (b) LESs5 and (c) LESd5. (d-f) Hovmöller diagrams of y-averaged surface rain rate (color scale) and cloud ice water path (red contours: 0.01, 0.02 and 0.03 g kg^{-1}) for (d) LESf, (e) LESs5 and (f) LESd5. In LESs5 and LESd5, the x-axis tick labels highlight the domain boundaries and the mountain sector: the mountain summits are located at x = 190 km in LESs5 and at x = 145 km and x = 235 km in LESd5.

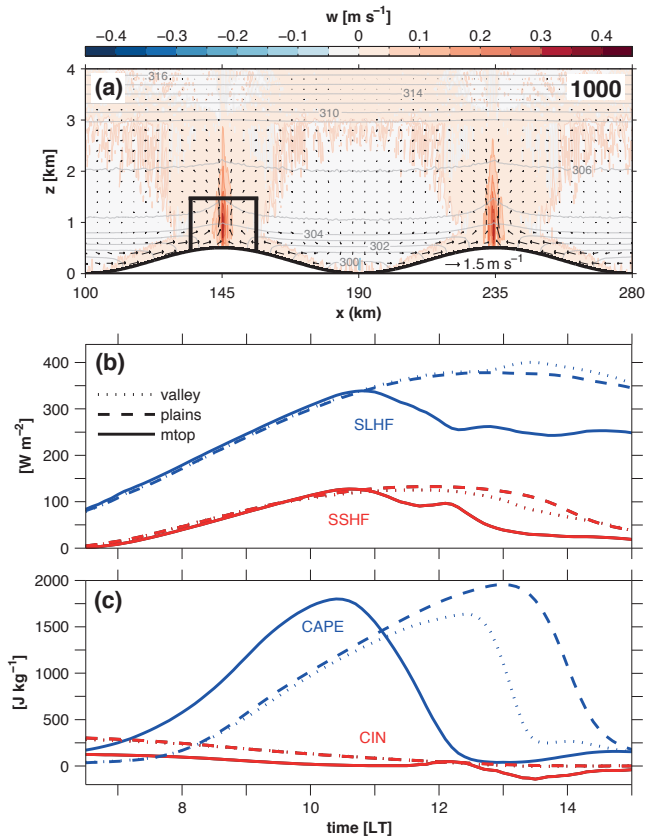**Figure A.2:** (a) Hourly mean y-averaged wind speed (black vectors: reference vector of 1.5 m s⁻¹), potential temperature ([K], grey lines) and vertical velocity (color scale) centered at 1000 LT in LESd5. The black box over the western mountain ridge displays the control volume used to compute the water vapor budget in Fig A.3a. (b) and (c) Time evolution of y-averaged (b) SSHF (red lines) and SLHF (blue lines) and (c) CAPE (blue lines) and CIN (red lines) over the western mountain ridge (mtop, solid lines), over the valley center (dotted lines) and over the plains at x = 50 km (dashed lines).

Figure A.2a illustrates the mean developing circulation over the mountain sector in LESd5. The circulation is driven by differential heating between the mountain summits and the surrounding air and is symmetric about the valley, owing to the lack of background wind. As in the simulations of Schmidli and Rotunno [2012] and Schmidli [2013], which did not include moist convection, the flow consists of weak mountain-to-plain and mountain-to-valley winds aloft and plain-to-mountain and valley-to-mountain winds below. Flow convergence over the mountains and subsidence over the valley and over the foothills are also observed. Despite the presence of the mountains, the surface sensible (SSHF) and latent (SLHF) heat fluxes vary only slightly in the x-direction (Fig. A.1b); a significant reduction in both SSHF and SLHF is observed over the mountain summit only after the precipitation event. However, there is a considerable variation in both convective inhibition (CIN) and convective available potential energy (CAPE) in the x-direction (Fig. A.2c): CIN is lower, but CAPE is higher and builds up more efficiently over the mountain summit compared to over the surrounding terrain.

To quantify the respective contribution of the advective and unresolved terms in the water vapor budget equation (Eq. A.3) to the moistening of a control volume in the subcloud layer over the western mountain summit (see Section A.3.1 for a detailed description of the budget; the control volume considered is depicted in Fig. A.2a), the time evolution of averaged specific water vapor tendencies within the control volume is shown in Fig. A.3a. Until 1030 LT a net moistening of the control volume is observed. The major contribution comes from the horizontal advection, whereas a minor contribution is given by the unresolved fluxes, which mainly consist of surface latent heat flux and entrainment drying. Vertical advection is the only loss term: it represents vertical transport of moisture from the BL into the midlevel troposphere, as well as resolved entrainment of dry air from the free troposphere into the subcloud layer. A sharp decrease in the horizontal advection contribution, which soon becomes a loss term, follows the onset of deep moist convection and precipitation.

Figure A.3b shows the horizontal distribution of liquid water path (blue line, left axis) and relative humidity at $z = 1500$ m (red line, right axis) at 1100 LT in LESd5. At the onset time of precipitation, the atmosphere above the mountain ridges has an excess of $5 \, \mathrm{kg \, m^{-2}}$ of moisture compared to the surrounding plains and the valley, and relative humidity in the convective core exceeds that of the surrounding air by 25%.

A.4.2 Mountain top embedded in an elevated mixed layer

Figures A.4a and A.4b show the temporal and spatial distribution of updraft velocities, clouds and precipitation in LESd15. By raising the mountain height to 1500 m, the summit breaks through the lower stable layer and is embedded within the elevated ML (see Section A.2.2). By comparing the
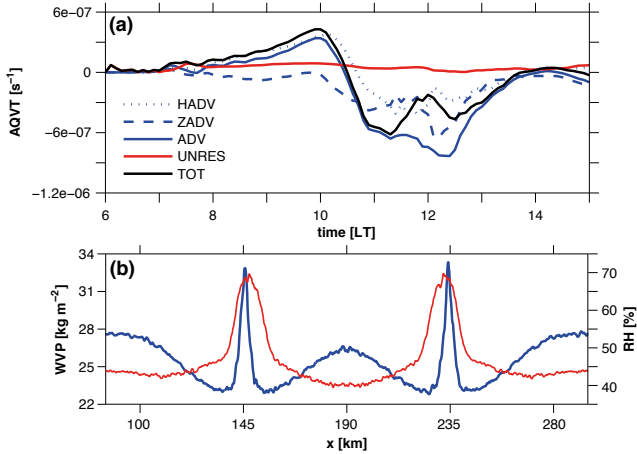
Figure A.3: (a) Time evolution of volume-averaged density-weighted water vapor tendencies in the control volume displayed in Fig. A.2a. TOT (black line) is the storage tendency, HADV (dotted blue line) is the horizontal advection, ZADV (dashed blue line) is the vertical advection, ADV (solid blue line) is the total advection, and UNRES (red line) is the subgrid-scale latent heat flux convergence. (b) Horizontal distribution of y-averaged water vapor path (WVP, blue lines) and relative humidity at $z = 1500\,\mathrm{m}$ (RH [%], red line) at 1100 LT in LESd5.
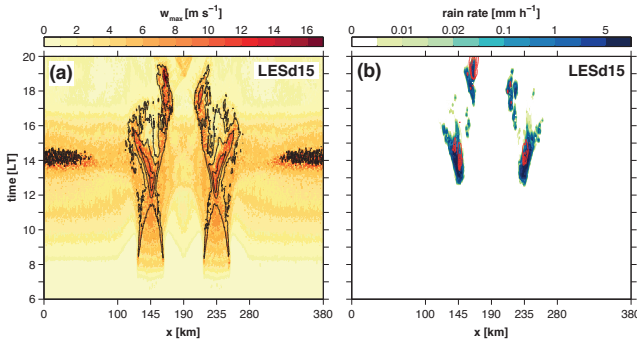

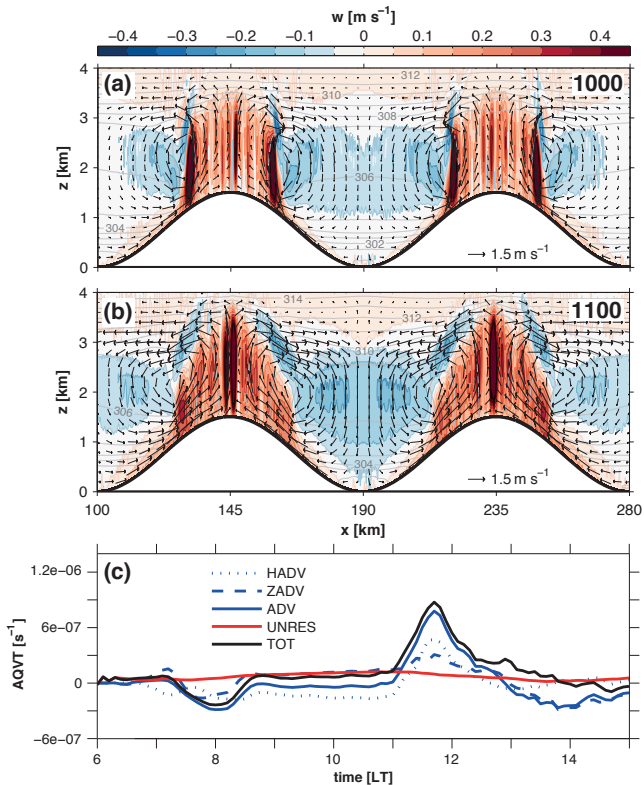**Figure A.4:** (a) and (b) As Figs. A.1c and A.1f but for LESd15.

Figure A.5: (a) and (b) Hourly mean y-averaged wind speed (black vectors: reference vector of $1.5 \, \text{m s}^{-1}$), potential temperature ([K], grey lines) and vertical velocity (color scale) centered at (a) 1000 LT and (b) 1100 LT in LESd15. (c) As Fig. A.3a but for LESd15.

flow structure and evolution in Figs. A.4a A.4b with the one in Figs. A.1c A.1f important differences both before and after the first precipitation event over the mountain ridge summit are visible. First, updraft velocity peaks at the mountain slopes in the morning, and shallow clouds form there rather than at the summit. Second, in LESd15 convection moves toward the valley center in the afternoon, and two distinct secondary precipitation events can be seen over the valley sidewalls.

Figures A.5a and A.5b illustrate the evolution of the mean cross-ridge circulation over the mountain sector in LESd15 in the morning hours. In contrast to LESd5, the convective core at the summit is not isolated but rather located within a larger area of strong convection. In addition, vigorous convective cells are visible over the slopes. Within the elevated ML a neutrally-stratified

environment allows for vigorous BL turbulence. Convergence of mountain-to-valley winds at $z = 3$ km increases the subsidence between $z = 1$ and 3 km over the valley compared to over the plains. Both CIN and CAPE over the mountain summits are considerably lower compared to LESd5 (not shown), with the former being approximately zero throughout the whole simulation and the latter being roughly 100 J kg^{-1} (cf. Fig. A.2c) at the time of the first precipitation event.

Figure A.5c shows the time evolution of averaged specific water vapor tendencies in a control volume in the subcloud layer at the western mountain summit in LESd15. The dimensions of the control volume considered are exactly as in LESd5 (see Fig. A.2a and Section A.3.1). In the morning, surface latent heating and vertical advection balance the negative contribution of horizontal advection (with the flow initially being downslope and toward the updrafts over the slopes; not shown). The observed peak in horizontal advection is delayed by roughly 2.5 hours compared to LESd5. A large fraction of the moisture carried by upslope winds is removed vertically by the strong thermals over the mountain slopes once it enters the elevated ML, and is therefore prevented from reaching the mountain top as in LESd5. This vertical transport of moisture leads to the formation of shallow cumuli over the mountain slopes, as illustrated in Fig. A.4a, and can partially explain the delayed onset of deep convection compared to LESd5 observed in Figs. A.4a and A.4b. The reduced CAPE and the drier environment at the summit are also contributing factors. Note also that the peak in horizontal advection is much sharper compared to LESd5. This is explained by the convergence at the summit of the two convective cores over the slopes (see Fig. A.5b).

A.4.3 Deep precipitating convection over the valley sidewalls

Differential heating processes between the valley atmosphere and the adjacent plains result in stronger upslope winds blowing from the plains compared to those blowing from the valley (Figs. A.5a and A.5b). The larger heating rate of the valley atmosphere can be explained from a bulk perspective in terms of the so called "valley-volume effect" [e.g. Wagner, 1932]: a given amount of energy input applied to a valley heats a smaller volume and therefore a smaller mass of air compared to over flat terrain. Stronger subsidence over the valley compared to over the plains (see Figs. A.5a and A.5b) also contributes to explain the larger heating rate of the valley atmosphere. Figure A.6a compares the time evolution of air temperature at a height of 1600 m in LESd15 at three different locations: over the valley center, over the eastern mountain summit, and over the open plains. The air over the mountain summit warms up faster than the surrounding air, triggering upslope winds at both mountain ridge slopes. However, the valley atmosphere heats up at a faster rate than the air above the plains, leading to a smaller temperature gradient, and thus weaker upslope winds blowing from the plains compared to those blowing from the valley. This difference is important in determining
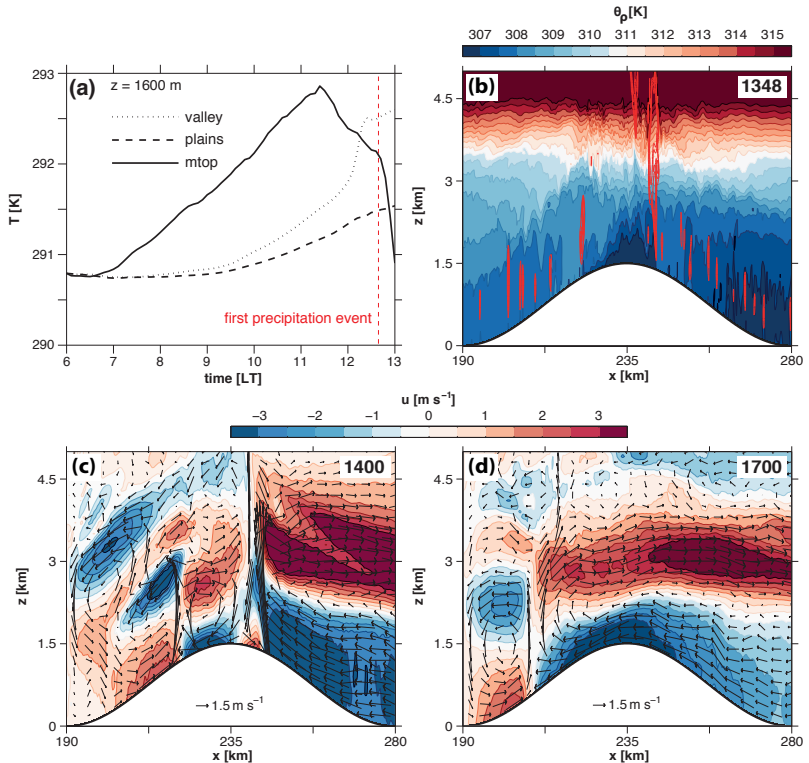
Figure A.6: (a) Time evolution of y-averaged air temperature at $1600\,\text{m}$ altitude above the valley (dotted line), above the eastern mountain ridge (solid line) and above the plains at $x = 280\,\text{km}$ (dashed line) in LESd15. The red line indicates the time of the first precipitation event over the eastern mountain ridge summit. (b) Vertical cross section at $y = 0\,\text{km}$ of density potential temperature (θ_ρ [K], color scale) and updraft velocity (red contours: 2, 2.5, 3 and $3.5\,\text{m s}^{-1}$) after the first precipitation event over the eastern mountain ridge summit. (c) and (d) Vertical cross sections of y-averaged horizontal velocity (color scale) and wind speed (black vectors: reference vector of $1.5\,\text{m s}^{-1}$) (c) after the first precipitation event and (d) before the second precipitation event over the easter mountain ridge summit in LESd15.

the flow evolution after the first precipitation event over the mountain summit.

Cooling by evaporation of precipitation below convective clouds results in cold pools, which are characterized by a near-surface horizontal flow of relatively cold and dry air. A few studies [e.g. Grabowski et al., 2006; Khairoutdinov and Randall, 2006; Böing et al., 2012; Bao and Zhang, 2013; Schlemmer and Hohenegger, 2014] investigated how precipitation-driven cold pools aid the transition from shallow to deep convection. Vertical lifting and moisture accumulation at the leading edge of the cold pool play an important role. Kirshbaum and Grant [2012] remarked the importance of this feedback in studies of orographic convection.

Figure A.6b displays the density potential temperature θ_ρ and updraft velocity after the first precipitation event over the eastern ridge in LESd15; θ_ρ is defined as:

$$\theta_\rho \equiv T_\rho (\frac{p_0}{p})^{\frac{R_d}{c_{pd}}} \tag{A.11}$$

where T_ρ is the density temperature, p_0 is a standard reference pressure of 1000 hPa, p is the pressure, R_d is the gas constant for dry air, and c_{pd} is the heat capacity of dry air at constant pressure. Following Emanuel [1994], the density temperature is defined as:

$$T_\rho \equiv T \frac{1 + r/\epsilon}{1 + r_T} \tag{A.12}$$

where r is the water vapor mixing ratio, $\epsilon = R_d/R_v$ is the ratio between the gas constant for dry air and for water vapor, and $r_T = r + r_l + r_i$ is the net water mixing ratio, which includes ice and liquid water. The value T_ρ may thus be either greater than or less than the actual temperature T depending on the relative amounts of condensed water and water vapor. The cold pools are visible as the region of low θ_ρ at the mountain summit in Fig. A.6b. Forced lifting along the leading edges of the downslope-travelling cold pools is highlighted by the red contours at x = 220 and 245 km.

Figs. A.6c and A.6d illustrate the flow evolution over the eastern mountain ridge between the first precipitation event over the summit and the second precipitation event over the valley sidewall. Stronger low-level convergence is observed after the first precipitation event over the mountain slope toward the plains compared to over the valley sidewall (cf. the upward motion at x = 220 km and at x = 245 km in Figs. A.6b and A.6c). However, the flow field becomes rapidly dominated by upslope winds again toward the plains, whereas over the valley sidewall the weaker upslope winds allow the cold pool to travel downslope (see Fig. A.6d). Stronger updrafts are driven by wind convergence at the leading edge of the cold pool when it collides with the upslope flow and generate the secondary precipitation event.
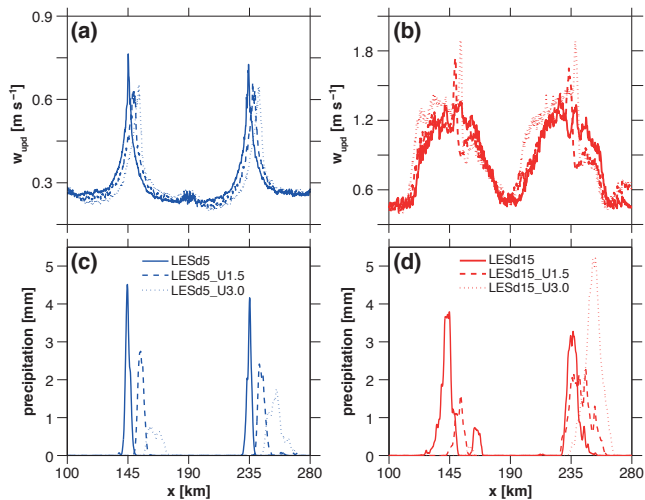
Figure A.7: (a) and (b) Hourly mean updraft velocities w_{upd} averaged in the y-direction and over the first kilometer above the mountain summits centered (a) at 1100 LT in LESd5 (solid line) and (b) at 1500 LT in LESd15 (solid line) with increasing background wind: _U1.5 (dashed line) and _U3.0 (dotted line). (c) and (d) As (a) and (b) but for the y-averaged accumulated surface precipitation over the entire duration of the simulation.

A.4.4 The role of background wind in convection initiation

The background wind speed U_b not only controls the strength of the mass convergence over the mountain top [e.g. Crook and Tucker, 2005; Kirshbaum, 2011], but also the moisture distribution within the mountain sector. Given the importance of this parameter, its influence on the simulated cloud and precipitation fields is investigated. The strength of the background wind (see Section A.2.2) is gradually increased in LESd5 and LESd15.

Figures A.7a and A.7c illustrate the strength and location of the thermally-induced updrafts over the mountain summits in the morning and the spatial distribution of accumulated precipitation over the mountain sector in LESd5 with increasing background winds. The updrafts are stronger and develop at the summit without background wind. As the background wind increases, the updrafts weaken and form farther down the downwind slope. The weaker convective cores generate less intense rainfall in LESd5_U1.5 and LESd5_U3.0. In contrast in LESd15, in which the mountains are higher and generate stronger circulations compared to LESd5, the updrafts over the mountain summits strengthen with increasing background wind (Fig. A.7b), and the spatial distribution of precipitation over the downwind mountain ridge exhibits a different pattern than the one observed in Fig. A.7c and over

the upwind mountain ridge (Fig. A.7d). As U_b increases, precipitation in LESd15 decreases upwind but increases downwind of the valley.

Figure A.8a illustrates the specific water vapor and wind velocity fields at 1200 LT in LESd15_U3.0. The background wind has been removed here to better illustrate the circulations associated with the convective cores over the mountain slopes. The convective circulations perturb the basic pressure state and ultimately drive changes in the low-level flow. Figure A.8b compares the surface pressure gradient between the plains and the foothills (solid lines, left axis) and the low-level horizontal wind speed (dashed lines, right axis) upwind and downwind of the mountain sector. The convective core at $x = 240$ km is located over the mountain slope on the lee side of the mountain sector; the associated upward motion generates a low surface pressure perturbation over the foothills, and a high surface pressure perturbation over the open plains, as a result of compensating subsidence. This strengthens the surface pressure gradient on the lee side of the mountain sector, which ultimately leads to a stronger low-level flow towards the mountains. Note that a stronger low-level flow is also observed upwind of the valley compared to downwind of the valley and is generated by the same mechanisms discussed above. This explains the strengthening of the updrafts at both mountain summits observed in Fig. A.7b.

An asymmetric spatial distribution similar to the one illustrated in Fig. A.7d for the accumulated precipitation in LESd15 is observed in Fig. A.8a in the water vapor field and can be explained by the combined effects of the compensating subsidence associated with the convective circulation and the strengthening of the low-level flow toward the mountains on the lee side. Figures A.8c and A.8d compare the water vapor tendencies in two control volumes within the BL over the foothills (see the black boxes in Fig. A.8a), one upwind (Fig. A.8c) and one downwind (Fig. A.8d) of the mountain sector. Before the onset of precipitation, a balance between a net positive contribution from horizontal advection and the negative contribution from vertical advection is observed in both control volumes. However, after 1130 LT, a decrease in export due to vertical advection and an increase in import due to horizontal advection are observed in the control volume downwind of the mountains. This is the combined effect of the compensating subsidence from the circulation associated with the convective core over the mountain slopes and the strengthening of the low-level flow toward the mountain foothills, which not only carries BL moisture from the open plains, but also disturbs the development of diurnal BL convection over the foothills. This extra availability of water vapor on the lee side explains the observed spatial distribution of convection and precipitation. Note that when the accumulated water vapor is transported over the mountain summit, CAPE also increases from the low values observed in LESd15 up to roughly $600 \, \mathrm{J \, kg^{-1}}$ (not shown).
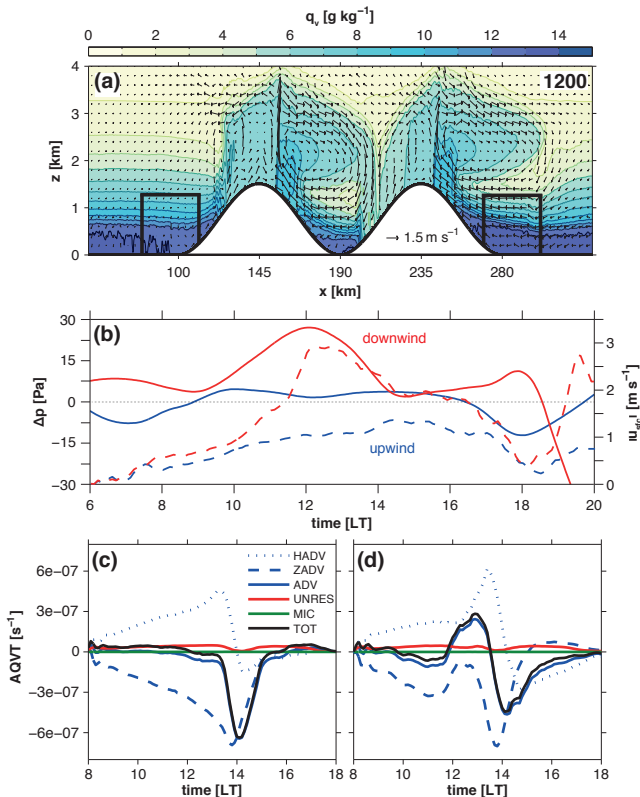
Figure A.8: (a) Vertical cross-section at $y = 0$ km of specific water vapor (q_v [g kg^{-1}], color scale) and cross-ridge wind speed (black vectors: reference vector of 4 m s^{-1}) at 1200 LT in LESd15_U3.0. The black boxes over the foothills downwind and upwind of the mountain sector display the control volumes used to compute the water vapor budget in (c) and (d). (b) Time evolution of y-averaged pressure gradient between the plains (40 km away from the foothills) and the foothills (solid lines, left vertical axis) and absolute horizontal wind speed at a height of 20 m ($| u |_{sfc}$ [m s^{-1}], dashed lines, right vertical axis) upwind (blue lines) and downwind (red lines) of the mountain sector. (c) and (d) Time evolution of y-averaged water vapor tendencies in the (c) upwind and (d) downwind control volume depicted in (a).

A.5   Convection-resolving simulations

The simulations discussed in Section A.4 are repeated with a CRM setup using a horizontal grid spacing of 1 km to investigate the performance of a coarser-resolution model in reproducing the spatial and temporal evolution of convection and precipitation. Figures A.9a-d illustrate the evolution of convection and precipitation in CRMd5 (Figs. A.9a and A.9c) and CRMd15 (Figs. A.9b and A.9d). The most important physical processes described in Section A.4 are captured: the first precipitation events at the mountain top, the downslope-travelling cold pools and the secondary precipitation events over the valley sidewalls in LESd15. Nevertheless, the absence of shallow cumuli in the morning over the slopes and an earlier triggering of convective precipitation are observed in CRMd15. In particular, the first precipitation event at the mountain top occurs one hour earlier, and the secondary precipitation event over the valley sidewalls three hours earlier.

Figures A.9e and A.9f show the time evolution of averaged specific water vapor tendencies in CRMd5 and CRMd15 in the same control volume in the subcloud layer over the western mountain summit used in the analysis in Section A.4. Although there are only minor differences comparing CRMd5 with LESd5, in CRMd15 an earlier, sharper and stronger (roughly twice as large) horizontal water vapor advection toward the mountain summit compared to LESd15 is observed (cf. Fig. A.3 for LESd5 and Fig. A.5c for LESd15).

Figures A.10a and A.10b compare vertical velocity, potential temperature and mean cross-ridge wind speed over the western slope of the western mountain ridge at 1030 LT in LESd15 and CRMd15. Instantaneous values of vertical velocity are shown to illustrate the BL thermals. In CRMd15, a distinct updraft is observed at the mountain summit. In LESd15, the BL thermals are explicitly resolved, and a transition between less intense convection over the mountain slopes and more vigorous convection over the mountain top, where the upslope winds converge, is observed. The enhanced vertical motion within the elevated ML seen in LESd15 is only partially observable in the coarser-resolution simulation. Also, the resolved mixing at the BL top seen in LESd15 is absent in CRMd15.

Vertical turbulent transport by BL thermals removes some of the water vapor but also momentum from the upslope flow. The turbulent (resolved + unresolved: see Section A.3.2 for the computation of the unresolved fluxes) vertical fluxes of zonal momentum at $x = 135$ km (within the elevated ML) and at a height of 20 m in LESd15 and CRMd15 are compared in Fig. A.10c. The resolved turbulent fluxes are calculated offline as deviations from the mean thermally-driven circulation. The total (resolved + unresolved: solid lines) fluxes are larger in LESd15 than in CRMd15, which suggests a stronger vertical transport of momentum in the higher-resolution runs. Figure A.10d compares the evolution of the horizontal wind speed at the same location where the vertical turbulent fluxes of momentum are computed in the morning in LESd15 and CRMd15. Weaker vertical transport within the elevated
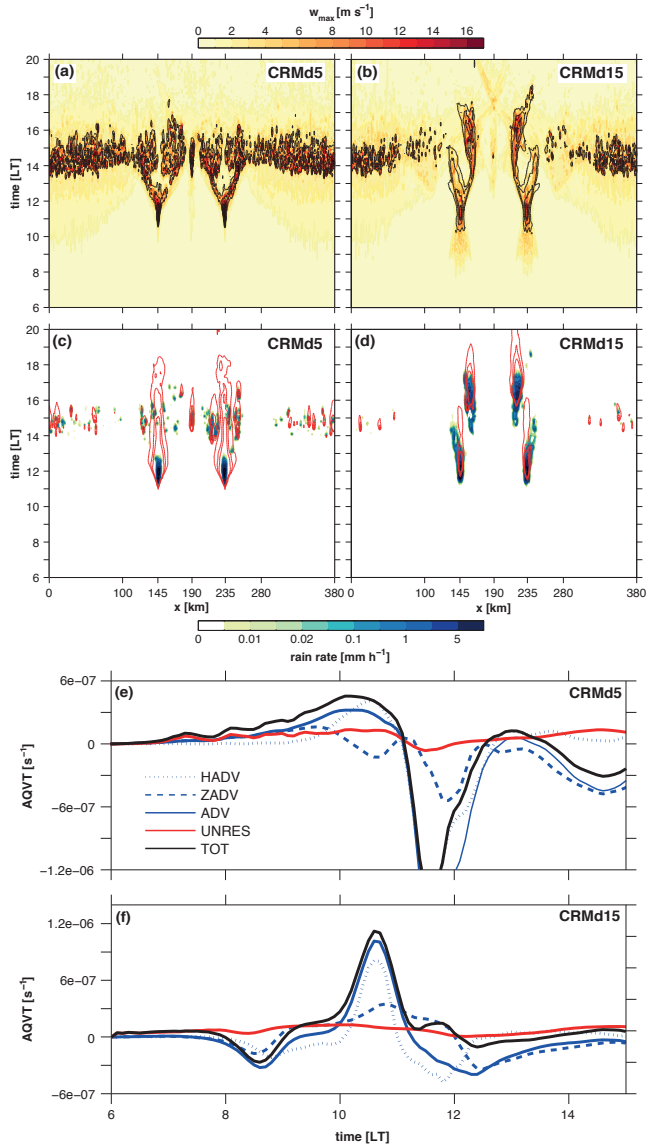
Figure A.9: (a-d) As Figs. A.1c and A.1f but for (a) and (c) CRMd5 and (b) and (d) CRMd15. (e) and (f) As Fig. A.3a but for (e) CRMd5 and (f) CRMd15.
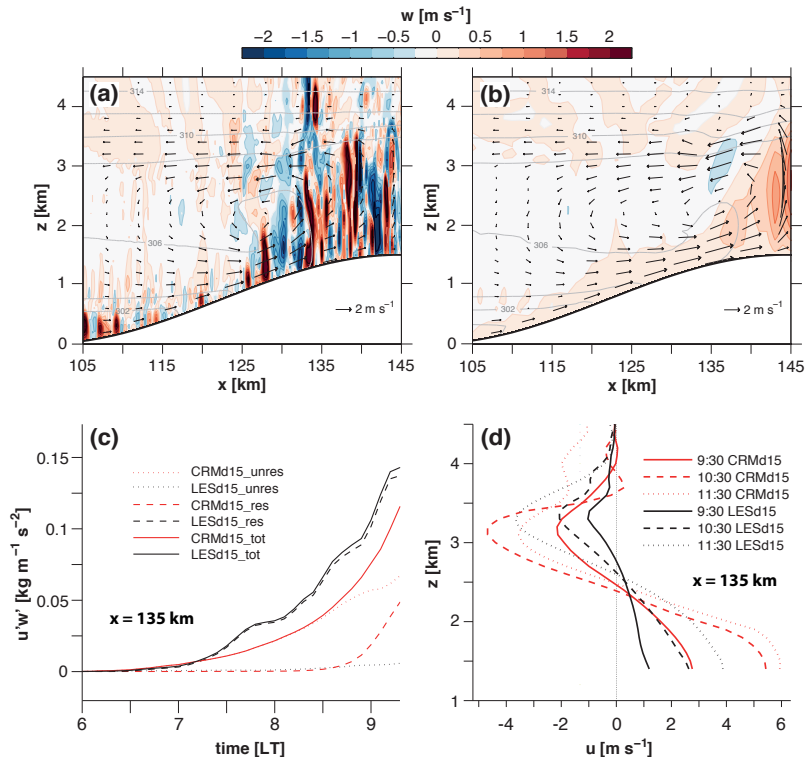
Figure A.10: (a) and (b) Vertical cross sections of instantaneous vertical velocity (color scale) at 1030 LT and hourly mean y-averaged wind speed (black vectors: reference vector of $2\,\mathrm{m\,s^{-1}}$) and potential temperature ([K], grey contours) centered at 1030 LT in (a) LESd15 and (b) CRMd15. (c) Time evolution of y-averaged vertical turbulent fluxes of momentum in LESd15 (black lines) and CRMd15 (red lines) at $x = 135\,\mathrm{km}$ and at a height of $20\,\mathrm{m}$. The legend discriminates between unresolved (dotted lines), resolved (dashed lines) and total (resolved + unresolved) fluxes. (d) Hourly mean vertical profiles of y-averaged horizontal wind speed centered at 0930 LT (solid lines), 1030 LT (dashed lines) and 1130 LT (dotted lines) in LESd15 (black lines) and CRMd15 (red lines) at $x = 135\,\mathrm{km}$.

ML in CRMd15 leads to stronger horizontal wind velocities compared to the LES. This not only strengthens mass convergence over the mountain summit, but also explains the stronger horizontal water vapor advection observed in Fig. A.9f. Reduced lateral turbulent entrainment in rising thermals as a result of the coarser resolution (not shown) could have also contributed to more vigorous convection in CRMd15. Recently, Hohenegger et al. [2015] also found a faster transition in coarser-resolution simulations, but in contrast they observed a delayed development of convection for the sea-breeze system studied.

A.5.1 Sensitivity to the turbulence and shallow convection parameterization

The sensitivity of precipitation and horizontal wind velocity in the CRM simulations to different turbulence parameterizations and to the employment of a shallow convection scheme is investigated.

The top panels in Fig. A.11 compare the time evolution of the domain-averaged surface rain rate in d5, d15 and d15_U3.0, which include both the LES and CRM experiments. The middle panels in Fig. A.11 show the spatial distribution of the accumulated precipitation at the surface during the entire duration of the simulations. The differences are small between CRMd5 and LESd5, in which vertical motion is limited within the shallow boundary layer, but there are big differences between CRMd15 and LESd15, in which convection is enhanced within the elevated ML.

The spatial distribution of precipitation is strongly controlled by the orography and is almost independent of the choice of the turbulence parameterization scheme. In contrast, the onset timing of precipitation differs by up to several hours. 3D schemes systematically delay the onset of convective precipitation in the CRM simulations. The differences are generally small between 1D* and hyb*, but larger differences are found when comparing these two schemes with 3Dsmag* and 3Ddear*, and also between 3Dsmag* and 3Ddear* themselves, suggesting that the choice of the horizontal mixing formulation may not account for the main differences between 1D and 3D schemes. In LESd5 and CRMd5, where the mountain slopes are less steep and the circulations develop mainly in the horizontal, there is stronger resemblance between the LES and the CRM simulations employing a 1D turbulence scheme as compared to CRM simulations employing a 3D scheme. A 3D turbulence scheme seems more suitable in CRMd15 and in CRMd15_U3.0, in which the onset timing of precipitation is strongly influenced by vertical transport processes by the BL eddies.

The bottom panels in Fig. A.11 compare vertical profiles of horizontal wind speed over the mountain slopes at 1030 LT. The differences between the simulations are marginal in d5 and d15_U3.0. In d15, in the CRM simulations employing a 3D turbulence scheme the upslope winds are weaker compared to CRM simulations employing a 1D turbulence scheme, suggesting an in-
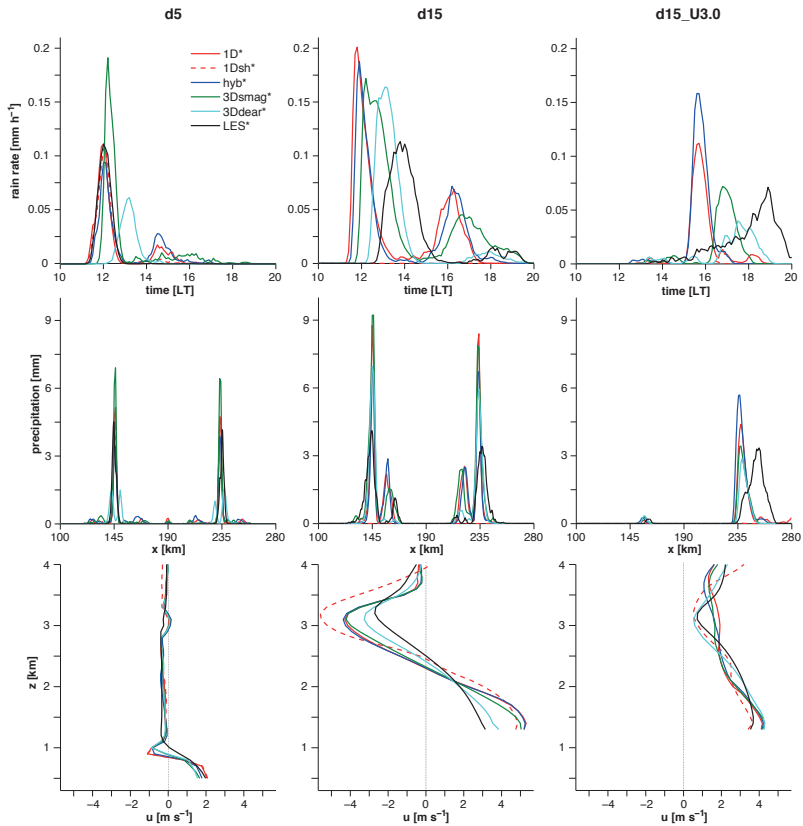
Figure A.11: (top) Time evolution of ensemble and domain-averaged surface rain rate in (left to right) d5, d15 and d15_U3.0. (middle) As in (top), but for the ensemble and y-averaged accumulated surface precipitation over the entire duration of the simulation. (bottom) As in (top) but for the running hourly mean vertical profiles of ensemble and y-averaged horizontal wind speed at $x = 135\,\mathrm{km}$ centered at 1030 LT.
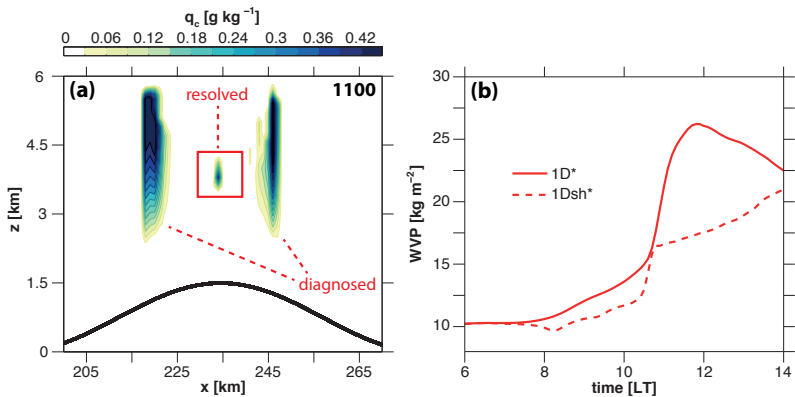
Figure A.12: (a) Vertical cross section of y-averaged specific cloud liquid water content (q_c [g kg^{-1}], color scale) at 1100 LT over the eastern mountain ridge in an ensemble member of 1Dsh. The red labels point at the parts of the cloud field that are explicitly resolved and diagnosed by the shallow convection scheme. (b) Time evolution of the y-averaged water vapor path over the eastern mountain ridge summit in 1D* (solid line) and 1Dsh* (dashed line).

creased vertical mixing. This could explain the delayed onset of precipitation observed in the panel above.

The employment of a shallow convection scheme (1Dsh*) does not modify substantially the simulated flow evolution in CRMd5 but has a big impact in CRMd15 and CRMd15_U3.0, in which precipitation is almost absent. The thick clouds visible over the slopes and diagnosed by the scheme in Fig. A.12a are absent in the LES (cf. Fig. A.4a for LESd15). In Fig. A.12b, which shows the time evolution of water vapor path above the mountain summit, a less pronounced moistening of the mountain summit is observed in the morning hours in 1Dsh* compared to 1D*. The scheme thus seems to exhibit a strong sensitivity to grid-scale moisture convergence in the subcloud layer. The authors observed a partial improvement, at least in the representation of the cloud field, changing the mass-flux closure to a surface buoyancy flux-based one (not shown).

A.6 Summary and conclusions

The important mechanisms of moist convection initiation and precipitation development within thermally-driven wind systems over mountainous terrain are investigated in idealized large-eddy (LES) and convection-resolving (CRM) simulations over an idealized double-ridge system with an embedded valley. For this study the model of the Consortium for Small-scale Modeling (COSMO) is run at horizontal grid spacings of 200 m and 1 km. The simu-

lations are based on the setup introduced by Kirshbaum [2011]. The strong convective inhibition, the presence of an elevated mixed layer (ML) and the conditional instability of the flow make it a useful case study to gain insight into orographic controls on cloud formation and the triggering of precipitation.

First, the mechanisms are analyzed by means of LES. Mass convergence, a more efficient buildup of CAPE and a weaker inhibition over the mountains flanking the valley combine with water vapor advection by upslope winds to initiate deep convection. Over higher mountains, whose summits protrude above the early morning lower stable layer and into the elevated ML, the transition to deep, precipitating convection is delayed compared to simulations with lower mountains, although convection inhibition is reduced. The delayed precipitation is mainly associated with increased vertical mixing within the elevated ML, which delays water vapor advection toward the mountain summits by upslope winds. A drier environment and a reduced CAPE over the mountain summits also contribute to explain the delayed precipitation. In the afternoon, secondary precipitation events are observed over the valley slopes. Differential heating processes between the valley atmosphere and the adjacent plains result in stronger upslope winds blowing from the plains compared to those blowing from the valley. This results in a preferential propagation of precipitation-driven cold pools at the summits toward the valley center. A strengthening of low-level convergence over the valley sidewalls is observed when the downslope-travelling cold pools collide with the upslope winds, which triggers the observed deep, precipitating convection.

The presence of background wind moves the convective cores over the slopes downwind of the summits, weakens convective updraft strength and reduces the amount of accumulated precipitation in the simulations with lower mountains. However, in the simulations with higher mountains the updraft strengthens with increasing background wind, and an asymmetric spatial distribution of precipitation is observed, with lower precipitation over the upwind ridge and higher precipitation over the downwind ridge and on the lee side of the mountain sector for stronger ambient winds. The perturbation induced in the pressure field by the downwind shift of the convective cores strengthens the updrafts downwind of the mountain summits, and in particular the low-level flow on the lee side, which transports moisture from the plains toward the mountains. This causes a massive moisture accumulation and a preferential location for the onset of deep moist convection over the downwind ridge and on the lee side of the mountain sector.

In the second part of the study CRM simulations are run and compared to the LES to investigate the performance of a coarser-resolution model in reproducing the mechanisms described above. Both the total precipitation amount and its spatial distribution simulated in the LES are well captured in CRM simulations with low mountains, in which vertical motion in the morn-

ing is limited within the shallow surface ML, and the circulations develop mainly in the horizontal. When the mountains are sufficiently high to enter the elevated ML, a faster triggering of deep convection and an earlier onset of precipitation are observed in the CRMs. The CRMs have a too coarse grid spacing to resolve the boundary layer eddies simulated in the LES, which remove some of the moisture and horizontal momentum from the upslope flow by vertical turbulent transport, and tend to underestimate the unresolved fluxes. This results in stronger upslope winds and stronger horizontal water vapor advection toward the mountain summit in the CRM simulations, which ultimately explain the faster and sharper transition from shallow to deep convection, and the earlier development of precipitation compared to the LES.

Several CRM ensembles employing different turbulence parameterization schemes are also compared. The turbulence parameterization scheme is found to have a minor influence on the spatial distribution of precipitation. However, there are differences in the onset time of convective precipitation and in the simulated surface rain rate compared to the LES. In particular, the employment of a 3D turbulence parameterization scheme is observed to systematically lead to weaker upslope winds, suggesting increased vertical mixing and delaying the onset of convective precipitation. The sensitivity studies also suggest that the different behaviors between the turbulence schemes might be due to differences in the vertical mixing formulation, rather than in the horizontal. The employment of a shallow convection scheme delays and dramatically reduces the precipitation when the mountain summit is located within the elevated ML. This is due to an excessive vertical moisture transport at the mountain slopes compared to the LES and other CRM simulations in which the shallow convection scheme is not active.

To conclude, the case setup chosen allowed for analyzing particular interactions and feedbacks that led to important differences between the LES and the CRMs. The choice of a double mountain ridge was made to capture features of real orographic systems, such as differential heating processes between the valley and the surrounding plains. The full treatment of moist convection and of cloud-radiation feedbacks represented a step forward toward a more complete analysis with respect to previous similar studies. Also, the consideration of land-atmosphere interactions allowed for a more realistic representation of feedbacks between clouds and surface fluxes compared to other studies which used prescribed surface fluxes.

Further research is necessary to confirm the relative importance of the convection initiation and precipitation development mechanisms described in this study. In this study, the presence and depth of the elevated ML certainly had an impact on the simulated amount of precipitation. The analysis in the presence of a background wind can be further improved by considering 3D topography with finite ridges to allow for other important effects, such as lee-side convergence, that were not considered in this study. Small-scale

topographical variations can also affect the orographic flow evolution due to channelling effects or strong local convergence at isolated small-scale peaks [e.g. Kirshbaum et al., 2007; Fuhrer and Schär, 2007], and lead to further issues concerning turbulence parameterization [Rotach and Zardi, 2007].

B

The influence of the resolution of topography and surface fields on the simulation of orographic moist convection

Christopher Heim[1], **Davide Panosetti**[1], Linda Schlemmer[1], and Christoph Schär[1]

Abstract Orographic moist convection tends to develop when and where moist instability coincides with sufficient terrain-induced ascent to locally overcome convective inhibition. This study aims at analyzing how the degree of detail in the representation of topography and surface fields influences the simulation of orographic moist convection. 9 days (11-19 July 2006) of thermally-driven flow over the Alps are analyzed. Two sets of simulations are compared, each consisting of 3 runs at horizontal grid spacings of 4.4, 2.2, and 1.1 km: one with fixed and one with varying resolution of topography and surface fields.

---

[1]Institute for Atmospheric and Climate Science, ETH Zurich, Universitätsstrasse 16, 8092 Zurich, Switzerland

Results show that with higher degree of detail of topography and surface fields the thermally-driven mesoscale flow over the Alps (Alpine pumping) is enhanced. Convection is triggered later, its maximum intensity is reduced and lasts for a longer time. The longer duration compensates for the reduced intensity such that total accumulated precipitation at the surface increases. This additional precipitation is mostly generated by secondary convective cells over the Po Valley and the Southern edge of the Alpine arc. The single convective cells are weaker and smaller, but their number increases.

Overall, these findings suggest that substantial changes in the simulation of orographic moist convection occur when the resolution of topography and surface fields is increased, and highlights that high-resolution datasets are important for accurate weather forecasts and climate projections.

B.1 Introduction

Moist convection is an important mechanism in the atmosphere that controls the vertical distribution of heat and water vapor. Its net effect is to transport relatively warm and often moist air from lower to higher levels of the atmosphere and relatively cold and dry air in the opposite direction. Convective clouds are a manifestation of moist convection and are often accompanied by precipitation.

Several processes may lead to the formation of precipitating convective cells. For instance, they can be triggered by frontal ascent, by upper-level destabilization, or by convergence of air in the planetary boundary layer (PBL). During fair-weather days, shallow cumulus clouds form at the top of the PBL in response to the incoming shortwave radiation which warms the ground and causes thermals to rise. These shallow cumuli usually experience a transition to deep convection before they produce a significant amount of rain.

There are several mechanisms that may hinder or favor the transition from shallow to deep convection. For instance, rising moist adiabatic air parcels lose buoyancy through the dilution from clear-air entrainment [e.g. Kirshbaum, 2011]. Besides that, radiative cooling reduces the buoyancy of the relatively warm updrafts. Processes favoring the transition to deep convection include mesoscale ascent by enhancing the uplifting of air parcels, cloud organization by reducing clear-air entrainment [e.g. Kirshbaum and Grant, 2012], and convergence of precipitation-driven cold pools [e.g. Grabowski et al., 2006; Böing et al., 2012; Schlemmer and Hohenegger, 2014].

Over mountainous terrain, one additional mechanism which may trigger deep convective cells are thermally-driven wind systems [Banta, 1990]. Thermally-driven wind systems form on fair-weather days and consist of mesoscale mountain-plain winds and local valley and slope winds [e.g. Wagner, 1932; Egger, 1990]. The mesoscale mountain-plain wind systems are driven by differential heating between the air over the mountains and the air over the surrounding plains. This creates a thermal low over the mountains during the
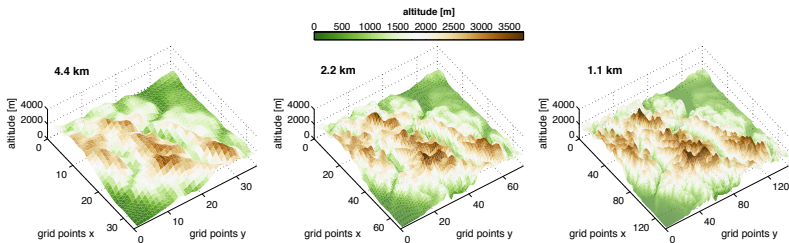
Figure B.1: Discretized topography in a $160 \times 160\,\mathrm{km}^2$ region of the European Alps at $\Delta x = 4.4$, 2.2 and 1.1 km. Courtesy of Davide Panosetti.

day and a thermal high over the mountains during the night. The mountain-plain winds evolve accordingly. During the day, the valley and slope winds transport the air coming in from the plains up the mountain valleys and slopes. Eventually, this leads to convergence of PBL air and moisture over the mountain summits. The convergence of air locally generates updrafts and the moisture supply from the surrounding plains and valleys favors the initiation of deep convection [e.g. Kirshbaum, 2011; Panosetti et al., 2016]. Because of these wind systems, mountainous regions like the European Alps exhibit an increased fair-weather convective activity compared to the surrounding plains. In the European Alps, the mesoscale circulation between the plains and the Alpine region is called "Alpine pumping" [Lugauer and Winkler, 2005; Langhans et al., 2013] and it is characterized by a daytime inflow layer with a depth of up to more than 2000 m and a much shallower nocturnal outflow layer with a depth of about 500 m [Corsmeier et al., 2003; Weissmann et al., 2005]. The horizontal inflow during the day is linked to an enhanced convective activity over the Alpine region. Convection exports the laterally imported surplus of moisture and heat in the vertical direction out of the boundary layer. During the night, on the other hand, convection is inhibited over the Alps due to the thermally-generated high pressure system and the associated subsidence.

Recent enhancements in computing power have allowed for the widespread use of convection-resolving models (CRMs) that can be run at horizontal resolutions of $\mathcal{O}(1\,\mathrm{km})$ without the need for a convection parameterization [e.g. Prein et al., 2015]. Several studies have demonstrated the added value of explicitly resolved convection for the simulation of precipitation in climate simulations [e.g. Kendon et al., 2014; Ban et al., 2014; Leutwyler et al., 2016]. CRMs also yield low resolution sensitivity with respect to the bulk feedbakcs between convection and the large-scale [e.g. Langhans et al., 2012c; Harvey et al., 2017; Panosetti et al., 2018]. Additionally, CRMs benefit from a more detailed representation of topography and surface fields. For accurate weather forecasts and climate prediction, topographic and land-use data

are important input elements for numerical models, and high-resolution terrain data are required to represent the complexity of various regions [e.g. Taylor et al., 2002; Dahai, 2004; Kabat et al., 2004]. Figure B.1 shows three-dimensional plots of the orography for a subsection of the European Alps interpolated at horizontal grid spacings (Δx) of 4.4, 2.2 and 1.1 km. Not only the degree of detail varies with resolution but also the maximum elevation in the domain differs by several hundred meters between the coarsest and the finest discretization. Because orographic convection is forced by the surface, substantial changes in the simulation of orographic convection may be expected. Several studies have already reported significant sensitivities in idealized and real-case simulations due to the resolution of small-scale topographical features or soil data [e.g. Kirshbaum et al., 2007; Stoll and Porté-Agel, 2009; Schmidli et al., 2011; Rihani et al., 2015; Obermann-Hellhund and Ahrens, 2018]. The aim of this study is to gain a deeper understanding of the influence of the degree of detail in the topography and surface fields on the simulation of orographic moist convection. The following two research questions are addressed:

1. How does the degree of detail in the topography and surface fields affect the processes driving orographic moist convection and the resulting features of orographic moist convection (onset time, intensity and duration, as well as accumulated surface precipitation)?

2. Do small-scale variations of topography and surface fields impose visible scales in the prognostic fields (vertical velocity, moist variables)? If so, what is the relative importance of these 'external scales' compared to the scale imposed by the horizontal grid spacing?

In the following section, the model and the simulations, as well as the methods used for the analysis of the simulations are presented. The results of the study are shown and analyzed in Section B.3. The discussion and conclusions are given in Section B.4.

B.2 Methods

B.2.1 Model

The simulations are run with the model of the Consortium for Small-Scale Modelling (COSMO) version 5.0 [Baldauf et al., 2011]. The COSMO model is a fully compressible, non-hydrostatic limited area model suitable for weather forecasts and climate simulations. A rotated latitude-longitude grid is used in the horizontal directions. The vertical direction is represented by a stretched terrain-following coordinate. Radiation is parameterized by the δ-two-stream approach after Ritter and Geleyn [1992]. Cloud microphysics is represented by a single-moment bulk scheme after Reinhardt and Seifert [2006]. Subgrid turbulence is parameterized with a 1D TKE-based model after Raschendorfer

[2001] in the vertical, whereas in the horizontal the eddy viscosities are computed using a Smagorinsky-Lilly closure. Because all simulations are run at convection-resolving resolution, no convection parameterization is employed.

B.2.2 Experimental Setup

The model is run at $\Delta x = 4.4$, 2.2 and 1.1 km. The vertical grid consists of 60 levels with a spacing ranging from around 20 m at the surface to around 1.2 km at the top. The model top is located at an altitude of around 23.5 km. Rayleigh damping is applied above 11.5 km to minimize the reflection of gravity waves.

The simulations are initialized and driven by a model with $\Delta x = 12$ km which is run over continental Europe (see e.g. Ban et al., 2014). The driving model has the same physical parameterizations as the nested models, except a difference subgrid-scale turbulence scheme and parameterized convection. ERA-Interim reanalysis data [Dee et al., 2011] yield the initial and lateral boundary conditions for the atmospheric part of the driving simulation. To make sure that the soil moisture and the atmosphere are well equilibrated at the start of the simulations, the soil moisture profiles are not taken from the comparably coarse ERA-Interim reanalysis data set. Instead, equilibrated soil moisture profiles from a 10-year long ERA-Interim-driven COSMO climate simulation [Ban et al., 2014] are employed. With this approach, the soil and the atmosphere should be well equilibrated by the start of the integration period in July. A relaxation zone of 35 km is located at the domain boundaries of the nested simulations. An ideal time period to study orographic moist convection over the Alpine region are the 9 days between 11 and 20 July 2006. This period has already been analyzed in previous studies (see e.g. Langhans et al., 2012c or Panosetti et al., 2019 for the same days or e.g. Langhans et al., 2013 for the entire month of July 2006). The period is characterized by the presence of a high-pressure system over the Alps with relatively low synoptic forcing and a strong diurnal cycle of convection.

The simulation domain covers an area of $1153 \times 1082\,\text{km}^2$ (Fig. B.2) and it is centered over the European Alps. The analysis focused on the Alpine region and is performed for the subdomain illustrated by the black rectangle in Fig. B.2. To determine the influence of the resolution of topography and surface fields on the convective activity, two sets of simulations (rows in Fig. B.3) are conducted. Each set consists of three simulations (columns in Fig. B.3) at $\Delta x = 4.4$, 2.2 and 1.1 km. In the first group (upper row - in the following referred to as SM, for smooth), the topography and the surface fields are kept constant with resolution. In the second group (lower row - in the following referred to as RAW), the topography and the surface fields are interpolated to the model grid at each Δx. In the following the simulations will be referred to as e.g. RAW1.1 ($\Delta x = 1.1$ km RAW simulation) or SM2.2 ($\Delta x = 2.2$ km SM simulation). Note that the topography/surface fields of the RAW4.4 and SM4.4 differ slightly in the degree of detail. This is illustrated
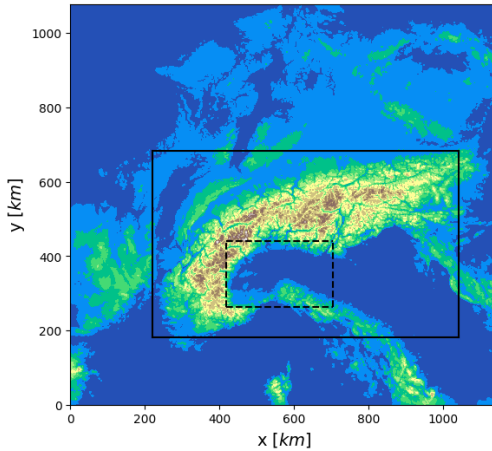
Figure B.2: Topography within the model domain at a $\Delta x = 1.1$ km. The analysis domain (Alpine region) is shown by the solid rectangle. The analysis subdomain (Po Valley) is shown by the dashed rectangle.
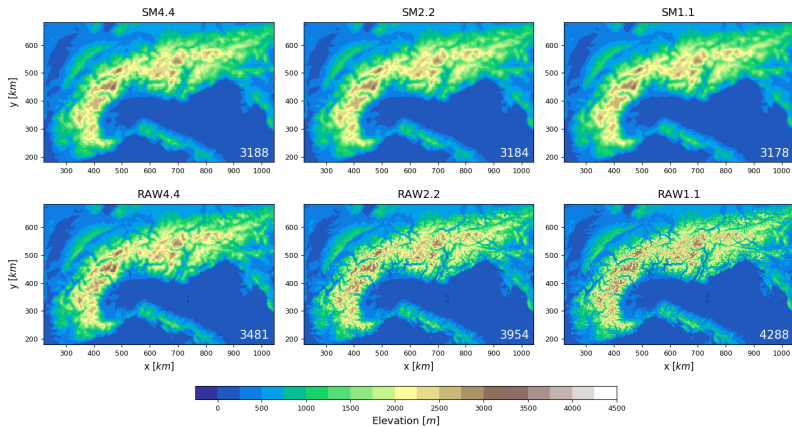
Figure B.3: Representation of topography within the analysis domain (Alpine region) in each of the 6 model simulations. The simulations consist of 2 sets called SM and RAW in the upper and the lower row, respectively. Each sets consists of 3 simulations at $\Delta x = 4.4$, 2.2 and 1.1 km, represented by the three columns. The labels in the lower right corner indicate the maximum elevation within the analysis domain.

Figure B.4: Mean diurnal cycle of domain-average rain rate [mm h^{-1}] over the Alpine region. The results of the SM and the RAW simulations are shown in the left and right plots, respectively. The model resolutions are 4.4 (black), 2.2 (blue) and 1.1 (red) km. The labels indicate the mean diurnal precipitation sum.
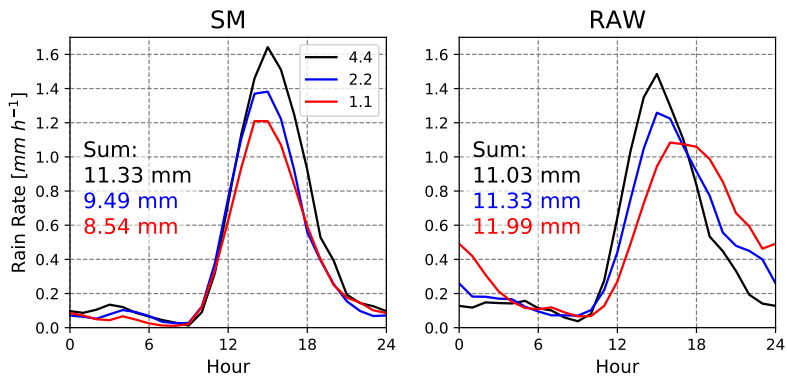
by the labels in Fig. B.3, showing the maximum surface elevation within the Alpine region. The interpolation from SM4.4 to SM2.2/SM1.1 is performed in physical space which introduces new differences in spectral space between the SM4.4 and the SM2.2/SM1.1 simulations. The additional use of a cosine filter in all SM simulations removes these differences and ensures that all of them have an identical effective resolution. Consequently, the SM4.4 simulation is not identical to the RAW4.4 simulation.

By comparing the simulation output of the SM and RAW groups, it is possible to isolate the effect of the resolution of topography and surface fields on the simulation of orographic moist convection.

B.3 Results

This section presents and discusses the most important differences between RAW and SM. In the following, all figures showing the mean diurnal cycle of a quantity are based on the average over the 9 simulated days.

B.3.1 Surface Precipitation

Mean Diurnal Cycle

Figure B.4 compares the mean diurnal cycle of domain-average precipitation between RAW and SM. A slightly earlier onset and an earlier and less intense maximum of precipitation are observed in SM with higher resolution. The precipitation sum is reduced by about 10% with a doubling of the resolution.
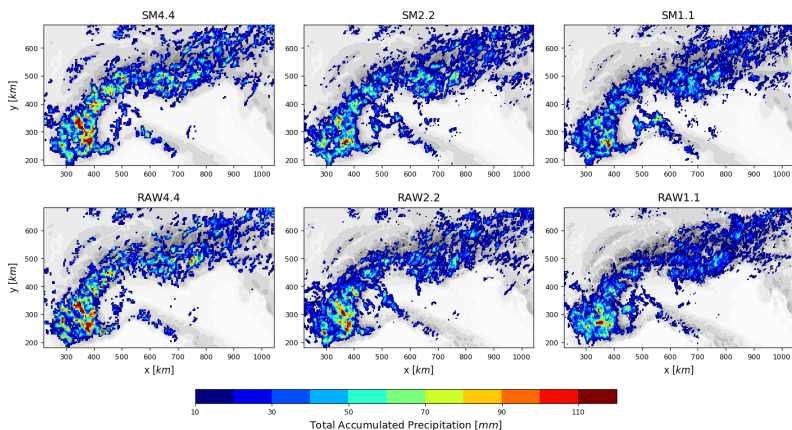
Figure B.5: Total accumulated daytime (between 8 LT and 20 LT) precipitation [mm] during the 9 simulated days. The results of the SM and the RAW simulations are shown in the upper and the lower panels, respectively. The columns show the simulations of each group with decreasing Δx from 4.4 km (left) to 1.1 km (right).

In contrast to SM, the simulations with high resolution (2.2 and 1.1 km) in RAW show a very different behaviour: both the onset time and diurnal peak are delayed, the maximum intensity is reduced, and precipitation does not end at 22 LT, as in the RAW4.4 and the SM simulations. Instead, there is a substantial amount of night-time precipitation that continues until 1 LT. and 4 LT in RAW2.2 and RAW1.1, respectively. The longer duration in these simulations overcompensates for the reduced intensity with higher resolution, such that the precipitation sum increases with higher resolution in RAW.

Spatial Pattern

Figure B.5 and B.6 show the total daytime and nighttime precipitation accumulated over the 9 days. Daytime precipitation is here defined as the amount that falls between 8 LT and 20 LT, whereas nighttime precipitation makes up the other half of the day. The figures show that the spatial pattern of daytime and nighttime precipitation is fundamentally different.

Figure B.5 reveals that there are no systematic differences in the spatial pattern of daytime precipitation between RAW and SM. The pattern of all simulations resembles the elevation map, which is what we expect because the mountains favour the formation of deep convection during the day. The highest amount of precipitation falls over the Southwestern parts of the Alpine region. A lot of moisture converges in this area. This is probably due to a large amount of moisture carried from the Mediterranean sea towards the
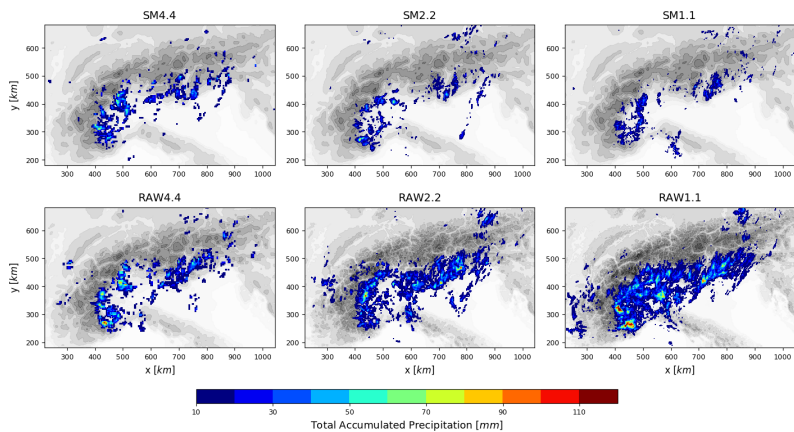
Figure B.6: As Fig. B.5 but for the total accumulated nighttime (between 20 LT and 8 LT) precipitation.

Alps. The day-time precipitation pattern also shows a tendency towards the Southern edge of the Alpine arc. In the high-resolution RAW simulations, the convective activity tends to be reduced over the Eastern and Central Alps and increased over the Southwestern Alps, compared to their corresponding SM simulations.

Looking at the spatial pattern of nighttime precipitation in Fig. B.6, we see that virtually all the additional night-time precipitation in the RAW simulations falls over the Southern Alpine flanks and over the Po Valley in Northern Italy. The amount increases systematically with higher resolution in RAW. There is no such trend in SM, or even a small negative trend, implying that the nighttime precipitation over these areas in RAW is a consequence of the higher degree of detail in topography and surface fields.

B.3.2 Alpine Pumping

For a first impression of the overall intensity of the thermally-driven convective activity, the strength of the Alpine pumping is compared between the SM and RAW simulations. The Alpine pumping is characterized by the convergence of horizontal winds close to the surface during the day combined with vertical export of air by convection over the Alpine region. A key quantity associated with this process is water vapor because it fuels moist convection. Two good measures of the strength of the Alpine pumping are thus the lateral import of water vapor into the sub-cloud layer of the Alpine region and the vertical export of water vapor out of the sub-cloud layer of the Alpine region.

The mean diurnal cycle of lateral water vapor flux into the sub-cloud layer of
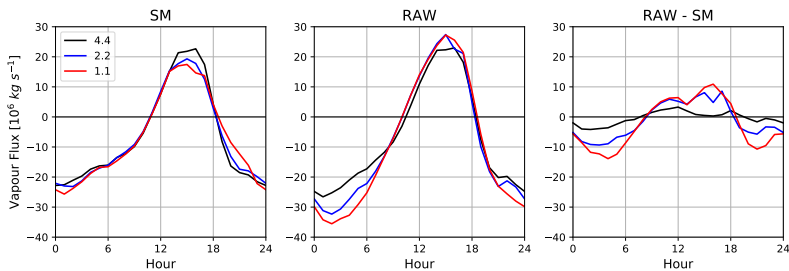
Figure B.7: Alpine pumping represented by the mean diurnal cycle of the lateral water vapor flux $[10^6 \, kg \, s^{-1}]$ for the subcloud layer (i.e. below 2500 m altitude) over the Alpine region. Positive values indicate a moistening of the subcloud layer. The right plot shows the difference between RAW and SM. The model resolutions are 4.4 (black), 2.2 (blue) and 1.1 (red) km.

the Alpine region is shown in Fig. B.7. The lateral fluxes are considered up to an altitude of 2.5 km which roughly corresponds to the domain-average cloud base. The differences between RAW and SM are shown in the right panel of Fig. B.7. Both, the water vapor import during the day and the water vapor export during the night are enhanced in RAW2.2 and RAW1.1 compared to the corresponding SM simulations. This indicates that the Alpine pumping is enhanced with increasing degree of detail in topography and surface fields.

B.3.3 Convective Features

This section provides an overview of the convective activity in both groups of simulations. Convection is characterized by the vertical in-cloud mass flux and by the moist variables. In the second part, frequency distributions of the horizontal and vertical extent of the convective clouds are studied.

Convective Mass Flux

The mean diurnal cycle of the domain-averaged convective mass flux is shown in Fig. B.8. Only grid points with a velocity greater than $1 \, m \, s^{-1}$ and a minimum amount of specific cloud liquid water ($10^{-6} \, kg \, kg^{-1}$) or cloud ice ($10^{-10} \, kg \, kg^{-1}$) are considered in the calculation of the convective mass flux. The changes in the domain-averaged convective mass flux with higher resolution are similar in RAW and SM. However, the timing of the peak intensity is delayed by 1-2 hours in the RAW simulations compared to the corresponding SM simulations. Also, the convective activity is prolonged in RAW and, integrated over time, the convective mass flux is larger than in SM. These findings are in line with the longer duration of surface precipitation shown in Fig. B.4.

The frequency distribution of the vertical velocity is analyzed at the altitude
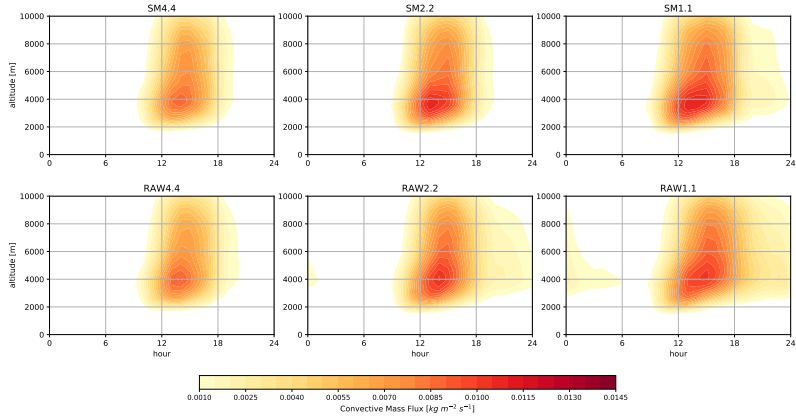
Figure B.8: Mean diurnal cycle of the vertical profile of domain-averaged convective mass flux [kg m^{-2} s^{-1}] shown between sea level and an altitude of 10 km. Values below 0.001 kg m^{-2} s^{-1} are masked. The results of the SM and the RAW group of simulations are shown in the upper and the lower panels, respectively. The columns show the simulations of each group with decreasing horizontal grid spacing from 4.4 km (left) to 1.1 km (right).
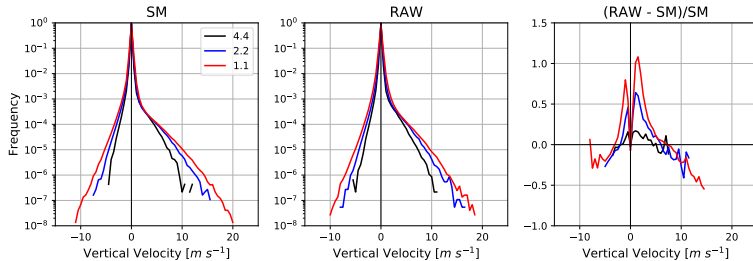
Figure B.9: Vertical velocity frequency distributions over the Alpine region at an altitude of 4 km. The distributions are calculated from hourly mean velocity values over all 9 days and all model grid points within the Alpine region. The Alpine region is indicated by the solid rectangle shown in Fig. B.2. The results of the SM and the RAW simulations are shown in the left and middle plots, respectively. The right plot shows the difference in the frequency between RAW and SM, normalised by the frequency in SM. The model resolutions are 4.4 (black), 2.2 (blue) and 1.1 (red) km.
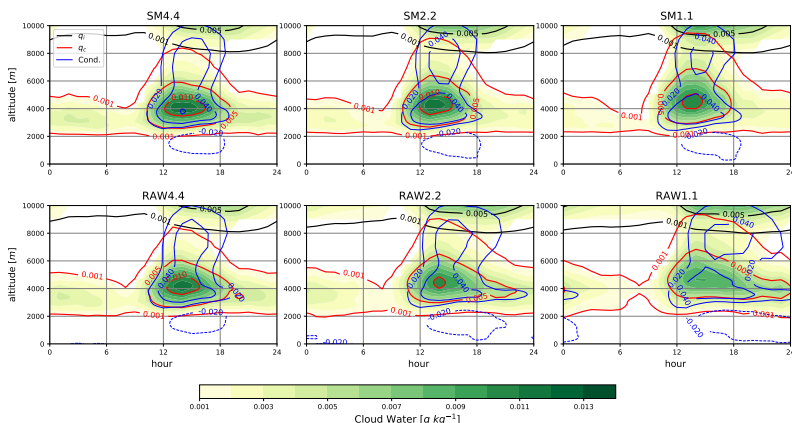
Figure B.10: Mean diurnal cycle of the vertical profile of domain-average cloud wa-
ter content [g kg⁻¹], shown between sea level and an altitude of 10 km. Domain-
average values below 0.001 g kg⁻¹ are masked. Cloud water is the sum of the
specific cloud liquid water content (q_c, shown by the red contour lines) and the
specific cloud ice content (q_i, shown by the black contour lines). Additionally,
the condensation rate [g kg⁻¹ hr⁻¹] is shown by the blue contour lines. Dashed
lines imply evaporation. The results of the SM and the RAW groups of simula-
tions are shown in the upper and lower panels, respectively. The columns
show the simulations of each group with decreasing horizontal grid spacing from
4.4 km (left) to 1.1 km (right).

of maximum convective mass flux taken from Fig. B.8. The left and middle
plots in Fig. B.9 show the frequency distribution of vertical velocity at an alti-
tude of 4 km in SM and RAW, respectively. The right plot shows the change
in relative frequency between RAW and SM normalized by SM (y-axis) for
a given velocity bin (x-axis). A value of 1 thus means that the frequency of
a given velocity in RAW is twice the frequency in SM. Note that the follow-
ing result is qualitatively the same at all altitudes above 2 km. Focusing on
positive velocity values (updrafts), the RAW velocity distribution is charac-
terized by a higher frequency of weak updrafts and lower frequency of strong
updrafts compared to SM. Values around 1 m s⁻¹ are twice as frequent in
RAW, whereas updrafts around 15 m s⁻¹ occur with half the frequency of SM.
The number of grid points with non-zero velocity is higher in RAW. This
means that the larger number of resolved orographic peaks in RAW trans-
lates to a larger number of updrafts. Considering the lower domain-average
convective mass flux in RAW (cf. Fig. B.8), it makes sense that the single
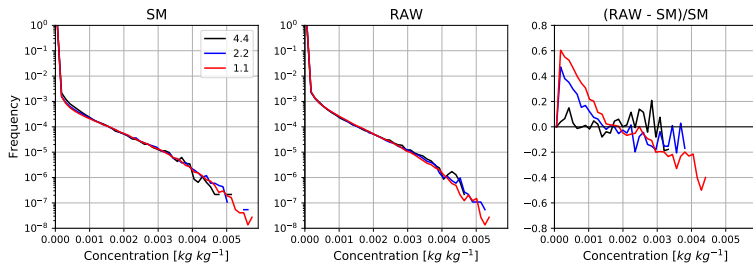updrafts are weaker on average.

Figure B.11: Frequency distribution of the specific cloud liquid water content over the Alpine region at an altitude of 4300 m. The distributions are calculated from hourly mean values of all nine days and all model grid points within the Alpine region. The Alpine region is indicated by the solid rectangle shown in Fig. B.2. The results of the SM and the RAW simulations are shown in the left and middle plots, respectively. The right plot shows the difference in the frequency between RAW and SM, normalised by the frequency in SM. The model resolutions are 4.4 (black), 2.2 (blue) and 1.1 (red) km.

Moist Variables

The mean diurnal cycle of the vertical profile of domain-average cloud water is shown in Fig. B.10. The green shading indicates the specific total cloud water content which is the sum of specific cloud liquid water content (q_c, red contour lines) and specific cloud ice content (q_i, black contour lines). In both, the RAW and the SM simulations, the altitude of maximum cloud water content is increasingly elevated with higher resolution (about 700 m difference between the 1.1 and 4.4 km simulations). The cloud base is located at roughly 2.5 km in all simulations.

Consistent with the mean diurnal cycle of the surface precipitation rate (Fig. B.4), the imprint of convection on the mean diurnal cycle of total cloud water in the RAW simulations is less distinct in time than in the SM simulations. In place of a clear cloud water peak in the SM simulations during the early afternoon, there is a less pronounced peak in the high-resolution RAW simulations which is dispersed over time. Integrated over space and time, the amount of q_c and q_i is higher the RAW simulations than in the SM simulations.

The vertical minimum of total cloud water in the upper troposphere (at an altitude of 7-8 km) in Fig. B.10 goes along with a peak in condensation (blue contour line in Fig. B.10). As will be shown later, this altitude is characterised by strong formation of snow and slightly below graupel. The magnitude and duration of this upper-level condensation peak is reduced with higher resolution in SM. The opposite can be observed in the RAW1.1 simulation: the band of condensation keeps a constant vertical extent throughout the late afternoon and early evening.
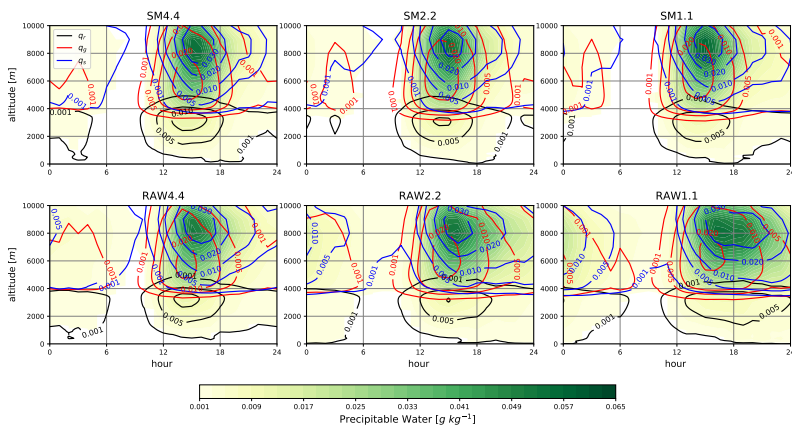
141

Figure B.12: Mean diurnal cycle of the vertical profile of domain-average precip-
itable water content [g kg^{-1}], shown between sea level and an altitude of 10 km.
Domain-average values below 0.001 g kg^{-1} are masked. Precipitable water is the
sum of the specific rain cotent (q_r, shown by the black contour lines), specific
graupel content (q_g, shown by the red contour lines) and specific snow content
(q_s, shown by the blue contour lines). The results of the SM and the RAW simu-
lations are shown in the upper and the lower panels, respectively. The columns
show the simulations of each group with decreasing horizontal grid spacing from
4.4 km (left) to 1.1 km (right).

Figure B.11 shows the frequency distribution of q_c at an altitude of 4.3 km.
The altitude is chosen to represent the region of maximum domain-average
q_c in all simulations, as good as possible. The findings at this altitude are
qualitatively representative for all levels with a pronounced domain-average
q_c maximum (3.5-5.5 km, cf. Fig. B.10). Similar to the vertical velocity fre-
quency distributions (Fig. B.9), grid points with low q_c values are more fre-
quent in RAW whereas grid points with high q_c values are less frequent. The
mean diurnal cycle of precipitating hydrometeors is shown in Fig. B.12. In
the higher-resolved simulations of both groups, rain (q_r, black contour lines)
has a reduced peak intensity. In the RAW simulations, the duration of rain
is additionally extended. In the RAW2.2 and RAW1.1 simulations, large
amounts of precipitation reach down to altitudes close to mean sea level.
This is another illustration of the night-time precipitation over the Po Valley
in these simulations.
The mean diurnal cycle of the total precipitating water shown in Fig. B.12
(green shading, sum of rain, graupel and snow) is similar at all resolutions in
the SM simulations. In the RAW simulations, the imprint of longer-lasting
convective activity is again visible. In line with the delayed onset of convec-
tion found previously, the evolution of total precipitating water is 1-2 hours
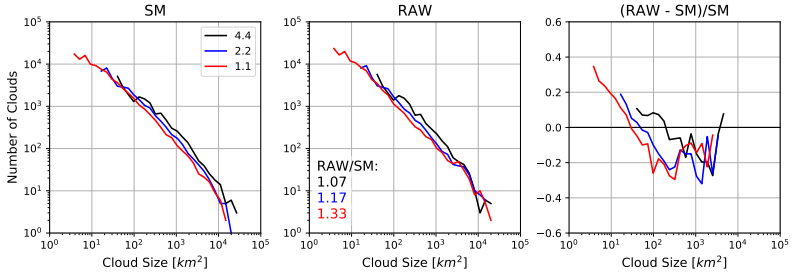delayed in RAW2.2 and RAW1.1, compared to the corresponding SM simula-

Figure B.13: Cloud size frequency distribution over the Alpine region during the nine days. The distributions are calculated from hourly mean cloud structures within the Alpine region during all nine days. The size of the clouds represents the horizontal extent of cloudy patches with a liquid water path greater than $0.01\,\mathrm{kg\,m^{-2}}$. The Alpine region is indicated by the solid rectangle shown in Fig. B.2. The results of the SM and the RAW simulations are shown in the left and middle plots, respectively. The right plot shows the difference in the frequency between RAW and SM, normalised by the frequency in SM. The model resolutions are 4.4 (black), 2.2 (blue) and 1.1 (red) km. The labels RAW/SM in the middle plot indicate the ratio between the total number of clouds in RAW and SM for the respective model resolution.

tions. As it is the case for q_c and q_i, the amounts of rain, graupel and snow, integrated over time and space, are higher in the RAW simulations than in their corresponding SM simulations.

Similar to q_c (Fig. B.10), the peak concentration of graupel is reduced in the RAW simulations but decays slower than in SM. The mean diurnal cycle of snow is peculiar in this respect as the peak concentrations in RAW1.1 are equally high as in SM1.1. However, the peak concentrations are retained much longer in RAW1.1 than in SM1.1 (from 15 LT to 21 LT). Consequently, the total time integrated amount of snow is more than twice as large in RAW1.1 than in SM1.1. Furthermore, the vertical extent, timing and duration of the peak concentration of snow in RAW1.1 is very similar to the upper-level maximum of condensation found in Fig. B.10. This suggests that the high snow concentration in RAW1.1 is probably linked to the maximum in condensation at that altitude.

Summarizng and combining the findings shown in Figs. B.10, B.11 and B.12, there is additional evidence that the convective activity is prolonged in RAW, but with reduced maximum intensity. The single convective cells are weaker. The longer duration of convective activity overcompensates for the reduced intensity. Thus, integrated over space and time, the amount of water in the atmosphere is larger.

Cloud Properties

Figure B.13 shows the size distribution of all convective clouds that form during the 9 days of simulation. The term size here represents the horizontal extent of the clouds. The distributions created from the SM and the RAW simulations are shown in the left and middle plots, respectively. As the minimum size of a cloud is limited by the area of a grid cell, smaller clouds form in the simulations with higher resolution. Consequently, the number of clouds increases with higher resolution, if a similar amount of cloud water is available. This is indeed the case. In the SM simulations, a doubling of the resolution increases the number of clouds by a factor of about 3 (not shown). The total amount of clouds also differs between the RAW and the SM groups. Systematically more clouds form in RAW than in SM. This is indicated by the label RAW/SM in the lower-left corner of the middle plot. The numbers indicate, for each resolution, the ratio between the number of clouds in RAW and SM. Under the assumption made above, that there is a similar amount of cloud water in both groups, the RAW simulations can be expected to produce smaller clouds on average. This, as well, turns out to be the case as shown in the following.

For a given size bin, the difference in the number of clouds between RAW and SM, normalised by the number of clouds in SM, is shown in the right plot of Fig. B.13. For example, a value of 0.5 would imply that the number of clouds in a given bin is 50 % larger in RAW than in SM. The difference is only shown for bins containing more than 30 clouds in RAW and SM. The lines indicate that relatively small clouds are more abundant in the high-resolved RAW simulations compared to their corresponding SM simulations. For instance, the number of the smallest clouds is about 35% larger in RAW1.1 than in SM1.1. Larger clouds of order $O(100\,\text{km}^2)$, on the other hand, are less frequent in RAW1.1. For the largest clouds of order $O(1000\,\text{km}^2)$, there is no clear difference between RAW and SM. It is notable that the comparably small difference in topography and surface fields between RAW4.4 and SM4.4 is enough to significantly change the horizontal extent of the clouds.

B.4 Discussion and Conclusions

The aim of this study was to understand the impact of the resolution of the model topography and surface fields on the simulation of summertime orographic moist convection. The COSMO model was used to simulate 9 days of reoccurring orographic convection over the Alps. 6 different simulations are conducted and divided into two groups, each one consisting of 3 simulations, run at a horizontal grid spacings of 4.4, 2.2 and 1.1 km. In the first group (SM), the topography and surface fields are filtered to obtain an equal representation at all horizontal resolutions. In the second group (RAW), the topography and surface fields are interpolated to the model grid. SM and RAW are compared to discuss the influence of the resolution

of topography and surface fields on the simulation of moist orographic convection. In the following, the two research questions are answered based on the results presented in Section B.3.

Research Question 1: *How does the degree of detail in the topography and surface fields affect the processes driving orographic moist convection and the resulting features of orographic moist convection (onset time, intensity and duration, as well as accumulated surface precipitation)?*

In RAW the following changes in the simulated moist convective activity compared to SM were observed:

- The onset of surface precipitation is delayed, its maximum intensity is reduced and it rains longer. The total accumulated precipitation increases.

- The spatial pattern of total accumulated surface precipitation reveals that the day-time precipitation pattern does not change remarkably. During the night, a large amount of additional precipitation is generated over the Po Valley and the Southern Alps. This precipitation is virtually absent in SM.

- The Alpine pumping is enhanced.

- Consistent with the mean diurnal cycle of surface precipitation, the mean diurnal cycles of the convective mass flux and of moist variables exhibit a delayed onset, a reduced maximum intensity and a longer duration.

- The amount of all moist variables integrated over time and space increases.

These findings highlight that the simulated convective activity is more pronounced in RAW, not because it is more intense, but rather because its duration is prolonged. Integrated over space and time, there is a higher amount of cloud water and precipitable water in the atmosphere, ultimately resulting in increased surface precipitation. The intensified Alpine pumping provide the required additional moisture to the atmosphere. The differences between RAW and SM increase with model resolution for all analyzed variables. This means that the differences in the simulated convective activity due to the increased resolution of topography and surface fields are systematic. Besides that, for most of the domain-averaged variables the difference between RAW1.1 and SM1.1 is larger than the difference between SM1.1 and SM4.4, which suggests that the resolution of topography and surface fields has a stronger impact than the model grid spacing.

Research Question 2: *Do small-scale variations of topography and surface fields impose visible scales in the prognostic fields (vertical velocity, moist variables)? If so, what is the relative importance of these 'external scales' compared to the scale imposed by the horizontal grid spacing?*

This question is addressed with the statistical distributions of vertical velocity, cloud water content and cloud horizontal size. When RAW and SM are compared, the frequency of grid points with weak/strong updrafts increases/decreases with more detailed topography and surface fields, and the total number of updrafts increases. Furthermore, there are more/less grid points with low/high cloud water content and the number of grid points with non-zero cloud water content increases. Finally, the number of clouds increases and smaller/larger clouds are more/less frequent in RAW. These results suggest that small-scale details in the topography and surface fields impose visible scales in the prognostic fields. However, most of these variables are more sensitive to the horizontal grid spacing rather than to the resolution of the external parameters. For instance, an increase in the model resolution from 4.4 to 1.1 km increases the number of clouds by about 500 %. The corresponding change in the topography and the surface fields accounts for an additional increase of 30 %. The change in the prognostic fields due to the grid spacing is thus roughly 15 times larger than the one induced by the resolution of topography and surface fields.

To conclude, this study discussed the changes in the simulation of thermally-driven moist convection due to a more detailed representation of the topography and surface fields in convection-resolving simulations. Even though this case study focused specifically on the Alpine region, similar results may be expected to occur in real-case simulations over different mountainous regions. This study focuses solely on thermally-driven moist convection. In synoptic situations with a stronger background flow, the larger amount of small-scale details in the topography may further influence the triggering of deep-convective cells (e.g. Kirshbaum et al., 2007).

Bibliography

Ancell, B. C., Bogusz, A., Lauridsen, M. J., and Nauert, C. J. Seeding chaos: The dire consequences of numerical noise in nwp perturbation experiments. *Bull. Amer. Meteor. Soc.*, 99(3):615–628, 2018.

Arakawa, A. The cumulus parameterization problem: Past, present, and future. *J. Climate*, 17(13):2493–2525, 2004.

Baldauf, M., Seifert, A., Förstner, J., Majewski, D., Raschendorfer, M., and Reinhardt, T. Operational convective-scale numerical weather prediction with the cosmo model: description and sensitivities. *Mon. Wea. Rev.*, 139 (12):3887–3905, 2011.

Ban, N., Schmidli, J., and Schär, C. Evaluation of the convection-resolving regional climate modeling approach in decade-long simulations. *J. Geophys. Res.: Atmos.*, 119(13):7889–7907, 2014.

Ban, N., Schmidli, J., and Schär, C. Heavy precipitation in a changing climate: Does short-term summer precipitation increase faster? *Geophys. Res. Lett.*, 42(4):1165–1172, 2015.

Banta, R. M. Daytime boundary-layer evolution over mountainous terrain. Part I: Observations of the dry circulations. *Mon. Wea. Rev.*, 112(2):340–356, 1984.

Banta, R. M. The role of mountain flows in making clouds. *Atmos. Proc. over Complex Terrain, Meteor. Monogr.*, 23(45):229–282, 1990.

Banta, R. M. and Barker Schaaf, C. Thunderstorm genesis zones in the colorado rocky mountains as determined by traceback of geosynchronous satellite images. *Mon. Wea. Rev.*, 115(2):463–476, 1987.

Bao, X. and Zhang, F. Impacts of the mountain–plains solenoid and cold pool dynamics on the diurnal variation of warm-season precipitation over northern China. *Atmos. Chem. Phys*, 13:6965–6982, 2013.

Barthlott, C., Burton, R., Kirshbaum, D., Hanley, K., Richard, E., Chaboureau, J.-P., Trentmann, J., Kern, B., Bauer, H.-S., Schwitalla, T., et al. Initiation of deep convection at marginal instability in an ensemble

of mesoscale models: a case-study from cops. *Quart. J. Roy. Meteor. Soc.*, 137(S1):118–136, 2011.

Barthlott, C. and Hoose, C. Spatial and temporal variability of clouds and precipitation over germany: multiscale simulations across the" gray zone". *Atmos. Chem. & Phys. Discussions*, 15(12), 2015.

Bechtold, P., Chaboureau, J.-P., Beljaars, A., Betts, A., Köhler, M., Miller, M., and Redelsperger, J.-L. The simulation of the diurnal cycle of convective precipitation over land in a global model. *Quart. J. Roy. Meteor. Soc.*, 130(604):3119–3137, 2004.

Bechtold, P., Semane, N., Lopez, P., Chaboureau, J.-P., Beljaars, A., and Bormann, N. Representing equilibrium and nonequilibrium convection in large-scale models. *J. Atmos. Sci.*, 71(2):734–753, 2014.

Bengtsson, L., Steinheimer, M., Bechtold, P., and Geleyn, J.-F. A stochastic parametrization for deep convection using cellular automata. *Quart. J. Roy. Meteor. Soc.*, 139(675):1533–1543, 2013.

Bennett, L. J., Blyth, A. M., Burton, R. R., Gadian, A. M., Weckwerth, T. M., Behrendt, A., Di Girolamo, P., Dorninger, M., Lock, S.-J., Smith, V. H., et al. Initiation of convection over the black forest mountains during cops iop15a. *Quart. J. Roy. Meteor. Soc.*, 137(S1):176–189, 2011.

Berg, P., Wagner, S., Kunstmann, H., and Schädler, G. High resolution regional climate model simulations for germany: part i—validation. *Clim. Dyn.*, 40(1-2):401–414, 2013.

Bergeron, T. On the low-level redistribution of atmospheric water caused by orography. In *Suppl. Proc. Int. Conf. Cloud Phys., Tokyo, 1965*, pages 96–100, 1965.

Blackadar, A. K. The vertical distribution of wind and turbulent exchange in a neutral atmosphere. *J. Geophys. Res.*, 67(8):3095–3102, 1962.

Böing, S. J., Jonker, H. J., Siebesma, A. P., and Grabowski, W. W. Influence of the subcloud layer on the development of a deep convective ensemble. *J. Atmos. Sci.*, 69(9):2682–2698, 2012.

Bott, A. A positive definite advection scheme obtained by nonlinear renormalization of the advective fluxes. *Mon. Wea. Rev.*, 117(5):1006–1016, 1989.

Bougeault, P., Binder, P., Buzzi, A., Dirks, R., Houze, R., Kuettner, J., Smith, R., Steinacker, R., and VoIkert, H. The map special observing period. *Bull. Amer. Meteor. Soc.*, 82(3):433–462, 2001.

Boutle, I., Eyre, J., and Lock, A. Seamless stratocumulus simulation across the turbulent gray zone. *Mon. Wea. Rev.*, 142(4):1655–1668, 2014.

Braham Jr, R. R. and Draginis, M. Roots of orographic cumuli. *J. Meteor.*, 17(2):214–226, 1960.

Brockhaus, P., Lüthi, D., and Schär, C. Aspects of the diurnal cycle in a regional climate model. *Meteor. Zeit.*, 17(4):433–443, 2008.

Brousseau, P., Seity, Y., Ricard, D., and Léger, J. Improvement of the forecast of convective activity from the arome-france system. *Quart. J. Roy. Meteor. Soc.*, 142(699):2231–2243, 2016.

Bryan, G. H. and Morrison, H. Sensitivity of a simulated squall line to horizontal resolution and parameterization of microphysics. *Mon. Wea. Rev.*, 140(1):202–225, 2012.

Bryan, G. H. and Rotunno, R. Statistical convergence in simulated moist absolutely unstable layers. In *Preprints, 11th Conf. on Mesoscale Processes, Albuquerque, NM, Amer. Meteor. Soc. M*, volume 1, 2005.

Bryan, G. H., Wyngaard, J. C., and Fritsch, J. M. Resolution requirements for the simulation of deep moist convection. *Mon. Wea. Rev.*, 131(10): 2394–2416, 2003.

Clark, P., Roberts, N., Lean, H., Ballard, S. P., and Charlton-Perez, C. Convection-permitting models: a step-change in rainfall forecasting. *Meteor. Appl.*, 23(2):165–181, 2016.

Corsmeier, U., Kottmeier, C., Winkler, P., Lugauer, M., Reitebuch, O., and Drobinski, P. Flow modification and mesoscale transport caused by alpine pumping: A vertikator case study. In *Proc. Int. Conf. on Alpine Meteorology*, pages 138–140, 2003.

Craig, G. C. and Dörnbrack, A. Entrainment in cumulus clouds: what resolution is cloud-resolving? *J. Atmos. Sci.*, 65(12):3978–3988, 2008.

Crook, N. A. and Tucker, D. F. Flow over heated terrain. Part I: linear theory and idealized numerical simulations. *Mon. Wea. Rev.*, 133(9):2552–2564, 2005.

Dahai, Z. R. X. Multi-scale turbulent planetary boundary layer parameterization in mesoscale numerical simulation. *Quart. J. Appl. Meteor.*, 5:003, 2004.

Dai, A. and Trenberth, K. E. The diurnal cycle and its depiction in the Community Climate System Model. *J. Climate*, 17(5):930–951, 2004.

Damiani, R., Geerts, B., Demko, J., Haimov, S., French, J., Zehnder, J., Razdan, A., Hu, J., Petti, J., Leuthold, M., et al. The cumulus, photogrammetric, in situ, and Doppler observations experiment of 2006. *Bull. Amer. Meteor. Soc.*, 89(1):57–73, 2008.

Dauhut, T., Chaboureau, J.-P., Escobar, J., and Mascart, P. Large-eddy simulations of hector the convector making the stratosphere wetter. *Atmos. Sci. Let.*, 16(2):135–140, 2015.

de Rooy, W. C., Bechtold, P., Fröhlich, K., Hohenegger, C., Jonker, H., Mironov, D., Pier Siebesma, A., Teixeira, J., and Yano, J.-I. Entrainment and detrainment in cumulus convection: an overview. *Quart. J. Roy. Meteor. Soc.*, 139(670):1–19, 2013.

Deardorff, J. W. Convective velocity and temperature scales for the unstable planetary boundary layer and for rayleigh convection. *J. Atmos. Sci.*, 27 (8):1211–1213, 1970.

Deardorff, J. W. The use of subgrid transport equations in a three-dimensional model of atmospheric turbulence. *J. Flui. Eng.*, 95(3):429–438, 1973.

Dee, D. P., Uppala, S., Simmons, A., Berrisford, P., Poli, P., Kobayashi, S., Andrae, U., Balmaseda, M., Balsamo, G., Bauer, d. P., et al. The era-interim reanalysis: Configuration and performance of the data assimilation system. *Quart. J. Roy. Meteor. Soc.*, 137(656):553–597, 2011.

Demko, J. C. and Geerts, B. A numerical study of the evolving convective boundary layer and orographic circulation around the santa catalina mountains in arizona. part i: Circulation without deep convection. *Mon. Wea. Rev.*, 138(9):3603–3622, 2010a.

Demko, J. C. and Geerts, B. A numerical study of the evolving convective boundary layer and orographic circulation around the santa catalina mountains in arizona. part ii: Interaction with deep convection. *Mon. Wea. Rev.*, 138(9):3603–3622, 2010b.

Demko, J. C., Geerts, B., Miao, Q., and Zehnder, J. A. Boundary layer energy transport and cumulus development over a heated mountain: An observational study. *Mon. Wea. Rev.*, 137(1):447–468, 2009.

Déqué, M., Rowell, D., Lüthi, D., Giorgi, F., Christensen, J., Rockel, B., Jacob, D., Kjellström, E., De Castro, M., and van den Hurk, B. An intercomparison of regional climate simulations for europe: assessing uncertainties in model projections. *Climatic Change*, 81(1):53–70, 2007.

Doms, G., Förstner, J., Heise, E., Herzog, H., Mironov, D., Raschendorfer, M., Reinhardt, T., Ritter, B., Schrodin, R., Schulz, J.-P., et al. A description of the nonhydrostatic regional cosmo model. part ii: physical parameterization. *Deutscher Wetterdienst, Offenbach, Germany*, 2011.

Done, J., Davis, C. A., and Weisman, M. The next generation of NWP: explicit forecasts of convection using the Weather Research and Forecasting (WRF) model. *Atmos. Sci. Let.*, 5(6):110–117, 2004.

Donner, L. J., Wyman, B. L., Hemler, R. S., Horowitz, L. W., Ming, Y., Zhao, M., Golaz, J.-C., Ginoux, P., Lin, S.-J., Schwarzkopf, M. D., et al. The dynamical core, physical parameterizations, and basic simulation characteristics of the atmospheric component am3 of the gfdl global coupled model cm3. *J. Climate*, 24(13):3484–3519, 2011.

Drobinski, P., Ducrocq, V., Alpert, P., Anagnostou, E., Béranger, K., Borga, M., Braud, I., Chanzy, A., Davolio, S., Delrieu, G., et al. Hymex: A 10-year multidisciplinary program on the mediterranean water cycle. *Bull. Amer. Meteor. Soc.*, 95(7):1063–1082, 2014.

Egger, J. Thermally forced flows: theory. *Atmos. Proc. over Complex Terrain, Meteor. Monogr.*, 23(45):43–57, 1990.

Emanuel, K. A. *Atmospheric convection.* Oxford University Press, 1994.

Errico, R. and Baumhefner, D. Predictability experiments using a high-resolution limited-area model. *Mon. Wea. Rev.*, 115(2):488–504, 1987.

Fiddes, S. L., Pezza, A. B., and Barras, V. Synoptic climatology of extreme precipitation in alpine australia. *Int. J. Climatol.*, 35(2):172–188, 2015.

Fortin, V., Abaza, M., Anctil, F., and Turcotte, R. Why should ensemble spread match the rmse of the ensemble mean? *J. Hydrometeor.*, 15(4):1708–1713, 2014.

Fosser, G., Khodayar, S., and Berg, P. Benefit of convection permitting climate model simulations in the representation of convective precipitation. *Clim. Dyn.*, 44(1-2):45–60, 2015.

Frei, C. and Schär, C. A precipitation climatology of the alps from high-resolution rain-gauge observations. *Int. J. Climatol.*, 18(8):873–900, 1998.

Fuhrer, O. and Schär, C. Dynamics of orographically triggered banded convection in sheared moist orographic flows. *J. Atmos. Sci.*, 64(10):3542–3561, 2007.

Grabowski, W., Bechtold, P., Cheng, A., Forbes, R., Halliwell, C., Khairout-dinov, M., Lang, S., Nasuno, T., Petch, J., Tao, W.-K., et al. Daytime convective development over land: a model intercomparison based on LBA observations. *Quart. J. Roy. Meteor. Soc.*, 132(615):317–344, 2006.

Grabowski, W. W. Coupling cloud processes with the large-scale dynamics using the cloud-resolving convection parameterization (crcp). *J. Atmos. Sci.*, 58(9):978–997, 2001.

Hanley, K. E., Plant, R. S., Stein, T. H., Hogan, R. J., Nicol, J. C., Lean, H. W., Halliwell, C., and Clark, P. A. Mixing-length controls on high-resolution simulations of convective storms. *Quart. J. Roy. Meteor. Soc.*, 141(686):272–284, 2015.

Harvey, B., Methven, J., Eagle, C., and Lean, H. Does the representation of flow structure and turbulence at a cold front converge on multiscale observations with model resolution? *Mon. Wea. Rev.*, 145(11):4345–4363, 2017.

Hassanzadeh, H., Schmidli, J., Langhans, W., Schlemmer, L., and Schär, C. Impact of topography on the diurnal cycle of summertime moist convection in idealized simulations. *Meteor. Zeit.*, 2015.

Heinzeller, D., Duda, M., and Kunstmann, H. Towards convection-resolving, global atmospheric simulations with the model for prediction across scales (mpas) v3. 1: an extreme scaling experiment. *Geosc. Mod. Devel.*, 9(1):77, 2016.

Heise, E., Lange, M., Ritter, B., and Schrodin., R. Improvement and valida-tion of the multi-layer soil model. *COSMO Newsletter*, 3:198–203, 2003.

Herzog, H.-J., Vogel, G., and Schubert, U. LLM–a nonhydrostatic model applied to high-resolving simulations of turbulent fluxes over heterogeneous terrain. *Theor. and appl. clim.*, 73(1-2):67–86, 2002.

Hohenegger, C., Brockhaus, P., Bretherton, C. S., and Schär, C. The soil moisture–precipitation feedback in simulations with explicit and parame-terized convection. *J. Climate*, 22(19):5003–5020, 2009.

Hohenegger, C., Brockhaus, P., and Schär, C. Towards climate simulations at cloud-resolving scales. *Meteor. Zeit.*, 17(4):383–394, 2008.

Hohenegger, C. and Schär, C. Atmospheric predictability at synoptic versus cloud-resolving scales. *Bull. Amer. Meteor. Soc.*, 88(11):1783–1793, 2007.

Hohenegger, C., Schlemmer, L., and Silvers, L. Coupling of convection and circulation at various resolutions. *Tellus A*, 67, 2015.

Hong, S.-Y. and Pan, H.-L. Nonlocal boundary layer vertical diffusion in a medium-range forecast model. *Mon. Wea. Rev.*, 124(10):2322–2339, 1996.

Honnert, R. Representation of the grey zone of turbulence in the atmospheric boundary layer. *Adv. Sci. Res.*, 13:63–67, 2016.

Honnert, R. and Masson, V. What is the smallest physically acceptable scale for 1d turbulence schemes? *Front. Earth Sci.*, 2:27, 2014.

Honnert, R., Masson, V., and Couvreux, F. A diagnostic for evaluating the representation of turbulence in atmospheric models at the kilometric scale. *J. Atmos. Sci.*, 68(12):3112–3131, 2011.

Hourdin, F., Musat, I., Bony, S., Braconnot, P., Codron, F., Dufresne, J.-L., Fairhead, L., Filiberti, M.-A., Friedlingstein, P., Grandpeix, J.-Y., et al. The lmdz4 general circulation model: climate performance and sensitivity to parametrized physics with emphasis on tropical convection. *Clim. Dyn.*, 27(7-8):787–813, 2006.

Houze, R. *Cloud Dynamics*. Academic, San Diego, California, 1993.

Huang, J., Cassiani, M., and Albertson, J. Analysis of coherent structures within the atmospheric boundary layer. *Boundary-Layer Meteor.*, 131(2): 147–171, 2009.

Ito, J., Niino, H., Nakanishi, M., and Moeng, C.-H. An extension of the mellor–yamada model to the terra incognita zone for dry convective mixed layers in the free convection regime. *Boundary-Layer Meteor.*, 157(1):23–43, 2015.

Jeevanjee, N. Vertical velocity in the gray zone. *J. Adv. Model. Earth Syst.*, 9(6):2304–2316, 2017.

Kabat, P., Claussen, M., Dirmeyer, P. A., Gash, J. H., de Guenni, L. B., Meybeck, M., Hutjes, R. W., Pielke Sr, R. A., and Lütkemeier, S. *Vegetation, Water, Humans and the Climate: A New Perspective on an Internactive System*. Springer Science & Business Media, 2004.

Kain, J. S. and Fritsch, J. M. A one-dimensional entraining/detraining plume model and its application in convective parameterization. *J. Atmos. Sci.*, 47(23):2784–2802, 1990.

Kajikawa, Y., Miyamoto, Y., Yoshida, R., Yamaura, T., Yashiro, H., and Tomita, H. Resolution dependence of deep convections in a global simulation from over 10-kilometer to sub-kilometer grid spacing. *Progress in Earth and Planetary Science*, 3(1):16, 2016.

Kalnay, E. *Atmospheric modeling, data assimilation and predictability*. Cambridge university press, 2003.

Keller, M., Fuhrer, O., Schmidli, J., Stengel, M., Stöckli, R., and Schär, C. Evaluation of convection-resolving models using satellite data: The diurnal cycle of summer convection over the alps. *Meteor. Zeit.*, pages 165–179, 2016.

Kendon, E. J., Roberts, N. M., Fowler, H. J., Roberts, M. J., Chan, S. C., and Senior, C. A. Heavier summer downpours with climate change revealed by weather forecast resolution model. *Nature Climate Change*, 4(7):570, 2014.

Kendon, E. J., Roberts, N. M., Senior, C. A., and Roberts, M. J. Realism of rainfall in a very high-resolution regional climate model. *J. Climate*, 25 (17):5791–5806, 2012.

Khairoutdinov, M. and Randall, D. High-resolution simulation of shallow-to-deep convection transition over land. *J. Atmos. Sci.*, 63(12):3421–3436, 2006.

Kirshbaum, D. and Grant, A. Invigoration of cumulus cloud fields by mesoscale ascent. *Quart. J. Roy. Meteor. Soc.*, 138(669):2136–2150, 2012.

Kirshbaum, D. J. Cloud-resolving simulations of deep convection over a heated mountain. *J. Atmos. Sci.*, 68(2):361–378, 2011.

Kirshbaum, D. J., Adler, B., Kalthoff, N., Barthlott, C., and Serafin, S. Moist orographic convection: Physical mechanisms and links to surface-exchange processes. *Atmosphere*, 9(3):80, 2018.

Kirshbaum, D. J., Bryan, G. H., Rotunno, R., and Durran, D. R. The triggering of orographic rainbands by small-scale topography. *J. Atmos. Sci.*, 64(5):1530–1549, 2007.

Klemp, J., Dudhia, J., and Hassiotis, A. An upper gravity-wave absorbing layer for nwp applications. *Mon. Wea. Rev.*, 136(10):3987–4004, 2008.

Klemp, J. B. and Wilhelmson, R. B. The simulation of three-dimensional convective storm dynamics. *J. Atmos. Sci.*, 35(6):1070–1096, 1978.

Knievel, J. C., Bryan, G. H., and Hacker, J. P. Explicit numerical diffusion in the wrf model. *Mon. Wea. Rev.*, 135(11):3808–3824, 2007.

Langhans, W., Fuhrer, O., and Schmidli, J. Description and application of a budget-diagnosis tool in COSMO. *COSMO Newsletter*, 12:43–51, 2012a.

Langhans, W., Fuhrer, O., and Schmidli, J. Description and application of a budget-diagnosis tool in COSMO. *COSMO Newsletter*, 12:43–51, 2012b.

Langhans, W., Schmidli, J., Fuhrer, O., Bieri, S., and Schär, C. Long-term simulations of thermally driven flows and orographic convection at convection-parameterizing and cloud-resolving resolutions. *J. Appl. Meteor. Climatol.*, 52(6):1490–1510, 2013.

Langhans, W., Schmidli, J., and Schär, C. Bulk convergence of cloud-resolving simulations of moist convection over complex terrain. *J. Atmos. Sci.*, 69(7):2207–2228, 2012c.

Langhans, W., Schmidli, J., and Szintai, B. A Smagorinsky-Lilly turbulence closure for COSMO-LES: Implementation and comparison to ARPS. *COSMO Newsletter*, 12:20–31, 2012d.

Lapillonne, X., Fuhrer, O., Spörri, P., Osuna, C., Walser, A., Arteaga, A., Gysi, T., Rüdisühli, S., Osterried, K., and Schulthess, T. Operational numerical weather prediction on a gpu-accelerated cluster supercomputer. In *EGU General Assembly Conference Abstracts*, volume 18, page 13554, 2016.

Lax, P. D. and Richtmyer, R. D. Survey of the stability of linear finite difference equations. *Communications on pure and applied mathematics*, 9 (2):267–293, 1956.

Lean, H. W., Clark, P. A., Dixon, M., Roberts, N. M., Fitch, A., Forbes, R., and Halliwell, C. Characteristics of high-resolution versions of the Met Office Unified Model for forecasting convection over the United Kingdom. *Mon. Wea. Rev.*, 136(9):3408–3424, 2008.

Lebo, Z. and Morrison, H. Effects of horizontal and vertical grid spacing on mixing in simulated squall lines and implications for convective strength and structure. *Mon. Wea. Rev.*, 143(11):4355–4375, 2015.

Leroyer, S., Bélair, S., Husain, S. Z., and Mailhot, J. Subkilometer numerical weather prediction in an urban coastal area: A case study over the vancouver metropolitan area. *J. Appl. Meteor. Climatol.*, 53(6):1433–1453, 2014.

Leuenberger, D., Koller, M., Fuhrer, O., and Schär, C. A generalization of the SLEVE vertical coordinate. *Mon. Wea. Rev.*, 138(9):3683–3689, 2010.

Leutwyler, D., Fuhrer, O., Lapillonne, X., Lüthi, D., and Schär, C. Towards european-scale convection-resolving climate simulations with gpus: a study with cosmo 4.19. *Geosc. Mod. Dev.*, 9(9):3393, 2016.

Leutwyler, D., Lüthi, D., Ban, N., Fuhrer, O., and Schär, C. Evaluation of the convection-resolving climate modeling approach on continental scales. *J. Geophys. Res. Atmos.*, 122(10):5237–5258, 2017.

Lilly, D. K. On the numerical simulation of buoyant convection. *Tellus*, 14 (2):148–172, 1962.

Liu, C., Ikeda, K., Rasmussen, R., Barlage, M., Newman, A. J., Prein, A. F., Chen, F., Chen, L., Clark, M., Dai, A., et al. Continental-scale convection-permitting modeling of the current and future climate of north america. *Clim. Dyn.*, 49(1-2):71–95, 2016.

Lorenz, E. Atmospheric predictability experiments with a large numerical model. *Tellus*, 34(6):505–513, 1982.

Lorenz, E. N. Deterministic nonperiodic flow. *J. Atmos. Sci.*, 20(2):130–141, 1963.

Lorenz, E. N. Atmospheric predictability as revealed by naturally occurring analogues. *J. Atmos. Sci.*, 26(4):636–646, 1969.

Louis, J.-F. A parametric model of vertical eddy fluxes in the atmosphere. *Boundary-Layer Meteor.*, 17(2):187–202, 1979.

Ludlam, F. H. *Clouds and storms: The behavior and effect of water in the atmosphere.* Pennsylvania State University Press, 1980.

Lugauer, M. and Winkler, P. Thermal circulation in South Bavaria–climatology and synoptic aspects. *Meteor. Zeit.*, 14(1):15–30, 2005.

Meissner, C., Kalthoff, N., Kunz, M., and Adrian, G. Initiation of shallow convection in the black forest mountains. *Atmos. Res.*, 86(1):42–60, 2007.

Mellor, G. L. and Yamada, T. A hierarchy of turbulence closure models for planetary boundary layers. *J. Atmos. Sci.*, 31(7):1791–1806, 1974.

Mellor, G. L. and Yamada, T. Development of a turbulence closure model for geophysical fluid problems. *Rev. of Geophys.*, 20(4):851–875, 1982.

Métais, O. and Lesieur, M. Statistical predictability of decaying turbulence. *J. Atmos. Sci.*, 43(9):857–870, 1986.

Obermann-Hellhund, A. and Ahrens, B. Mistral and tramontane simulations with changing resolution of orography. *Atmos. Sci. Lett.*, page e848, 2018.

Orville, H. D. Ambient wind effects on the initiation and development of cumulus clouds over mountains. *J. Atmos. Sci.*, 25(3):385–403, 1968.

Panosetti, D., Böing, S., Schlemmer, L., and Schmidli, J. Idealized large-eddy and convection-resolving simulations of moist convection over mountainous terrain. *J. Atmos. Sci.*, 73(10):4021–4041, 2016.

Panosetti, D., Schlemmer, L., and Schaer, C. Convergence behavior of idealized convection-resolving simulations of summertime deep convection over land. *Clim. Dyn.*, 2018.

Panosetti, D., Schlemmer, L., and Schaer, C. Bulk and structural convergence at convection-resolving scales in real-case simulations of summertime moist convection over land. *Quart. J. Roy. Meteor. Soc.*, 2019.

Panziera, L., Gabella, M., Germann, U., and Martius, O. A 12-year radar-based climatology of daily and sub-daily extreme precipitation over the swiss alps. *Int. J. Clim.*, 2018.

Pedersen, C. A. and Winther, J.-G. Intercomparison and validation of snow albedo parameterization schemes in climate models. *Clim. Dyn.*, 25(4): 351–362, 2005.

Petch, J. Sensitivity studies of developing convection in a cloud-resolving model. *Quart. J. Roy. Meteor. Soc.*, 132(615):345–358, 2006.

Petch, J., Brown, A., and Gray, M. The impact of horizontal resolution on the simulations of convective development over land. *Quart. J. Roy. Meteor. Soc.*, 128(584):2031–2044, 2002.

Pielke Sr, R. A. Influence of the spatial distribution of vegetation and soils on the prediction of cumulus convective rainfall. *Rev. Geophys.*, 39(2): 151–177, 2001.

Pope, S. B. Turbulent flows, cambridge univ. *Press, Cambrigde*, 2000.

Prein, A. F., Langhans, W., Fosser, G., Ferrone, A., Ban, N., Goergen, K., Keller, M., Tölle, M., Gutjahr, O., Feser, F., et al. A review on regional convection-permitting climate modeling: Demonstrations, prospects, and challenges. *Rev. Geophys.*, 53(2):323–361, 2015.

Prein, A. F., Rasmussen, R. M., Ikeda, K., Liu, C., Clark, M. P., and Holland, G. J. The future intensification of hourly precipitation extremes. *Nature Climate Change*, 7(1):48–52, 2017.

Pritchard, M. S., Moncrieff, M. W., and Somerville, R. C. Orogenic propagating precipitation systems over the united states in a global climate model with embedded explicit convection. *J.Atmos. Sci.*, 68(8):1821–1840, 2011.

Purdy, J., Austin, G., Seed, A., and Cluckie, I. Radar evidence of orographic enhancement due to the seeder feeder mechanism. *Meteor. Appl.*, 12(3): 199–206, 2005.

Randall, D., Khairoutdinov, M., Arakawa, A., and Grabowski, W. Breaking the cloud parameterization deadlock. *Bull. Amer. Meteor. Soc.*, 84(11): 1547–1564, 2003.

Raschendorfer, M. The new turbulence parameterization of LM. *COSMO Newsletter*, 1:89–97, 2001.

Raymond, D. and Wilkening, M. Mountain-induced convection under fair weather conditions. *J. Atmos. Sci.*, 37(12):2693–2706, 1980.

Raymond, W. H. High-order low-pass implicit tangent filters for use in finite area calculations. *Mon. Wea. Rev.*, 116(11):2132–2141, 1988.

Reinhardt, T. and Seifert, A. A three-category ice scheme for LMK. *COSMO Newsletter*, 6:115–120, 2006.

Reiter, E. R. and Tang, M. Plateau effects on diurnal circulation patterns. *Mon. Wea. Rev.*, 112(4):638–651, 1984.

Renno, N. O., Emanuel, K. A., and Stone, P. H. Radiative-convective model with an explicit hydrologic cycle: 1. formulation and sensitivity to model parameters. *J. Geophys. Res.: Atmospheres*, 99(D7):14429–14441, 1994.

Ricard, D., Lac, C., Riette, S., Legrand, R., and Mary, A. Kinetic energy spectra characteristics of two convection-permitting limited-area models arome and meso-nh. *Quart. J. Roy. Meteor. Soc.*, 139(674):1327–1341, 2013.

Richard, E., Buzzi, A., and Zängl, G. Quantitative precipitation forecasting in the alps: The advances achieved by the mesoscale alpine programme. *Quart. J. Roy. Meteor. Soc.*, 133(625):831–846, 2007.

Richard, E., Chaboureau, J.-P., Flamant, C., Champollion, C., Hagen, M., Schmidt, K., Kiemle, C., Corsmeier, U., Barthlott, C., and Di Girolamo, P. Forecasting summer convection over the black forest: a case study from the convective and orographically-induced precipitation study (cops) experiment. *Quart. J. Roy. Meteor. Soc.*, 137(S1):101–117, 2011.

Rihani, J. F., Chow, F. K., and Maxwell, R. M. Isolating effects of terrain and soil moisture heterogeneity on the atmospheric boundary layer: Idealized simulations to diagnose land-atmosphere feedbacks. *J. Adv. Model. Earth Syst.*, 7(2):915–937, 2015.

Ritter, B. and Geleyn, J.-F. A comprehensive radiation scheme for numerical weather prediction models with potential applications in climate simulations. *Mon. Wea. Rev.*, 120(2):303–325, 1992.

Rockel, B., Will, A., and Hense, A. The Regional Climate Model COSMO-CLM (CCLM). *Meteor. Zeit.*, 17(4):347–348, 2008.

Rotach, M. W. and Zardi, D. On the boundary-layer structure over highly complex terrain: key findings from MAP. *Quart. J. Roy. Meteor. Soc.*, 133 (625):937–948, 2007.

Rotunno, R. and Snyder, C. A generalization of lorenz's model for the predictability of flows with many scales of motion. *J. Atmos. Sci.*, 65(3): 1063–1076, 2008.

Saito, K., Ishida, J.-I., Aranami, K., Hara, T., Segawa, T., Narita, M., and Honda, Y. Nonhydrostatic atmospheric models and operational development at jma. *J. Meteor. Soc. Japan*, 85:271–304, 2007.

Sanderson, B. M., Piani, C., Ingram, W., Stone, D., and Allen, M. Towards constraining climate sensitivity by linear analysis of feedback patterns in thousands of perturbed-physics gcm simulations. *Clim. Dyn.*, 30(2-3):175–190, 2008.

Schär, C. Mesoscale mountains and the larger-scale atmospheric dynamics: A review. In *Int. Geophys.*, volume 83, pages 29–42. Elsevier, 2002.

Schär, C., Leuenberger, D., Fuhrer, O., Lüthi, D., and Girard, C. A new terrain-following vertical coordinate formulation for atmospheric prediction models. *Mon. Wea. Rev.*, 130(10):2459–2480, 2002.

Schemann, V., Stevens, B., Grützun, V., and Quaas, J. Scale dependency of total water variance and its implication for cloud parameterizations. *J. Atmos. Sci.*, 70(11):3615–3630, 2013.

Schlemmer, L. and Hohenegger, C. The formation of wider and deeper clouds as a result of cold-pool dynamics. *J. Atmos. Sci.*, 71(8):2842–2858, 2014.

Schlemmer, L., Hohenegger, C., Schmidli, J., Bretherton, C. S., and Schär, C. An idealized cloud-resolving framework for the study of midlatitude diurnal convection over land. *J. Atmos. Sci.*, 68(5):1041–1057, 2011.

Schmidli, J. Daytime heat transfer processes over mountainous terrain. *J. Atmos. Sci.*, 70(12):4041–4066, 2013.

Schmidli, J., Billings, B., Chow, F. K., de Wekker, S. F., Doyle, J., Grubišic, V., Holt, T., Jiang, Q., Lundquist, K. A., Sheridan, P., et al. Intercomparison of mesoscale model simulations of the daytime valley wind system. *Mon. Wea. Rev.*, 139(5):1389–1409, 2011.

Schmidli, J. and Rotunno, R. Mechanisms of along-valley winds and heat exchange over mountainous terrain. *J. Atmos. Sci.*, 67(9):3033–3047, 2010.

Schmidli, J. and Rotunno, R. Influence of the valley surroundings on valley wind dynamics. *J. Atmos. Sci.*, 69(2):561–577, 2012.

Schneider, T. The general circulation of the atmosphere. *Annu. Rev. Earth Planet. Sci.*, 34:655–688, 2006.

Schneider, T., O'Gorman, P. A., and Levine, X. J. Water vapor and the dynamics of climate changes. *Rev. Geophys.*, 48(3), 2010.

Schwartz, C. S., Kain, J. S., Weiss, S. J., Xue, M., Bright, D. R., Kong, F., Thomas, K. W., Levit, J. J., and Coniglio, M. C. Next-day convection-allowing WRF model guidance: A second look at 2-km versus 4-km grid spacing. *Mon. Wea. Rev.*, 137(10):3351–3372, 2009.

Selz, T. and Craig, G. C. Upscale error growth in a high-resolution simulation of a summertime weather event over europe. *Mon. Wea. Rev.*, 143(3):813–827, 2015.

Serafin, S. and Zardi, D. Daytime heat transfer processes related to slope flows and turbulent convection in an idealized mountain valley. *J. Atmos. Sci.*, 67(11):3739–3756, 2010.

Sherwood, S. C., Bony, S., and Dufresne, J.-L. Spread in model climate sensitivity traced to atmospheric convective mixing. *Nature*, 505(7481):37, 2014.

Shin, H. H. and Hong, S.-Y. Representation of the subgrid-scale turbulent transport in convective boundary layers at gray-zone resolutions. *Mon. Wea. Rev.*, 143(1):250–271, 2015.

Skamarock, W. C. Evaluating mesoscale nwp models using kinetic energy spectra. *Mon. Wea. Rev.*, 132(12):3019–3032, 2004.

Skamarock, W. C., Park, S.-H., Klemp, J. B., and Snyder, C. Atmospheric kinetic energy spectra from global high-resolution nonhydrostatic simulations. *J. Atmos. Sci.*, 71(11):4369–4381, 2014.

Smagorinsky, J. General circulation experiments with the primitive equations: I. the basic experiment. *Mon. Wea. Rev.*, 91(3):99–164, 1963.

Smagorinsky, J. Global atmospheric modeling and the numerical simulation of climate. *Weather and climate modification*, pages 633–686, 1974.

Song, X. and Zhang, G. J. Convection parameterization, tropical pacific double itcz, and upper-ocean biases in the ncar ccsm3. part i: Climatology and atmospheric feedback. *J. Clim.*, 22(16):4299–4315, 2009.

Stevens, B. Atmospheric moist convection. *Annu. Rev. Earth Planet. Sci.*, 33:605–643, 2005.

Stevens, B. and Bony, S. Waterin the atmosphere. *Phys. Today*, 66(6):29, 2013a.

Stevens, B. and Bony, S. What are climate models missing? *Science*, 340 (6136):1053–1054, 2013b.

Stoll, R. and Porté-Agel, F. Surface heterogeneity effects on regional-scale fluxes in stable boundary layers: surface temperature transitions. *J. Atmos. Sci.*, 66(2):412–431, 2009.

Tang, Y., Lean, H. W., and Bornemann, J. The benefits of the met office variable resolution nwp model for forecasting convection. *Meteor. Appl.*, 20(4):417–426, 2013.

Taylor, C. M., Birch, C. E., Parker, D. J., Dixon, N., Guichard, F., Nikulin, G., and Lister, G. M. Modeling soil moisture-precipitation feedback in the sahel: Importance of spatial scale versus convective parameterization. *Geophys. Res. Lett.*, 40(23):6213–6218, 2013.

Taylor, C. M., Lambin, E. F., Stephenne, N., Harding, R. J., and Essery, R. L. The influence of land use change on climate in the sahel. *J. Clim.*, 15(24):3615–3629, 2002.

Tiedtke, M. A comprehensive mass flux scheme for cumulus parameterization in large-scale models. *Mon. Wea. Rev.*, 117(8):1779–1800, 1989.

Tribbia, J. and Baumhefner, D. Scale interactions and atmospheric predictability: An updated perspective. *Mon. Wea. Rev.*, 132(3):703–713, 2004.

van Ypersele de Strihou, J.-P. and Marbaix, P. Sensitivity of convection-permitting regional climate simulations to the level of microphysics parameterization complexity. In *CORDEX International Conference on Regional Climate*, 2013.

Verrelle, A., Ricard, D., and Lac, C. Sensitivity of high-resolution idealized simulations of thunderstorms to horizontal resolution and turbulence parametrization. *Quart. J. Roy. Meteor. Soc.*, 141(687):433–448, 2015.

Vukicevic, T. and Errico, R. M. The influence of artificial and physical factors upon predictability estimates using a complex limited-area model. *Mon. Wea. Rev.*, 118(7):1460–1482, 1990.

Wagner, A. Neue Theorie des Berg- und Talwindes (a new theory of mountain and valley winds). *Meteor. Zeit.*, 49:329–341, 1932.

Wagner, J. S., Gohm, A., and Rotach, M. W. The impact of horizontal model grid resolution on the boundary layer structure over an idealized valley. *Mon. Wea. Rev.*, 142(9):3446–3465, 2014.

Wan, H., Giorgetta, M. A., Zängl, G., Restelli, M., Majewski, D., Bonaventura, L., Fröhlich, K., Reinert, D., Rıpodas, P., Kornblueh, L., et al. The icon-1.2 hydrostatic atmospheric dynamical core on triangular grids, part i: formulation and performance of the baseline version. *Geosc. Mod. Devel.*, 6:735–763, 2013.

Weisman, M. L., Davis, C., Wang, W., Manning, K. W., and Klemp, J. B. Experiences with 0–36-h explicit convective forecasts with the wrf-arw model. *Wea. Forecasting*, 23(3):407–437, 2008.

Weisman, M. L. and Klemp, J. B. The dependence of numerically simulated convective storms on vertical wind shear and buoyancy. *Mon. Wea. Rev.*, 110(6):504–520, 1982.

Weisman, M. L., Skamarock, W. C., and Klemp, J. B. The resolution dependence of explicitly modeled convective systems. *Mon. Wea. Rev.*, 125(4): 527–548, 1997.

Weissmann, M., Braun, F., Gantner, L., Mayr, G., Rahm, S., and Reitebuch, O. The alpine mountain-plain circulation: Airborne doppler lidar measurements and numerical simulations. *Mon. Wea. Rev.*, 133(11):3095–3109, 2005.

Weusthoff, T., Ament, F., Arpagaus, M., and Rotach, M. W. Assessing the benefits of convection-permitting models by neighborhood verification: Examples from map d-phase. *Mon. Wea. Rev.*, 138(9):3418–3433, 2010.

White, B., Gryspeerdt, E., Stier, P., Morrison, H., Thompson, G., and Kipling, Z. Uncertainty from the choice of microphysics scheme in convection-permitting models significantly exceeds aerosol effects. *Atmos. Chem. and Phys.*, 17(19):12145, 2017.

Whiteman, C. D. Observations of thermally developed wind systems in mountainous terrain. *Atmos. Proc. over Complex Terrain, Meteor. Monogr.*, 23 (45):5–42, 1990.

Wicker, L. J. and Skamarock, W. C. Time-splitting methods for elastic models using forward time schemes. *Mon. Wea. Rev.*, 130(8):2088–2097, 2002.

Wulfmeyer, V., Behrendt, A., Bauer, H.-S., Kottmeier, C., Corsmeier, U., Blyth, A., Craig, G., Schumann, U., Hagen, M., Crewell, S., et al. The convective and orographically induced precipitation study: a research and development project of the world weather research program for improving quantitative precipitation forecasting in low-mountain regions. *Bull. Amer. Meteor. Soc.*, 89(10):1477–1486, 2008.

Wulfmeyer, V., Behrendt, A., Kottmeier, C., Corsmeier, U., Barthlott, C., Craig, G. C., Hagen, M., Althausen, D., Aoshima, F., Arpagaus, M., et al. The Convective and Orographically-induced Precipitation Study (COPS): the scientific strategy, the field phase, and research highlights. *Quart. J. Roy. Meteor. Soc.*, 137(S1):3–30, 2011.

Wyngaard, J. C. Toward numerical modeling in the "terra incognita". *J. Atmos. Sci.*, 61(14):1816–1826, 2004.

Wyngaard, J. C. *Turbulence in the Atmosphere.* Cambridge University Press, 2010.

Xie, S.-P., Xu, H., Saji, N., Wang, Y., and Liu, W. T. Role of narrow mountains in large-scale organization of asian monsoon convection. *J. Clim.*, 19 (14):3420–3429, 2006.

Xu, K.-M., Cederwall, R. T., Donner, L. J., Grabowski, W. W., Guichard, F., Johnson, D. E., Khairoutdinov, M., Krueger, S. K., Petch, J. C., Randall, D. A., et al. An intercomparison of cloud-resolving models with the atmospheric radiation measurement summer 1997 intensive observation period data. *Quart. J. Roy. Meteor. Soc.*, 128(580):593–624, 2002.

Zhang, F., Snyder, C., and Rotunno, R. Mesoscale predictability of the "surprise" snowstorm of 24–25 january 2000. *Mon. Wea. Rev.*, 130(6):1617–1632, 2002.

Zhang, F., Snyder, C., and Rotunno, R. Effects of moist convection on mesoscale predictability. *J. Atmos. Sci.*, 60(9):1173–1185, 2003.

Zhang, G. J. and Mu, M. Simulation of the madden–julian oscillation in the ncar ccm3 using a revised zhang–mcfarlane convection parameterization scheme. *J. Clim.*, 18(19):4046–4064, 2005.

Zhang, G. J. and Song, X. Convection parameterization, tropical pacific double itcz, and upper-ocean biases in the ncar ccsm3. part ii: Coupled feedback and the role of ocean heat transport. *J. Clim.*, 23(3):800–812, 2010.

Zhou, B., Simon, J. S., and Chow, F. K. The convective boundary layer in the terra incognita. *J. Atmos. Sci.*, 71(7):2545–2563, 2014.

Zhou, B., Sun, S., Yao, K., and Zhu, K. Re-examining the gradient and counter-gradient representation of the local and non-local heat fluxes in the convective boundary layer. *J. Atmos. Sci.*, 2018.

Curriculum Vitae

Davide Panosetti
Institute for Atmospheric and Climate Science
ETH Zurich
Universitätstrasse 16
8092 Zurich, Switzerland   ✉davide.panosetti@gmail.com

Personal

Citizen of Italy, born on 23 May 1990 in Segrate, Italy

Academic Background

since 2019	**ETH Zurich**, Switzerland **Postdoctoral researcher** Institute for Atmospheric and Climate Science, Climate and Water Cycle Group
2015 – 2018	**ETH Zurich**, Switzerland **PhD student in Atmospheric and Climate Science** Institute for Atmospheric and Climate Science, Climate and Water Cycle Group
Thesis:	Resolution sensitivity and convergence behavior of convection-resolving simulations of summertime moist convection over land
Supervisors:	Prof. Dr. Christoph Schär Dr. Linda Schlemmer
Examiner:	Dr. Evelyne Richard

2013 – 2015	**ETH Zurich**, Switzerland
	MSc in Atmospheric and Climate Science
Thesis:	Idealized large-eddy and convection-resolving simulations of summertime deep convection over a double mountain ridge
Supervisors:	Prof. Dr. Christoph Schär
	Dr. Steven Böing
	Dr. Linda Schlemmer
	Dr. Jürg Schmidli

2010 – 2013	**University of Bologna**, Italy
	BSc in Atmospheric Physics and Meteorology
Thesis:	First findings on the thermal regime of the largest living wall in Europe (Rozzano, Italy)
Supervisors:	Dr. Teodoro Georgiadis
	Dr. Marianna Nardino
	Prof. Dr. Rolando Rizzi

| 2004 – 2009 | **Lindbergh Flying School**, Italy |

Teaching

Teaching Assistant in:

Fall 2017	Numerical Methods in Environmental Physics (BSc)
Spring 2016 & 2017	Numerical Modeling of Weather and Climate (MSc)
Fall 2015 & 2016	Boundary Layer Meteorology (MSc)

Supervision

| MSc thesis: | Christopher Heim (Fall 2017 & Spring 2018) |
| | "The influence of the resolution of topography and surface fields on the simulation of orographic moist convection" |

Publications

Panosetti, D., L. Schlemmer, and C. Schär (2019): On the subgrid-scale turbulence parameterization at convection-resolving scales and its impact on the mean flow properties and individual convective cells. *Mon. Wea. Rev.*, in preparation.

Schär, C., A. Arteaga, N. Ban, C. Charpilloz, S. Di Girolamo, O. Fuhrer, L. Hentgen, T. Höfler, X. Lapillonne, D. Leutwyler, K. Osterried, **D.**

Panosetti, S. Rüdisühli, T. Schulthess, M. Sprenger, S. Ubbiali and H. Wernli (2019): Kilometer-scale climate models: prospects and challenges." *Bull. Amer. Meteor. Soc.*, submitted.

Vergara-Temprado, J., N. Ban, **D. Panosetti**, L. Schlemmer, and C. Schär (2019): Climate models permit convection at much coarser resolution than previously considered. *J. Clim.*, submitted.

Heim, C., **D. Panosetti**, L. Schlemmer, and C. Schär (2019): Influence of topography resolution on the simulation of orographic moist convection. *Mon. Wea. Rev.*, in preparation.

Panosetti, D., L. Schlemmer, and C. Schär (2019): Bulk and structural convergence at convection-resolving scales in real-case simulations of summertime moist convection over land. *Quart. J. Roy. Meteor. Soc.*, published online on 10 February 2019, doi:10.1002/qj.3502.

Panosetti, D., L. Schlemmer, and C. Schär (2018): Convergence behavior of idealized convection-resolving simulations of summertime deep moist convection over land. *Clim. Dyn.*, published online on 4 May 2018, doi:10.1007/s00382-018-4229-9.

Panosetti, D., S. Böing, L. Schlemmer, and J. Schmidli (2016). Idealized large-eddy and convection-resolving simulations of moist convection over mountainous terrain. *J. Atmos. Sci.*, 73, 4021–4041, doi:10.1175/JAS-D-15-0341.1.

Oral presentations

Panosetti, D., L. Schlemmer, and C. Schär: Convergence behavior of convection-resolving simulations of summertime moist convection over land.

AGU Fall Meeting 2018, 9-14 December 2018, Washington D.C., USA
California Institute of Technology, 6 December 2018, Pasadena, USA (invited)
CLM Assembly 2018, 18-21 September 2018, Karlsruhe Institute of Technology, Karlsruhe, Germany
COSMO/CLM/ICON/ART User Seminar, 06-08 March 2017, Offenbach am Main, Germany
EGU General Assembly 2017, 23-28 April 2017, Vienna, Austria
Istanbul Technical University, 02 October 2017, Istanbul, Turkey (invited)

Panosetti, D., S. Böing, L. Schlemmer, and J. Schmidli: Idealized large-eddy

and convection-resolving simulations of moist convection over mountainous terrain.

Goethe-University Frankfurt, 01 September 2016, Frankfurt am Main, Germany (invited)

Panosetti, D., T. Georgiadis, and M. Nardino: First findings on the thermal regime of the largest living wall in Europe (Rozzano, Italy).

International Conference on Urban Climate and History of Meteorology, 25-26 February 2013, Florence, Italy

Poster presentations

Panosetti, D., L. Schlemmer, and C. Schär: On the treatment of subgrid-scale turbulence at convection-resolving scales and sensitivities in real-case simulations.

EGU General Assembly 2010, 7-12 April 2019, Vienna, Austria

Panosetti, D., L. Schlemmer, and C. Schär: Convergence behavior of convection-resolving simulations of summertime moist convection over land.

$HD(CP)^2$ conference "Understanding clouds and precipitation" 2019, 25 February-1 March 2019, Berlin, Germany
EGU General Assembly 2018, 8-13 April 2018, Vienna, Austria
ECMWF Workshop: "Shedding the light on the grey zone", 13-16 November 2017, Reading, UK
16th International Swiss Climate Summer School, 3-8 September 2017, Ascona, Switzerland

Panosetti, D., S. Böing, L. Schlemmer, and J. Schmidli: Idealized large-eddy and convection-resolving simulations of moist convection over mountainous terrain.

$HD(CP)^2$ conference "Understanding clouds and precipitation", 15-19 February 2016, Berlin, Germany

Honors and awards

Outstanding Student Poster and PICO (OSPP) Award at the EGU General Assembly 2018, 8-13 April 2018, Vienna, Austria